Dielectrophoretic Analysis of Polystyrene Spheres in Fluidic Suspension

by

Timothy Ian Cabel

A Thesis submitted to the Faculty of Graduate Studies of

The University of Manitoba

in partial fulfilment of the requirements of the degree of

MASTER OF SCIENCE

Department of Electrical and Computer Engineering

University of Manitoba

Winnipeg

UNIVERSITY OF MANITOBA | Graduate Studies

Master's Thesis/Practicum Final Report

The undersigned certify that they have read the Master's Thesis/Practicum entitled:

Dielectrophoretic Analysis of Polystyrene Spheres in Fluidic Suspension

submitted by

Timothy Cabel

in partial fulfillment of the requirements for the degree of

M.Sc.

The Thesis/Practicum Examining Committee certifies that the thesis/practicum (and oral examination if required) is:	Approved ☐	Thesis ☑
	Not Approved ☐	Practicum ☐

	Name	Signature
	Dr. G. Bridges (*Advisor*)	
	(*Advisory Committee member*)	
	Dr. D. Thomson, ECE (*Advisory Committee member*)	
	Dr. M. Birouk, MME (*Advisory Committee member*)	

Date _____ (*MM/DD/YYYY*)

Abstract

Polystyrene spheres, suspended in deionized water, flowing in a microfluidic channel are actuated using a non-uniform electric field, with the final goal of determining the dielectrophoretic (DEP) force spectra of the particles. Particle height changes are detected by measuring the capacitance of set of electrodes at high frequency (1.58 GHz). Two sets of DEP experiments are analyzed for applied DEP signals ranging in frequency from 50 kHz to 10 MHz. For one experiment, a simulated mapping is found to determine the Clausius-Mossotti factor, a frequency dependent term in the DEP force equation, for each particle in the data set. Remaining experiments are analyzed by plotting the normalized height change, a measure of the relative change in height of each particle as an indication of the DEP force.

Acknowledgements

I would like to thank my advisor Greg Bridges for giving me the opportunity to continue my education into the MSc program and for all of his help and guidance. I would also like to thank my research group, Douglas Thomson, Marija Nikolic-Jaric, Graham Ferrier, Elham Salimi, Ashlesha Bhide, Bahareh Saboktakin, and Kaveh Mohammad for all their help.

I also thank my parents for all their support through my academic career, and my girlfriend Kelsey Romano for all her support and help.

Table of Contents

List of Figures

List of Tables

Nomenclature

Abbreviations

DEP	Dielectrophoresis or dielectrophoretic
nDEP	Negative dielectrophoresis or negative dielectrophoretic
pDEP	Positive dielectrophoresis or positive dielectrophoretic
$\overline{E}$	Vector E
$\underline{E}$	Complex value E

Constants

$\epsilon_0 = 8.854 \times 10^{-12}\,\mathrm{F\,m^{-1}}$ electromagnetic permittivity of free space

Chapter 1

Background and Motivation

AC electrokinetic manipulation of micrometer and nanometer scale particles has rapidly become a major area of research. The ability to manipulate particles via contactless forces has allowed non-invasive and efficient characterization, identification, and separation of different particle types in fluidic suspension [3]. Using photolithographic and etching techniques common for the manufacturing of semiconductor devices, the fabrication of microfluidic devices become much more acessible and has allowed analysis on the single particle level to follow. By characterizing particles one at a time and with use of automation techniques, detailed analysis of a large populations of particles can be performed in a short amount of time.

A major area of interest for applications in electrokinetic particle manipulation is biological particles, namely biological cells, viruses, DNA, and proteins [3]. For biological cells in particular it has been shown that the dielectric properties of a cell can be directly linked to cell physiology [4]. This makes it possible to use electrokinetic techniques such as dielectrophoresis (DEP), which will be main focus of this thesis, to determine specific properties of individual cells within a population. As opposed to bulk dielectric measurements, single cell dielectrophoretic analysis can allow for

characterization of subpopulations that make up a very small percentage of a bulk sample, allowing for the detection of even the smallest of subpopulations. In order to develop a more accurate model for the characterization of biological cells using DEP, this thesis will explore the DEP characteristics of various sizes of polystyrene microspheres (PSS) in a frequency range of 50 kHz to 10 MHz. Techniques will be explored to normalized collected capacitance signals and convert them into a Clausius-Mossotti factor, a term in the dielectrophetic force equation that determines the polarity and magnitude of the force.

The term dielectrophoresis was first used by Herbert Pohl in a paper published in 1951. The paper defines the DEP force as "the phenomenon seen in the relative motion of suspensoid and medium resulting from polarization forces produced by an inhomogeneous electric field"[5]. He named and theoretically calculated the dielectrophoretic force after attempting to use electrophoresis to remove carbon-black filler from polyvinyl chloride. In the paper he contrasted the difference between dielectrophoresis and the already commonly known electrophoresis after he discovered that the resulting force in his experiment wasn't reversible by a field of opposite polarity, and that it affected neutrally charged particles, which electrophoresis would not. Following this original use for removing colloidal particles for polymer analysis, he moved on from his initial application to using dielectrophoresis to analyze the electrical properties of biological cells [6, 7, 8, 9].

The following contributions were made:

- Developed theory and experimental study of dielectrophoretic force on polystyrene spheres in a fluid suspension

- Developed analysis method for finding the instantaneous particle speed based on the width of the particle signal

- Developed analysis method for finding the system sensitivity and particle heights using simulated data and curve fitting
- Developed analysis method to determine the Clausius-Mossotti factor of each particle in a population based on a calculated particle heights and a mapping created from multiple simulated particle trajectories
- Design of a microfluidic chip with a split electrode design along with microfluidics group allowing for separation of the sensing and actuation regions
- Wrote signal processing and capture software to collect and analyze capacitance signals
- Developed interferometric system for measuring electrode capacitance and microfluidics delivery system along with microfluidics group: G. Ferrier, S.F. Romanuik, M. Nikolic-Jaric, S. Rzeszowski, E. Salimi, and D. Card

The following sections will outline the derivation of the dielectrophoretic force on a micron scale particle, suspended in a solution, in the presence of a non-uniform electric field. The derivation will follow the steps outlined in Thomas B. Jones's book, *Electromechanics of Particles* [10].

1.1 Force Induced on a Dipole in an Electric Field

In order to characterize the dielectrophoretic force and properly interpret experimental results, an analytical approach is first necessary to determine an expression to approximate the dielectrophoretic response. The following sections will be used to derive an equation to approximate the force exerted on a lossy, polarizable particle in a lossy medium, in the presence of a non-uniform field.

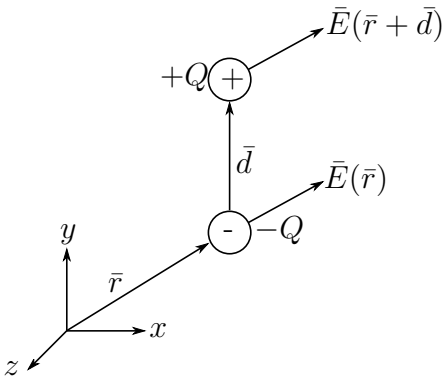

Figure 1.1: Dipole placed in an external electric field.

When a dielectric particle is placed in an electric field, electric charges will separate according to the direction of the field and the particle will become polarized. The simplest approximation for any polarized particle is an electric dipole. A general illustration of the dipole is shown in Figure 1.1; formed when equal and opposite charges, $\pm Q$, are separated by distance, $|\bar{d}|$. When the dipole is introduced into an external electric field, $\overline{E}$, both charges will experience a force proportional to their sign and position in the field. If the field is uniform the force magnitudes will cancel, since $\overline{E}(\bar{r}+\bar{d}) = \overline{E}(\bar{r})$, and the particle will experience a torque with no net force. However, if the field is non-uniform, then the forces on each of charges will not be equal and a net force will be produced. The net force being given as:

$$\overline{F} = Q\overline{E}(\bar{r}+\bar{d}) - Q\overline{E}(\bar{r}) \tag{1.1}$$

where $Q\overline{E}(\bar{r}+\bar{d})$ is the Coulomb force acting on the positive charge located at $\bar{r}+\bar{d}$ and $-Q\overline{E}(\bar{r})$ is the Coulomb force acting on the negative charge at $\bar{r}$. When $|\bar{d}|$ is small compared to the electric field non-uniformity, generally when $|\bar{r}| >> |\bar{d}|$, if the origin is the point of field emission, a Taylor series expansion can be done for $\overline{E}(\bar{r}+\bar{d})$

about $\bar{r}$:

$$\overline{E}(\bar{r}+\bar{d}) = \overline{E}(\bar{r}) + \bar{d}\cdot\nabla\overline{E}(\bar{r}) + \frac{1}{2}(\bar{d}\cdot\nabla)(\bar{d}\cdot\nabla)\overline{E}(\bar{r}) + \cdots \tag{1.2}$$

If the field non-uniformities are small, relative to the length of the dipole, then the first two terms will dominate and (1.1) becomes:

$$\begin{aligned}\overline{F} &\approx Q(\overline{E}(\bar{r}) + \bar{d}\cdot\nabla\overline{E}(\bar{r})) - Q\overline{E}(\bar{r}) \\ &= Q\bar{d}\cdot\nabla\overline{E}(\bar{r})\end{aligned} \tag{1.3}$$

If the length of the dipole is reduced to approach zero, $|\bar{d}| \to 0$, while still maintaining a finite length such that the dipole moment, $\bar{p} \equiv Q\bar{d}$ is non-zero, then the expression approaches the force on an infinitesimal dipole:

$$\overline{F}_{dipole} = \bar{p}\cdot\nabla\overline{E} \tag{1.4}$$

From this general equation it is shown that for a dipole in an electric field, no net force is exerted unless there is some non-uniformity in the field, that is $\nabla\overline{E} \neq 0$.

1.2 Dipole Potential and Effective Dipole Moment

The above force derivation can be extended to work on any dipole, including a polarized particle, assuming field non-uniformities are on a larger scale than the dipole. When an external non-uniform field polarizes a particle, which in turn causes the force on the particle, the above approximation is known as the dielectrophoretic approximation and the resulting force is a dielectrophoretic (DEP) force, F_{DEP}. In order to determine the full equation for the dielectrophoretic force on a spherical

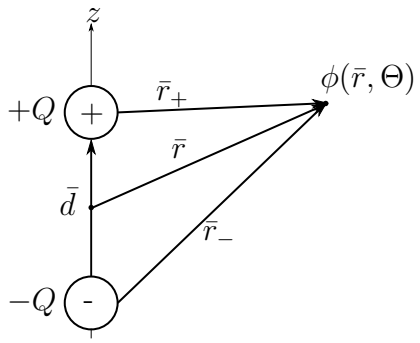

Figure 1.2: Electric field of an infinitesimal dipole.

dielectric particle an effective dipole moment, $\bar{p}_{eff}$, must be found. The effective dipole moment is the dipole moment of an infinitesimal dipole placed at the center of the dielectric particle in the same medium which, when the particle is removed, results in the same electrostatic field.

First the potential of an infinitesimal dipole with dipole moment $\bar{p}_{eff}$ is needed. Figure 1.2 shows a the dipole used in the derivation. Using superposition the potentials from the two point charges are combined:

$$\begin{aligned} \phi_{dipole}(r,\theta) &= \frac{Q}{4\pi\varepsilon_{med} r_+} - \frac{Q}{4\pi\varepsilon_{med} r_-} \\ &= \frac{Q}{4\pi\varepsilon_{med} r} \left(\frac{r}{r_+} - \frac{r}{r_-} \right) \end{aligned} \tag{1.5}$$

where by geometry $r_\pm$ can be found to be:

$$\begin{aligned} r_\pm^2 &= (d/2)^2 + r^2 \mp dr\cos(\theta) \\ \left(\frac{r}{r_\pm}\right) &= \left[1 + \left(\frac{d}{2r}\right)^2 \mp \left(\frac{d}{r}\right)\cos(\theta) \right]^{-1/2} \end{aligned} \tag{1.6}$$

then expanding the function using a Maclaurin series:

$$\left(\frac{r}{r_{\pm}}\right) = P_0 \pm P_1\left(\frac{d}{2r}\right) + P_2\left(\frac{d}{2r}\right)^2 \pm P_3\left(\frac{d}{2r}\right)^3 + \cdots \tag{1.7}$$

where $P_n(\cos(\theta))$ are Legendre polynomials and are given by Table 1.1. Combining (1.6) and (1.7) gives the full expression for the electrostatic potential of an infinitesimal dipole:

$$\phi_{dipole}(r,\theta) = \frac{QdP_1(\cos(\theta))}{4\pi\varepsilon_{med}r^2} + \frac{Qd^3P_3(\cos(\theta))}{16\pi\varepsilon_{med}r^4} + \cdots \tag{1.8}$$

$$\approx \frac{QdP_1(\cos(\theta))}{4\pi\varepsilon_{med}r^2} \tag{1.9}$$

As long as $d << r$, a first order approximation is sufficiently accurate, making the potential due to a dipole with dipole moment, $\bar{p} = Q\bar{d}$:

$$\phi_{dipole}(r,\theta) \approx \frac{|\bar{p}|\,P_1(\cos(\theta))}{4\pi\varepsilon_{med}r^2} \tag{1.10}$$

The approximation breaks down as $r \to d$ and the multipolar terms become larger. Applying this solution to a dielectric particle, the effective dipole moment is first found by solving the boundary value problem when the particle is placed in an electric field and comparing the induced dipole term from the solution.

Table 1.1: Maclaurin series coefficients for electrostatic dipole potential.

n	$P_n(\cos(\theta))$	
0	$f(0)$	1
1	$\frac{f'(0)}{1!}$	$\cos(\theta)$
2	$\frac{f''(0)}{2!}$	$[3\cos^2(\theta) - 1]/2$
3	$\frac{f'''(0)}{3!}$	$[5\cos^3(\theta) - 3\cos(\theta)]/2$

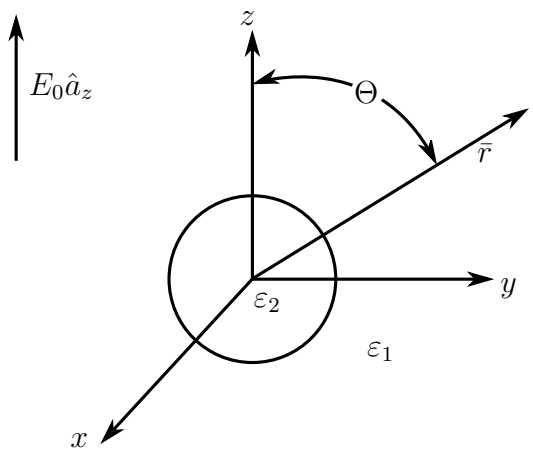

Figure 1.3: Dielectric particle placed in a uniform electric field.

1.3 Effective Dipole Moment of a Lossless Dielectric Particle in a Uniform Electric Field

Consider a uniform electric field of magnitude E_0 polarized in the $\hat{a}_z$ direction in a medium with permittivity ε_1. Shown in Figure 1.3, a lossless dielectric sphere of radius a and permittivity ε_2 is placed in the field. The resulting potential outside and inside the sphere, will be defined as $\phi_1(r,\theta)$ and $\phi_2(r,\theta)$, respectively. Upon solving Laplace's equation, $\nabla \cdot (\varepsilon \nabla \phi) = 0$, inside and outside the sphere the solution takes the form [10]:

$$\phi_1(r,\theta) = -E_0 r\cos(\theta) + \frac{A\cos(\theta)}{r^2}, \qquad r \geq a \tag{1.11a}$$

$$\phi_2(r,\theta) = -Br\cos(\theta), \qquad r \leq a \tag{1.11b}$$

where A and B are unknown coefficients that will now be determined. Starting from the boundary conditions, both the electrostatic potential and the normal component

of the electric displacement field must be continuous:

$$\phi_1(r=a,\theta) = \phi_2(r=a,\theta) \tag{1.12a}$$

$$\varepsilon_1 E_{r1}(r=a,\theta) = \varepsilon_2 E_{r2}(r=a,\theta) \tag{1.12b}$$

where $E_{r1} = -\partial\phi_1/\partial r$ and $E_{r2} = -\partial\phi_2/\partial r$ are the radial components of the electric field outside and inside of the particle, respectively. On combining (1.11) and (1.12), and solving for A and B the following result is obtained:

$$A = \frac{\varepsilon_2 - \varepsilon_1}{\varepsilon_2 + 2\varepsilon_1} a^3 E_0 \tag{1.13a}$$

$$B = \frac{3\varepsilon_1}{\varepsilon_2 + 2\varepsilon_1} E_0. \tag{1.13b}$$

Plugging A and B back into (1.11), the potential inside and outside the particle becomes:

$$\phi_1(r,\theta) = -E_0\cos(\theta)\left[r + \frac{Ka^3}{r^2}\right], \qquad r \geq a \tag{1.14a}$$

$$\phi_2(r,\theta) = -\frac{3\varepsilon_1}{\varepsilon_2 + 2\varepsilon_1} r\cos(\theta), \qquad r \leq a \tag{1.14b}$$

where $K = \frac{\varepsilon_2 - \varepsilon_1}{\varepsilon_2 + 2\varepsilon_1}$. Solving for $\overline{E} = -\nabla\phi$ inside and outside the particle gives the full solution:

$$\begin{aligned}
\overline{E}_1(r,\theta) &= -\frac{\partial\phi_1}{\partial r}\hat{a}_r - \frac{1}{r}\frac{\partial\phi_1}{\partial\theta}\hat{a}_\theta, && r \geq a \\
&= E_0\cos(\theta)\left[1 - 2Ka^3/r^3\right]\hat{a}_r - E_0\sin(\theta)\left[1 + Ka^3/r^3\right]\hat{a}_\theta, && r \geq a \\
&= E_0\hat{a}_z + \frac{E_0 K a^3}{r^3}\left[2\cos(\theta)\hat{a}_r + \sin(\theta)\hat{a}_\theta\right], && r \geq a \qquad (1.15a) \\
\overline{E}_2(r,\theta) &= -\frac{\partial\phi_2}{\partial r}\hat{a}_r - \frac{1}{r}\frac{\partial\phi_2}{\partial\theta}\hat{a}_\theta, && r \leq a
\end{aligned}$$

$$= \frac{3\varepsilon_1}{\varepsilon_2 + 2\varepsilon_1} E_0 \left[\cos(\theta)\hat{a}_r - \sin(\theta)\hat{a}_\theta\right], \qquad r \leq a$$
$$= \frac{3\varepsilon_1}{\varepsilon_2 + 2\varepsilon_1} E_0 \hat{a}_z, \qquad r \leq a. \quad (1.15b)$$

Following from (1.10), (1.11a), and (1.13a), the effective dipole moment, p_{eff}, can be found:

$$\begin{aligned} \bar{p}_{eff} &= 4\pi\varepsilon_1 A \hat{a}_z \\ &= 4\pi\varepsilon_1 K a^3 E_0 \hat{a}_z \end{aligned} \quad (1.16)$$

where K is known as the Clausius-Mossotti function, which models the contrast between the permittivity of the spherical particle and medium. The Clausius-Mossotti function, which is defined as:

$$K(\varepsilon_1, \varepsilon_2) = \frac{\varepsilon_2 - \varepsilon_1}{\varepsilon_2 + 2\varepsilon_1} = \frac{\varepsilon_2/\varepsilon_1 - 1}{\varepsilon_2/\varepsilon_1 + 2} \quad (1.17)$$

gives a measure of the relative strength as well as the direction of the polarization the particle undergoes. When $\varepsilon_2 > \varepsilon_1$, then $K > 0$ and the effective polarization, $\bar{p}_{eff}$, will be in the same direction as $\overline{E}_0$. In the case of $\varepsilon_2 < \varepsilon_1$, then $K < 0$ and $\bar{p}_{eff}$ is in line with $-\overline{E}_0$. A plot the Clausius-Mossotti function for a range of ε_2 is shown in Figure 1.4. The function is limited to $-0.5 \leq K \leq 1$ so even as $\varepsilon_2 \to \infty$, $K \to 1$.

1.4 Effective Dipole Moment of a Conductive Particle in a Uniform DC Field

The same analysis as used in Section 1.3 can be applied to a spherical conductive particle of radius a in a uniform DC field. If a particle with conductivity, σ_2, sus-

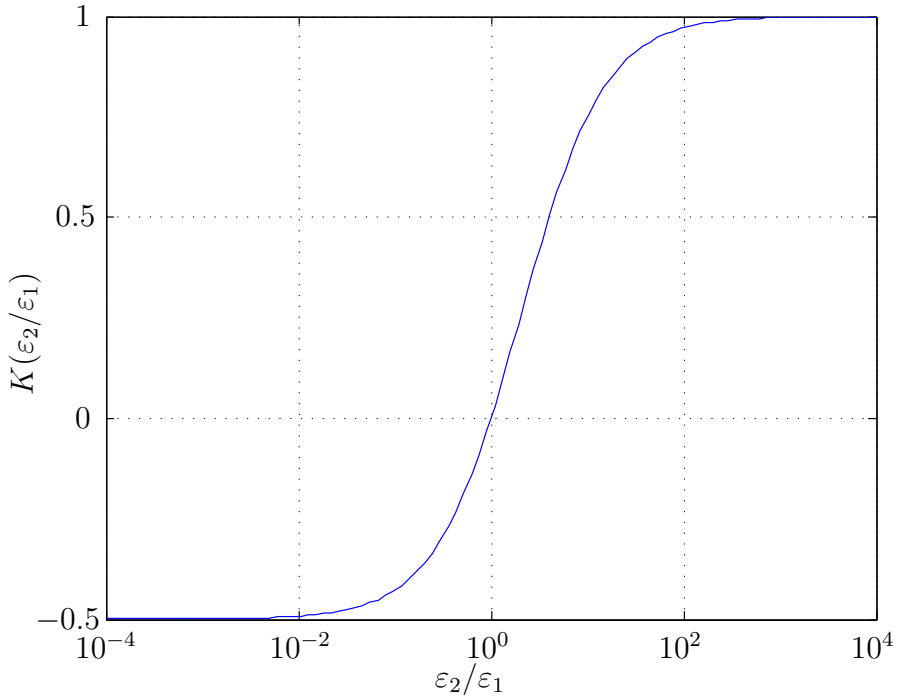

Figure 1.4: Clausius-Mossotti function.

pended in a solution with conductivity, σ_1, is subject to a uniform DC field, Laplace's equation, $\nabla \cdot (\sigma \nabla \phi) = 0$, must be satisfied inside and outside the spherical particle with the following boundary conditions applied:

$$\phi_1(r = a, \theta) = \phi_2(r = a, \theta) \tag{1.18a}$$

$$\sigma_1 E_{r1}(r = a, \theta) = \sigma_2 E_{r2}(r = a, \theta). \tag{1.18b}$$

When combined with (1.11), the same solution is found, with $p_{eff} = 4\pi\varepsilon_1 K a^3 E_0$. The only distinction being that $K(\varepsilon_1, \varepsilon_2)$ becomes:

$$K(\sigma_1, \sigma_2) = \frac{\sigma_2 - \sigma_1}{\sigma_2 + 2\sigma_1} = \frac{\sigma_2/\sigma_1 - 1}{\sigma_2/\sigma_1 + 2} \tag{1.19}$$

If the particle is a good conductor, that is $\sigma_2/\sigma_1 >> 1$, then the Clausius-Mossotti

function will approach $K = 1$ and the effective dipole moment will be:

$$p_{eff} \rightarrow p_0 = 4\pi\varepsilon_1 a^3 E_0 \tag{1.20}$$

1.5 Effective Dipole Moment of a Lossy Dielectric Particle in a Time Harmonic Uniform Electric Field

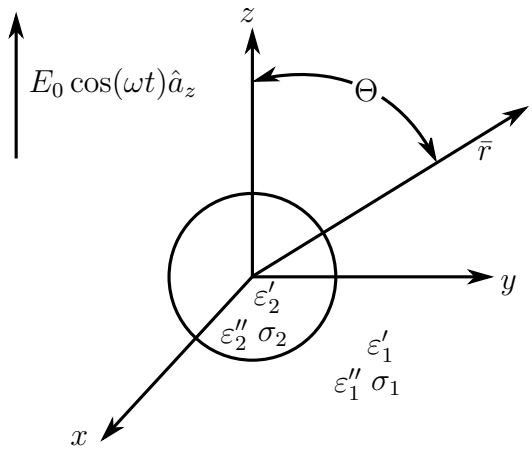

Figure 1.5: Lossy particle placed in a time harmonic non-uniform electric field.

In this section a lossy dielectric sphere is subject to a uniform time harmonic electric field of magnitude E_0 and angular frequency ω, described by:

$$\overline{E}_0(t) = \mathrm{Re}\left\{ E_0 \hat{a}_z e^{j\omega t} \right\}. \tag{1.21}$$

The particle, shown in Figure 1.5 with permittivity, ε_2, and conductivity, σ_2, is placed in a lossy medium of permittivity, ε_1, and conductivity, σ_1. The permittivities of the sphere and medium are extended from Section 1.3 to include the dielectric loss term, ε''. The permittivities of the sphere and medium take the form $\varepsilon_2 = \varepsilon_2' - j\varepsilon_2''$ and

$\varepsilon_1 = \varepsilon_1' - j\varepsilon_1''$, respectively.

General solutions for the electric potential inside and outside are found by solving Laplace's equation in complex form, $\nabla \cdot (\underline{\varepsilon} \nabla \phi) = 0$, where $\underline{\varepsilon} = \varepsilon' - j\varepsilon'' + \sigma/j\omega$. The solutions take the same form as (1.11), but are complex functions with complex constants. That is:

$$\underline{\phi}_1(r,\theta) = -E_0 r\cos(\theta) + \frac{\underline{A}\cos(\theta)}{r^2}, \qquad r \geq a \tag{1.22a}$$

$$\underline{\phi}_2(r,\theta) = -\underline{B} r\cos(\theta), \qquad r \leq a \tag{1.22b}$$

The first boundary condition, (1.12a), requiring the potential be continuous across the boundary remains unchanged. However, (1.12b) will be modified to include time-dependent accumulation of surface charge. In the time domain, the charge conservation condition, $\nabla \cdot \bar{J} = -\frac{\partial \sigma_f}{\partial t}$, at the surface must be satisfied:

$$J_{r1} - J_{r2} + \frac{\partial \sigma_f}{\partial t} = 0, \qquad r = a \tag{1.23}$$

$$\sigma_1 E_{r1} - \sigma_2 E_{r2} + \frac{\partial}{\partial t}\left(\varepsilon_1 E_{r1} - \varepsilon_2 E_{r2}\right) = 0, \qquad r = a \tag{1.24}$$

where $J_{r1} = \sigma_1 E_{r1}$ and $J_{r2} = \sigma_2 E_{r2}$ are the normal components of the ohmic current inside and outside the particle, respectively, and $\sigma_f = \varepsilon_1 E_{r1} - \varepsilon_2 E_{r2}$ is the free surface charge at the interface. Assuming that the permittivities are time invariant and the field inside and outside the particle are time harmonic, $\partial/\partial t \rightarrow j\omega$, the boundary condition becomes:

$$\sigma_1 E_{r1} - \sigma_2 E_{r2} + j\omega\varepsilon_1 E_{r1} - j\omega\varepsilon_2 E_{r2} = 0, \qquad r = a \tag{1.25}$$

$$\underline{\varepsilon}_1(\omega) E_{r1} = \underline{\varepsilon}_2(\omega) E_{r2}, \qquad r = a \tag{1.26}$$

where $\underline{\varepsilon}_1(\omega) = \varepsilon_1' - j\varepsilon_1'' + \sigma_1/j\omega$ and $\underline{\varepsilon}_2(\omega) = \varepsilon_2' - j\varepsilon_2'' + \sigma_2/j\omega$ are the complex permittivity of the medium and the particle, respectively. The coefficients for the general solution of Laplace's equation then become:

$$\underline{A} = \frac{\underline{\varepsilon}_2 - \underline{\varepsilon}_1}{\underline{\varepsilon}_2 + 2\underline{\varepsilon}_1} a^3 E_0 \tag{1.27a}$$

$$\underline{B} = \frac{3\underline{\varepsilon}_1}{\underline{\varepsilon}_2 + 2\underline{\varepsilon}_1} E_0 \tag{1.27b}$$

and effective dipole moment becomes the complex:

$$\bar{\underline{p}}_{eff} = 4\pi\varepsilon_1' \underline{K} a^3 \overline{E}_0 \tag{1.28}$$

The Clausius-Mossotti function becomes complex as well as a function of the frequency of the applied field:

$$\underline{K}(\underline{\varepsilon}_1, \underline{\varepsilon}_2) = \frac{\underline{\varepsilon}_2(\omega) - \underline{\varepsilon}_1(\omega)}{\underline{\varepsilon}_2(\omega) + 2\underline{\varepsilon}_1(\omega)} \tag{1.29}$$

1.6 Dielectrophoretic Force on a Lossless Particle in a Non-Uniform Field

From Section 1.1 the force on a dipole placed in a non-uniform external electric field is given by:

$$\overline{F}_{dipole} = \bar{p} \cdot \nabla \overline{E}_0 \tag{1.30}$$

where $\overline{E}_0 = E_x \hat{a}_x + E_y \hat{a}_y + E_z \hat{a}_z$ is an external electric field and $\bar{p}$ is the moment of the dipole. When a polarizable particle is placed in a medium with an external

electric field, $\overline{E}_0$, the changes in the total electric field can be approximated by the electric field of either a single infinitesimal dipole or a multipole in the same medium, located at the same position as the particle. The effective dipole moment, $\bar{p}_{eff}$, can be found for the particle by solving Laplace's equation using the boundary conditions on the surface of the particle and finding the total electric field. The effective dipole moment can then be used in combination with (1.30) to find the force on the particle:

$$\overline{F}_{particle} = \bar{p}_{eff} \cdot \nabla \overline{E}_0 \tag{1.31}$$

In the case of a lossless dielectric particle, $\bar{p}_{eff}$ is in line with $\overline{E}_0$ and the polarity is determined by the sign of K. If the field non-uniformities are on a larger scale than the particle then the polarization can be approximated by a single dipole potential. That is, $\bar{p}_{eff}$ is as defined in (1.16), and the effective instantaneous force on the particle is:

$$\begin{aligned}
\overline{F}_{particle} &= 4\pi\varepsilon_1 K a^3 \overline{E}_0 \cdot \nabla \overline{E}_0 \\
&= 4\pi\varepsilon_1 K a^3 \overline{E}_0 \cdot (\partial_x E_x \hat{a}_{xx} + \partial_y E_x \hat{a}_{xy} + \partial_z E_x \hat{a}_{xz} + \dots \\
&\qquad \partial_x E_y \hat{a}_{yx} + \partial_y E_y \hat{a}_{yy} + \partial_z E_y \hat{a}_{yz} + \dots \\
&\qquad \partial_x E_z \hat{a}_{zx} + \partial_y E_z \hat{a}_{zy} + \partial_z E_z \hat{a}_{zz}) \qquad (1.32) \\
&= 4\pi\varepsilon_1 K a^3 [(E_x \partial_x E_x + E_y \partial_x E_y + E_z \partial_x E_z)\, \hat{a}_x + \dots \\
&\qquad (E_x \partial_y E_x + E_y \partial_y E_y + E_z \partial_y E_z)\, \hat{a}_y + \dots \\
&\qquad (E_x \partial_z E_x + E_y \partial_z E_y + E_z \partial_z E_z)\, \hat{a}_z] \qquad (1.33)
\end{aligned}$$

$$= 4\pi\varepsilon_1 K a^3 [\frac{1}{2}\partial_x \left(E_x^2 + E_y^2 + E_z^2\right)\hat{a}_x + \ldots$$
$$\frac{1}{2}\partial_y \left(E_x^2 + E_y^2 + E_z^2\right)\hat{a}_y + \ldots$$
$$\frac{1}{2}\partial_x \left(E_x^2 + E_y^2 + E_z^2\right)\hat{a}_z] \tag{1.34}$$

where ∂_x, ∂_y, and ∂_z are the partial spacial derivatives with respect to x, y, and z, respectively, and $a_{i,j}$ denotes the element at (i,j) in the tensor array. Since $E_x^2 + E_y^2 + E_z^2 = |E_0|^2$, the total force on the particle takes the same form as the commonly used approximation of the dielectrophoretic force:

$$\overline{F}_{DEP} = 2\pi\varepsilon_1 a^3 K \nabla |E_0|^2 . \tag{1.35}$$

1.7 Dielectrophoretic Force on a Lossy Particle in a Non-Uniform Field

If a lossy particle in a lossy medium, each as shown in Figure 1.5 with a finite conductivity and dielectric loss, are subject to a non-uniform electric field, $\underline{\overline{E}}_0 = \underline{E}_x\hat{a}_x + \underline{E}_y\hat{a}_y + \underline{E}_z\hat{a}_z$, the particle will become polarized with an effective polarization, $\underline{\bar{p}}_{eff}$. Due to changes in the boundary conditions to allow for changes in surface charge, the effective polarization will be complex and will have a phase angle which can be interpreted as a lag of the particle polarization behind the external field. The instantaneous force on the particle will then take the form:

$$\overline{F}_{DEP}(t) = \mathrm{Re}\{\underline{\bar{p}}_{eff} e^{j\omega t}\} \cdot \nabla \mathrm{Re}\{\underline{\overline{E}}_0 e^{j\omega t}\} . \tag{1.36}$$

Assuming the external electric field and the polarization are time harmonic, all components of the field are in phase, and assuming field non-uniformities are on a

scale larger than the particle, the instantaneous force on the particle will be:

$$\overline{F}_{DEP}(t) = \left[\cos^2(\omega t)\right] \bar{\underline{p}}_{eff} \cdot \nabla \overline{\underline{E}}_0 \tag{1.37}$$

$$= \frac{1}{2}\left[1 + \cos(2\omega t)\right] 4\pi\varepsilon_1' \mathrm{Re}\{\underline{K}\}\, a^3 \overline{\underline{E}}_0 \cdot \nabla \overline{\underline{E}}_0 \tag{1.38}$$

$$= \left[1 + \cos(2\omega t)\right] 2\pi\varepsilon_1' \mathrm{Re}\{\underline{K}\}\, a^3 \nabla \left|\overline{\underline{E}}_0\right|^2 \tag{1.39}$$

Due to the relatively high viscosity (low Reynolds number environment) of the fluid, the double frequency term of the force is dampened and the constant term dominates. Taking the time average of force gives:

$$\left\langle \overline{F}_{DEP}(t) \right\rangle = \frac{1}{2}\mathrm{Re}\left\{\bar{\underline{p}}_{eff} \cdot \nabla \overline{\underline{E}}_0^*\right\} \tag{1.40}$$

$$= 2\pi\varepsilon_1' \mathrm{Re}\{\underline{K}\}\, a^3 \nabla E_{0,rms}^2 \tag{1.41}$$

where $\langle f(t) \rangle$ denotes the time average of $f(t)$, and $E_{0,rms}$ is the root mean square magnitude of the external electric field. The real part of the Clausius-Mossotti factor is what determines the relative strength and polarity of the induced force, as well as providing a frequency dependence of the force.

1.8 Electrical Double Layer

When a particle is placed in a liquid with non-zero conductivity, an electrical double layer is formed at the interface between the particle and the liquid which creates a finite surface conductivity. As a low-loss particle becomes smaller, surface conductivity will play a larger role in the overall dielectrophoretic response since currents move more easily around the outside of the particle making the total conductivity of the particle increase. The decreasing total surface resistance can be incorporated into

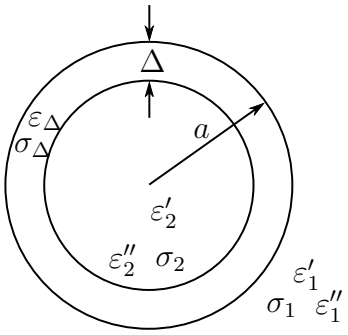

Figure 1.6: Lossy particle with equivalent double layer.

the total complex particle permittivity by using the shell method, which adds a small conductive layer of thickness, $\Delta << a$, with conductivity, σ_Δ, and permittivity, ε_Δ. An illustration of the shell method equivalent particle is shown in Figure 1.6. Assuming $\frac{\sigma_\Delta}{\omega} >> \varepsilon_\Delta$, making the layer conductive, and using the shell method described in Appendix C of Jones [10], the effective complex permittivity will become:

$$\underline{\varepsilon}_{2,eff} = \frac{\sigma_\Delta}{j\omega}\left\{\frac{(1+\frac{\Delta}{a})^3 + 2\left(\frac{\underline{\varepsilon}_2 - \sigma_\Delta/j\omega}{\underline{\varepsilon}_2 + 2\sigma_\Delta/j\omega}\right)}{(1+\frac{\Delta}{a})^3 - \left(\frac{\underline{\varepsilon}_2 - \sigma_\Delta/j\omega}{\underline{\varepsilon}_2 + 2\sigma_\Delta/j\omega}\right)}\right\}. \tag{1.42}$$

Since $\frac{\Delta}{a} << 1$, $(1+\frac{\Delta}{a})^3 \approx 1 + 3\frac{\Delta}{a}$:

$$\underline{\varepsilon}_{2,eff} \approx \frac{\sigma_\Delta}{j\omega}\left\{\frac{(1+3\frac{\Delta}{a})(\underline{\varepsilon}_2 + 2\sigma_\Delta/j\omega) + 2\left(\underline{\varepsilon}_2 - \sigma_\Delta/j\omega\right)}{(1+3\frac{\Delta}{a})(\underline{\varepsilon}_2 + 2\sigma_\Delta/j\omega) - (\underline{\varepsilon}_2 - \sigma_\Delta/j\omega)}\right\} \tag{1.43}$$

$$\approx \frac{\sigma_\Delta}{j\omega}\left\{\frac{3\underline{\varepsilon}_2 + \frac{6\sigma_\Delta}{j\omega}\frac{\Delta}{a}}{\frac{3\sigma_\Delta}{j\omega} + 3\underline{\varepsilon}_2\frac{\Delta}{a}}\right\} \tag{1.44}$$

$$\approx \frac{\underline{\varepsilon}_2 + \frac{2\sigma_\Delta}{j\omega}\frac{\Delta}{a}}{1 + \frac{\underline{\varepsilon}_2 j\omega}{\sigma_\Delta}\frac{\Delta}{a}}. \tag{1.45}$$

Since $(1+x)^{-1} \approx (1-x)$ for $x << 1$:

$$\varepsilon_{2,eff} \approx \left(\varepsilon_2 + \frac{2\sigma_\Delta}{j\omega}\frac{\Delta}{a}\right)\left(1 - \frac{\varepsilon_2 j\omega}{\sigma_\Delta}\frac{\Delta}{a}\right) \tag{1.46}$$

$$\approx \varepsilon_2 + \frac{2\sigma_\Delta}{j\omega}\frac{\Delta}{a} - \frac{\varepsilon_2^2 j\omega}{\sigma_\Delta}\frac{\Delta}{a} - 2\varepsilon_2 j\omega\frac{\Delta^2}{a^2} \tag{1.47}$$

$$\approx \varepsilon_2 + \frac{2\Delta\sigma_\Delta}{j\omega a} \tag{1.48}$$

$$= \varepsilon_2 + \frac{2K_s}{j\omega a}, \tag{1.49}$$

where $K_s = \Delta\sigma_\Delta$ is the surface conductance of the particle. Incorporating this term into the conductivity of the particle, the effective conductivity takes the form:

$$\sigma_2 = \sigma_{bulk} + \frac{2K_s}{a} \tag{1.50}$$

and the complex particle permittivity remains $\varepsilon_2(\omega) = \varepsilon_2' - j\varepsilon_2'' + \sigma_2/j\omega$. Here σ_{bulk} is the bulk conductivity of the particle and K_s is the surface conductance, a value that will depend on the properties of the particle and medium.

1.9 Clausius-Mossotti Function for Various Particle Types

To get a sense of the behavior of different particle types in a non-uniform time harmonic field, this section will explore the Clausius-Mossotti function for a few particle types. The types of particles described will include: metallic particles, lossless and non-dispersive lossy homogeneous dielectric particles (polystyrene spheres), and biological cells (yeast). Figure 1.7 shows a plot of the Clausius-Mossotti functions for the inorganic particle types, each with a radius of 3 µm, and parameters as specifed

in Table 1.2. The lossy particle described in Table 1.2 has the double layer surface conductivity include in the conductivity term, as included in (1.50).

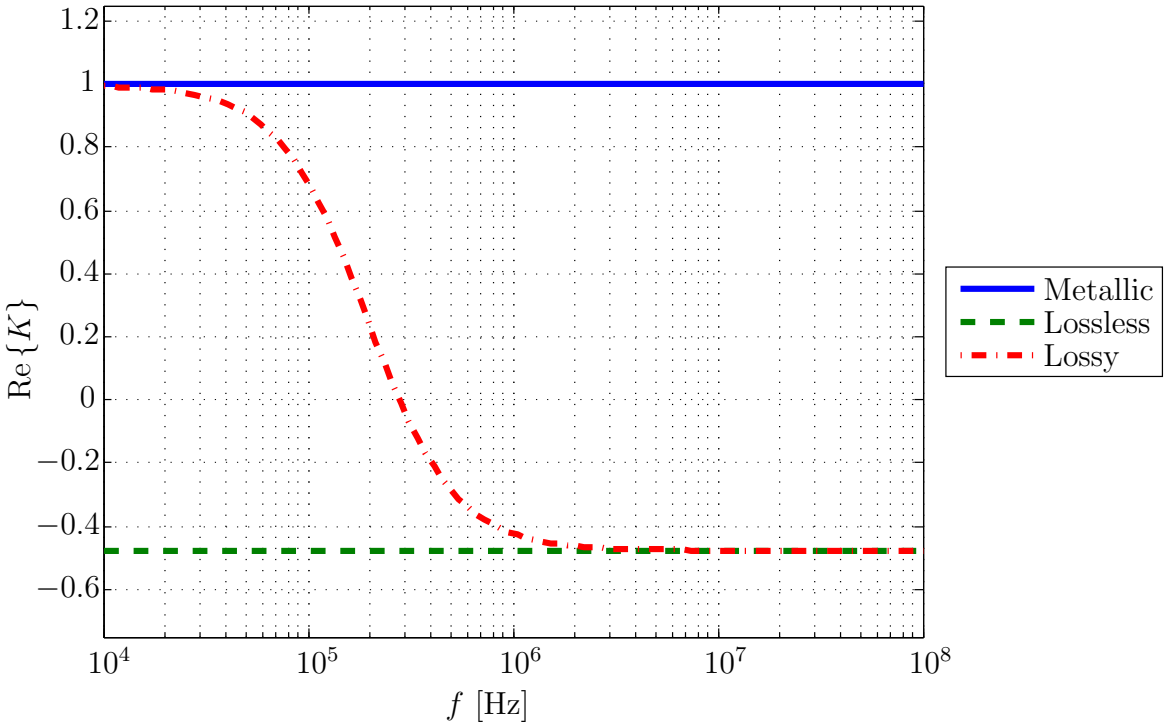

Figure 1.7: Clausius-Mossotti function for metallic, homogeneous lossless and lossy dielectric particles in a low loss medium.

For a metallic particle in a low loss medium, the Clausius-Mossotti factor remains:

$$\begin{aligned} \underline{K} &= \frac{\underline{\varepsilon}_2 - \underline{\varepsilon}_1}{\underline{\varepsilon}_2 + 2\underline{\varepsilon}_1} \\ &\approx 1. \end{aligned} \tag{1.51}$$

Since $\sqrt{|\varepsilon_1'| + |\sigma_1/\omega|} << |\underline{\varepsilon}_2| \approx \sigma_2/\omega$. Giving the metallic particle a constant Clausius-Mossotti function of 1, meaning it will always experience a positive DEP force, pulling it into areas of higher electric field.

For a lossless dielectric particle in a low loss medium, $\underline{\varepsilon}_2 \approx \varepsilon_2$, $\varepsilon_1' >> \sigma_1/\omega$, the

Table 1.2: Clausius-Mossotti function plot parameters.

	Parameter	**Value**
	Particle Radius	$3\,\mu m$
	ε_0	$8.854\,187\,82 \times 10^{-12}\ \frac{F}{m}$
DI water	ε_1'	$78\varepsilon_0$
	ε_1''	0
	σ_1	$1 \times 10^{-6}\ \frac{S}{m}$
Metallic Particle (Silver colloid)	ε_2'	ε_0
	σ_2	$1 \times 10^{8}\ \frac{S}{m}$
Lossless Particle (Lossless PSS)	ε_2'	$2.5\varepsilon_0$
	σ_2	0
Lossy Particle (Lossy PSS)	ε_2'	$2.5\varepsilon_0$
	σ_2	$1.7 \times 10^{-3}\ \frac{S}{m}$

Clausius-Mossotti function will be:

$$\underline{K} = \frac{\underline{\varepsilon}_2 - \underline{\varepsilon}_1}{\underline{\varepsilon}_2 + 2\underline{\varepsilon}_1} \approx \frac{\varepsilon_2' - \varepsilon_1'}{\varepsilon_2' + 2\varepsilon_1'}. \tag{1.52}$$

The particle will experience either a constant positive or negative DEP force depending on whether $\varepsilon_2' > \varepsilon_1'$ or $\varepsilon_2' < \varepsilon_1'$, respectively.

For a lossy particle in a lossy medium, from Section 1.7, the term, $\mathrm{Re}\{\underline{K}\}$, is the only frequency dependent term in the time average DEP force. Here the electrical double layer is included in the particle conductivity, that is $\sigma_2 = \sigma_{2,bulk} + 2\frac{K_s}{a} = 1.7\,\mathrm{mS\,m^{-1}}$ when $K_s = 2.56\,\mathrm{nS}$ [11]. Starting from the general expression for the Clausius-Mossotti factor, and assuming $\varepsilon_1'' = \varepsilon_2'' = 0$,

$$\mathrm{Re}\{\underline{K}\} = \mathrm{Re}\left\{\frac{\underline{\varepsilon}_2 - \underline{\varepsilon}_1}{\underline{\varepsilon}_2 + 2\underline{\varepsilon}_1}\right\} \tag{1.53}$$

$$= \mathrm{Re}\left\{\frac{\varepsilon_2 + \sigma_2/j\omega - \varepsilon_1 - \sigma_1/j\omega}{\varepsilon_2 + \sigma_2/j\omega + 2\varepsilon_1 + 2\sigma_1/j\omega}\right\} \tag{1.54}$$

$$= \frac{(\sigma_2 - \sigma_1)(\sigma_2 + 2\sigma_1) + \omega^2(\varepsilon_2 - \varepsilon_1)(\varepsilon_2 + 2\varepsilon_1)}{(\sigma_2 + 2\sigma_1)^2 + \omega^2(\varepsilon_2 + 2\varepsilon_1)^2} \tag{1.55}$$

$$= \frac{K_0 + \omega^2 \tau_{MW}^2 K_\infty}{1 + \omega^2 \tau_{MW}^2} \tag{1.56}$$

$$= K_\infty - \frac{K_\infty - K_0}{1 + \omega^2 \tau_{MW}^2}. \tag{1.57}$$

Here K_0 and K_∞ are the low and high frequency limits of the Clausius-Mossotti function, respectively, and τ_{MW} is the Maxwell-Wagner charge relaxation time. As defined in [2, 10, 12, 13, 14]:

$$K_0 = \lim_{\omega \to 0} \underline{K} = \frac{\sigma_2 - \sigma_1}{\sigma_2 + 2\sigma_1} \tag{1.58}$$

$$K_\infty = \lim_{\omega \to \infty} \underline{K} = \frac{\varepsilon_2 - \varepsilon_1}{\varepsilon_2 + 2\varepsilon_1} \tag{1.59}$$

$$\tau_{MW} = \frac{\varepsilon_2 + 2\varepsilon_1}{\sigma_2 + 2\sigma_1}, \tag{1.60}$$

making the frequency response governed by a single Maxwell-Wagner relaxation process centered at $f_{MW} = 1/2\pi\tau_{MW}$. Specifically, for the lossy particle with parameters shown in Table 1.2, the DEP response, shown in Figure 1.7, is characterized by low and high $\mathrm{Re}\{K\}$ limits of $K_0 = 0.9982$ and $K_\infty = -0.4764$, respectively, as well as a center frequency of $f_{MW} = 193\,\mathrm{kHz}$.

A major application of DEP techniques is in single cell diagnostics. The commonly used, simplified model of a biological cell is the shelled sphere, in which the cell is modeled as a lossy dielectric sphere with multiple shells of various thicknesses and permittivities. These shells, made to represent the nucleoplasm, nuclear envelope, cytoplasm, cytoplasmic membranes, cell wall, and other layers of the particular cell of interest. As an example, Figure 1.8 shows a model of a baker's yeast cell (*Saccharomyces cerevisiae*), as described in [2, 15]. The permittivity, conductivity, and thickness of each layer has been experimentally determined by fitting to data

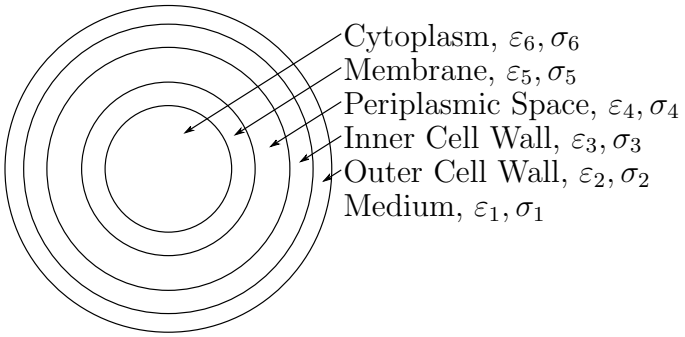

Figure 1.8: Shelled model of a baker's yeast cell (not to scale).

collected through electrorotation (ROT) [15]. The effective complex permittivity of the cell is found by using a similar method to that in Section 1.8. Starting from the innermost sphere, the cytoplasm, and the innermost shell, the membrane, the equivalent effective complex permittivity for the cytoplasm and the membrane, $\varepsilon_{6,eff}$, is found [2, 10, 12]:

$$\varepsilon_{6,eff} = \varepsilon_{mem} \left[\frac{\left(\frac{r_{cyt}+d_{mem}}{r_{cyt}}\right)^3 + 2\left(\frac{\varepsilon_{cyt}-\varepsilon_{mem}}{\varepsilon_{cyt}+2\varepsilon_{mem}}\right)}{\left(\frac{r_{cyt}+d_{mem}}{r_{cyt}}\right)^3 - \left(\frac{\varepsilon_{cyt}-\varepsilon_{mem}}{\varepsilon_{cyt}+2\varepsilon_{mem}}\right)} \right] \tag{1.61}$$

If this method is continued through all the layers eventually an equivalent complex permittivity for the entire cell is found:

$$\varepsilon_{n,eff} = \varepsilon_n \left[\frac{\left(\frac{r_{cyt}+\sum_{i=n}^{6} d_i}{r_{cyt}+\sum_{i=n+1}^{6}}\right)^3 + 2\left(\frac{\varepsilon_{n+1,eff}-\varepsilon_n}{\varepsilon_{n+1,eff}+2\varepsilon_n}\right)}{\left(\frac{r_{cyt}+\sum_{i=n}^{6} d_i}{r_{cyt}+\sum_{i=n+1}^{6}}\right)^3 - \left(\frac{\varepsilon_{n+1,eff}-\varepsilon_n}{\varepsilon_{n+1,eff}+2\varepsilon_n}\right)} \right], \qquad 2 \geq n \leq 5 \tag{1.62}$$

where $n = 1$, $n = 2$,...,$n = 6$ denotes the layers, medium, outer cell wall, inner cell wall, periplasmic space, cytoplastic membrane, and cytoplasm, respectively. Using the above iterative algorithm to calculate the effective complex permittivity, with

parameters shown in Table 1.3, the Clausius-Mossotti function was plotted and is shown in Figure 1.9. With each layer of added dielectric material, an additional Maxwell-Wagner relaxation process is observed, giving the cell a more complex frequency response than that of the lossy homogeneous sphere. The Clausius-Mossotti function for a cell with N lossy dielectric layers takes the form [10]:

$$\mathrm{Re}\{\underline{K}\} = K_\infty - \sum_{i=1}^{N} \frac{\Delta K_i}{1 + \omega^2 \tau_{MW,i}^2} \tag{1.63}$$

where K_∞ is the high frequency limit of $\mathrm{Re}\{\underline{K}(\omega)\}$, ΔK_i is the change in $\mathrm{Re}\{\underline{K}\}$ for a given relaxation time, $\tau_{MW,i}$. The values of ΔK_i and τ_i can be found when τ_i are widely separated; however, ΔK_i and τ_i cannot be reduced to simple expressions like in the case of a lossy homogeneous sphere, and the Clausius-Mossotti function has to be recalculated for each change in parameters [10].

The following chapter will describe the detection method used for sensing the response of particles to the applied DEP force. It will also describe the design, fabrication, and simulation of the microelectrodes used to detect particles and apply the DEP force.

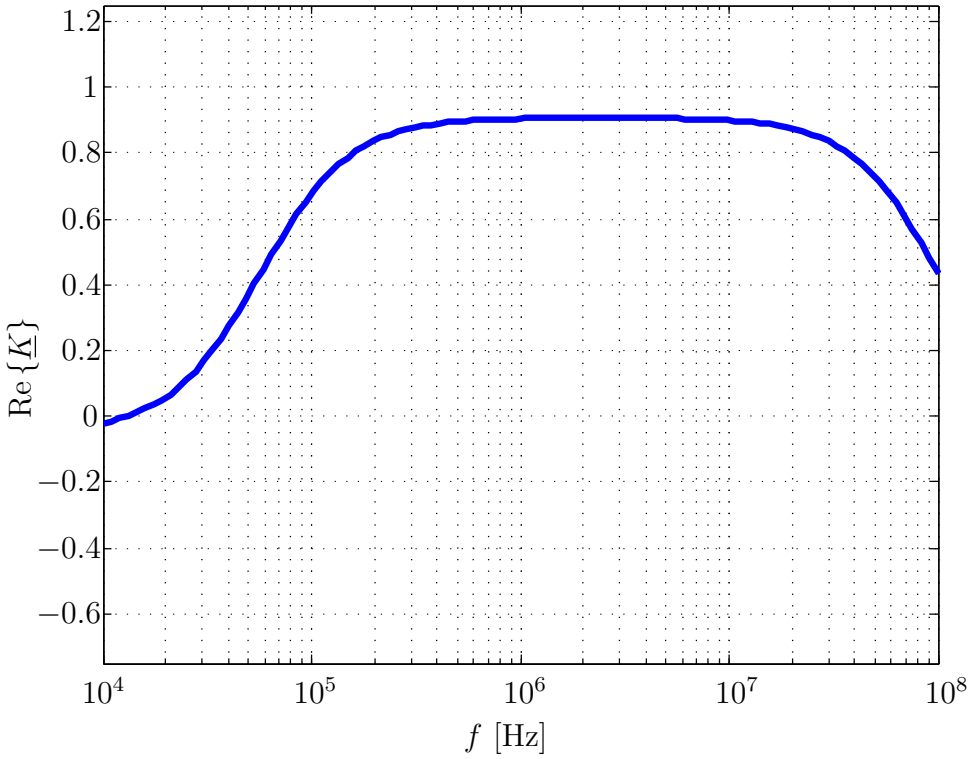

Figure 1.9: Clausius-Mossotti function of a baker's yeast cell (Saccharomyces cerevisiae), with parameters according to Table 1.3.

Table 1.3: Clausius-Mossotti function plot parameters for biological cell (S. cerevisiae)[2].

Layer	**Radius/Thickness**	ε	σ $[\frac{\mu S}{m}]$
Cytoplasm (cyt)	3 µm	$51\varepsilon_0$	120
Cytoplasmic Membrane (mem)	3.5 nm	$3\varepsilon_0$	3.02e-4
Periplasmic Space (pps)	25 nm	$14.4\varepsilon_0$	0.41
Inner Cell Wall (icw)	110 nm	$60\varepsilon_0$	0.304322
Outer Cell Wall (ocw)	50 nm	$5.9\varepsilon_0$	2
Medium		$78\varepsilon_0$	0.334

Chapter 2

Experimental Setup: Microelectrode Design and DEP Simulation

Experimental measurement of the dielectrophoretic force exerted on a particle required that a system be designed to both apply a non-uniform electric field in order to actuate the particle, and simultaneously measure the response to allow for an estimate of the polarity and magnitude of the force and determination of the Clausius-Mossotti function. The particles, biological cells and non-biological particles, to be actuated and measured by the system range in size from 1 µm to 20 µm. Electrode dimensions must be small to create a strong enough electric field, keeping $\nabla|\overline{E}_0|^2$ large enough to create a measurable force, while keeping the source voltage at a reasonable level for available lab equipment. The non-uniformities in the DEP electric field must also be small across the largest particle in order for the dipole approximation to be accurate and all higher order polarization terms be negligible. Using these criteria, a set of electrodes was designed to allow for DEP actuation as well as sensing of particle

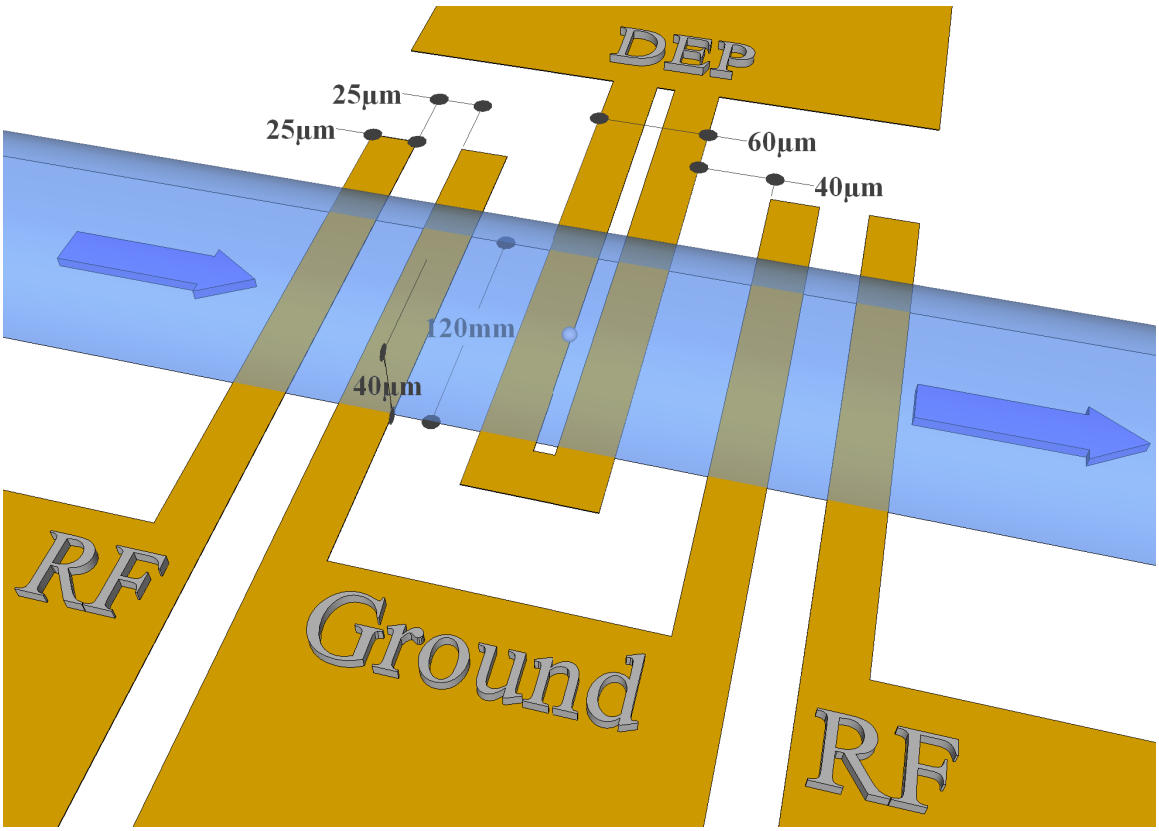

Figure 2.1: Channel and electrode configuration.

position, with use of an electrode capacitance measurement. Figure 2.1 shows a 3D view of the final electrode array design with a microfluidic channel running over the electrode array. A microfluidic channel is used to move particles over the sensing and actuation electrodes to measure their translation due to an applied DEP force.

The microfluidic chip, further discussed in Chapter 3, was designed at the University of Manitoba and fabricated using the Sensonit process [16] by Micronit Microfluidics BV in conjunction with CMC Microsystems to flow multiple particles over the electrode array. A 2D graphical representation of the channel and electrode configuration is shown in Figure 2.2. The electrode array consists of two measurement zones, shown by $\overline{E}_{RF}$ in the figure, to measure the height of the particle before and after the DEP force is applied. The remaining electrode gaps are two DEP zones,

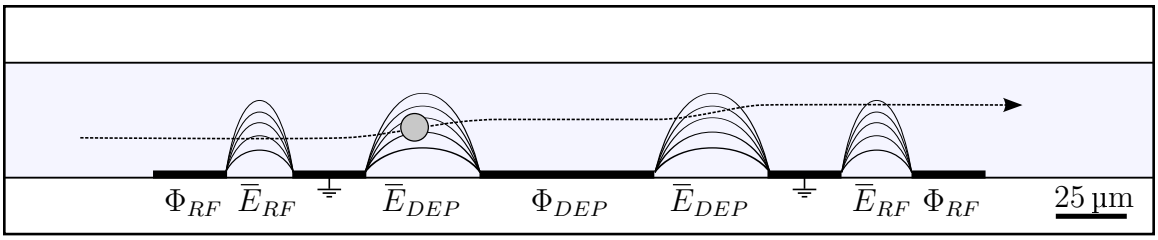

Figure 2.2: As the particle moves over the electrodes the initial height is measured by the first half of the sensing field, next the particle is actuated and is again measured.

shown by $\overline{E}_{DEP}$ in the figure, wherein the passing particle is actuated using the DEP force.

The particles used in experiments are polystyrene microspheres, with nominal diameters of 4.5 µm, 6 µm, and 10 µm. They are manufactured by Polysciences, Inc. to provide a precise monodisperse particle size distribution [17]. Polystyrene spheres (PSS) were chosen because of their consistent dielectric properties and size, as well as their high dielectric contrast with the background medium, deionized water.

This chapter will describe finite element simulations of the sensing and DEP electric fields. Using the simulated fields and analytical expressions, the theoretical induced sensing electrode capacitance changes are found and the theoretical particle trajectories are simulated.

2.1 Theoretical Capacitance Change

Sensing of the particle position is done by measuring the capacitance of the set of sensing electrodes as the particle flows through the sensing field. The theoretical capacitance change corresponding to a passing particle can be found analytically by finding the energy change caused by the presence of the particle. The channel is first analyzed without the particle and with a homogeneous fluid medium of permittivity, ε_1', dielectric loss, ε_1'', and conductivity, σ_1. The sensing electrodes, shown in Figure 2.2

as the two electrodes on the outside edges, are energized with the time harmonic RMS potential, Φ_{RF}, oscillating at angular frequency, ω. The total stored energy of the detection zone, defined as the region in the channel surrounding the sensing electrodes, is equal to:

$$W_0 = \frac{1}{2} C_0 \Phi_{RF}^2 \tag{2.1}$$

where C_0 is the electrode capacitance [18, 1]. Setting Φ_{RF} constant for a given experiment, any change in capacitance will result in a change in energy:

$$\Delta W = \frac{1}{2} \Delta C \Phi_{RF}^2 \tag{2.2}$$

Now if a homogeneous lossy dielectric sphere is introduced to the detection zone, there is a change in the total stored energy of the system. The sphere has a radius, a, permittivity, ε_2', dielectric loss, ε_2'', and conductivity, $\sigma_2 = \sigma_{bulk} + \frac{2K_s}{a}$ where σ_{bulk} and K_s are the bulk particle conductivity and the surface conductance, respectively. The total energy of the detection zone then becomes:

$$W = \frac{1}{2} C_0 \Phi_{RF}^2 + \frac{1}{2} \mathrm{Re}\left\{ \int_V \overline{E}_{RF} \cdot \underline{\overline{P}}_{part}^* dV \right\} \tag{2.3}$$

$$= \frac{1}{2} C_0 \Phi_{RF}^2 + \frac{1}{2} \mathrm{Re}\left\{ \int_{V_{part}} \overline{E}_{RF} \cdot \underline{\overline{P}}_{part}^* dV_{part} \right\} \tag{2.4}$$

where V is the volume of the detection zone, $\overline{E}_{RF} = -\nabla \Phi_{RF}$ is the RMS electric field generated by the electrode potential, and $\underline{\overline{P}}_{part}^*$ is the complex conjugate of the RMS particle polarization. Since $\underline{\overline{P}}_{part}$ is zero outside the particle, then the volume integral is reduced to the region inside the particle, V_{part} [18, 1]. The change in stored energy

then becomes:

$$\Delta W = W - W_0 = \frac{1}{2}\mathrm{Re}\left\{\int_{V_{part}} \overline{E}_{RF} \cdot \underline{\overline{P}}^*_{part} dV_{part}\right\} \tag{2.5}$$

$$\frac{1}{2}\Delta C \Phi^2_{RF} = \frac{1}{2}\mathrm{Re}\left\{\int_{V_{part}} \overline{E}_{RF} \cdot \underline{\overline{P}}^*_{part} dV_{part} dV\right\} \tag{2.6}$$

The change in electrode capacitance due to the presence of the particle then becomes:

$$\Delta C = \frac{1}{\Phi^2_{RF}}\mathrm{Re}\left\{\int_{V_{part}} \overline{E}_{RF} \cdot \underline{\overline{P}}^*_{part} dV_{part}\right\} \tag{2.7}$$

The particle polarization is defined as in [18, 1]:

$$\underline{\overline{P}}_{part} = (\underline{\varepsilon}_2 - \underline{\varepsilon}_1)\underline{\overline{E}}_{part} \tag{2.8}$$

where $\underline{\overline{E}}_{part}$ is the electric field inside the particle. If the non-uniformities in the electric field are small over the particle, the dipole approximation will be reasonably accurate, and the electric field inside the particle can be found by combining (1.22b) and (1.27b), defined in Section 1.5:

$$\underline{\overline{E}}_{part} = \frac{3\underline{\varepsilon}_1}{\underline{\varepsilon}_2 + 2\underline{\varepsilon}_1}\overline{E}_{RF} \tag{2.9}$$

$$\underline{\overline{P}}_{part} = 3\varepsilon_1 \underline{K}\overline{E}_{RF} \tag{2.10}$$

The change in energy can then be found by integrating the time average energy over the total volume of the detection zone with and without the particle. Using (2.7)

and (2.10) the change in electrode capacitance then becomes [18, 1]:

$$\Delta C = \frac{1}{\Phi_{RF}^2}\mathrm{Re}\left\{\int_{V_{part}} \overline{E}_{RF}\cdot\left[3\underline{\varepsilon}_1\underline{K}\overline{E}_{RF}\right]^* dV_{part}\right\} \tag{2.11}$$

$$= 3V_{part}\mathrm{Re}\{[\underline{\varepsilon}_1\underline{K}]^*\}\,\frac{E_{RF}^2}{\Phi_{RF}^2}. \tag{2.12}$$

In order to further simplify the capacitance change expression approximate values can be used for the complex permittivity of the medium and particle. In the experimental apparatus used for DEP force cytometry, sensing electrodes are excited at frequencies close to 1.58 GHz. As calculated in [12] and [19], the relative permittivity and dielectric loss for DI water at 25 °C can be found using the formula:

$$\underline{\varepsilon}_r(\omega) = \varepsilon_{inf} + \frac{\varepsilon_s - \varepsilon_2}{1 + j\omega\tau_1} + \frac{\varepsilon_2 - \varepsilon_{inf}}{1 + j\omega\tau_2} \tag{2.13}$$

$$\underline{\varepsilon}_r(\omega) = 4.57 + \frac{78.32 - 6.32}{1 + j\omega 9.6\times10^{-12}\,\mathrm{s}} + \frac{6.32 - 4.57}{1 + j\omega 1.2\times10^{-12}\,\mathrm{s}} \tag{2.14}$$

making $\varepsilon_1' = 77.67\varepsilon_0$ and $\varepsilon_1'' = 6.82\varepsilon_0$ at 1.58 GHz. Since $\varepsilon_1'' << \varepsilon_1'$, for the sake of simplicity the dielectric loss will be assumed negligible and the permittivity will be approximated as $78\varepsilon_0$ for both the high frequency capacitance changes and the DEP force estimates. The DI water conductivity was measured using a conductivity meter prior to each experiment and ranged from 64 $\frac{\mu S}{m}$ to 593 $\frac{\mu S}{m}$ depending on time exposed to air. Polystyrene permittivity is $\varepsilon_2' \sim 2.55\varepsilon_0$ and dielectric loss is low ($\varepsilon_2'' \sim 0.001\varepsilon_0$), so it can be neglected [2, 11]. Particle conductivity takes the form, $\sigma_2 = \sigma_{bulk} + \frac{2K_s}{a}$ which will depend on particle size. However, with the frequency being in the gigahertz range, the Clausius-Mossotti function reaches its high frequency limit,

since $\varepsilon_1 << \sigma_1/\omega$ and $\varepsilon_2 << \sigma_2/\omega$, such that:

$$K_\infty = \lim_{\omega\to\infty} \frac{\underline{\varepsilon}_2 - \underline{\varepsilon}_1}{\underline{\varepsilon}_2 + 2\underline{\varepsilon}_1} \tag{2.15}$$

$$= \frac{\varepsilon_2' - \varepsilon_1'}{\varepsilon_2' + 2\varepsilon_1'} \tag{2.16}$$

making the particle detection rather insensitive to changes in fluid and particle conductivity. The change in capacitance due to a passing particle, including the high frequency approximations, then becomes:

$$\Delta C = 4\pi a^3 \varepsilon_1' K_\infty \frac{E_{RF}^2}{\Phi_{RF}^2} \tag{2.17}$$

and for PSS with parameters as previously specified

$$\Delta C = 4\pi a^3 \left[3.29 \times 10^{-10}\right] \frac{E_{RF}^2}{\Phi_{RF}^2}. \tag{2.18}$$

Capacitive detection of particles passing over the electrode array generates time domain "capacitance signatures". In order to predict and analyze the capacitance signatures resulting from passing particles, a finite element simulation was done to simulate the only position dependent portion of the capacitance change, $\frac{E_{RF}^2}{\Phi_{RF}^2}$, in (2.17).

2.2 Finite Element Capacitance Change Simulation

A 2D model of the electrode configuration was created in COMSOL Multiphysics, with use of the Electric Currents partial differential equation type, to compute the electric field, $\overline{E}_{RF} = -\nabla V$, created by the sensing electrodes. This field will be used

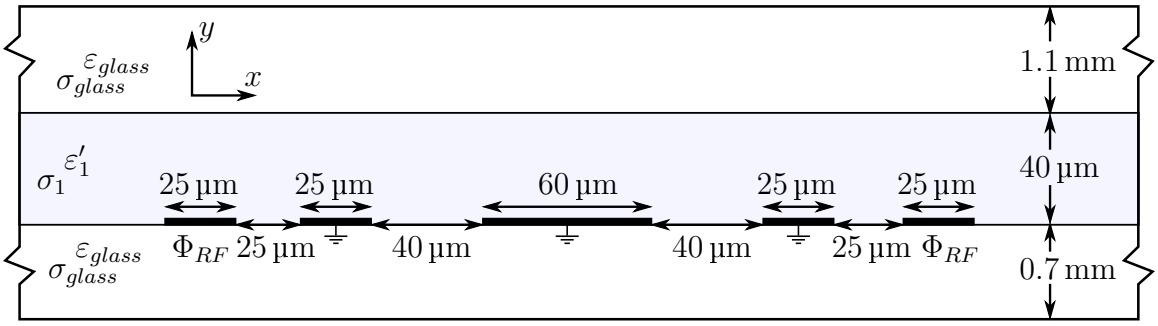

Figure 2.3: Model and parameters for COMSOL simulation of the sensing field, E_{RF}.

to find the expected capacitance signatures of passing polystyrene spheres. A 2D simulation was chosen to approximate the electric field as the electrode configuration is transversely symmetric to the fluid flow and since it shortens simulation time and simplifies the interpretation and visualization of the resulting data. The 2D approximation assumes that passing particles are in the middle third of the channel, where the channel height is 40 µm, or that particles are not near the walls of the channel.

A diagram of the electrode configuration within the channel is shown in Figure 2.3. Sensing electrode spacing and width are set to 25 µm and the total separation, center to center, of the electrode pairs to 215 µm. The dielectric properties of the model are set according to Table 2.1. Channel height is set to 40 µm, the length to 2 mm, and the permittivity and conductivity to $78\varepsilon_0$ and $100\,\frac{\mu S}{m}$, respectively. The channel is etched into borosilicate glass with a permittivity $4.8\varepsilon_0$ and negligible losses. As per the Sensonit fabrication documentation, the top layer and bottom layer glass thicknesses are 1.1 mm and 0.7 mm, respectively [16]. The inside sensing electrodes are set to ground, simultaneously providing ground for the DEP field during experiments. The DEP electrode is also set to ground with respect to the sensing electrode potential. The outer sensing electrode potential is set to $\sqrt{2}$V magnitude so the electrode potential is 1 V RMS, making $E_{RF}^2/\Phi_{RF}^2 = E_{RF}^2$. A Neumann (insulating) boundary condition, $\hat{a}_n \cdot \bar{J} = 0$, was set for the outside edges of the simulation with the assump-

Table 2.1: Parameters for COMSOL simulation of sensing field.

Parameter	**Value**
ε_1	$78\varepsilon_0$
ε_0	$8.854\,187\,82 \times 10^{-12}\ \frac{\mathrm{F}}{\mathrm{m}}$
σ_1	$100 \times 10^{-6}\ \frac{\mathrm{S}}{\mathrm{m}}$
ε_{glass}	$4.8\varepsilon_0$ [12]
σ_{glass}	~ 0 [12]
Φ_{RF}	$1\mathrm{V}_{rms}$

tion that the edges are far enough from the electrodes that the field would be near 0.

The solution to the complex form of Laplace's equation, $\nabla \cdot (\varepsilon \nabla V) = 0$, was found for a frequency of 1.58 GHz within detection zone. The electric field was calculated from the spatially dependent potential solution using, $\overline{E}_{RF} = -\nabla V$. Figure 2.4 shows the squared RMS electric field magnitude over the RMS electrode potential, E_{RF}^2/Φ_{RF}^2, as a function of x position for a variety of heights above the electrodes. Heights are measured from the bottom of the channel to the center of the particle. A particle with a height of 4 µm corresponds to a maximum E_{RF}^2/Φ_{RF}^2 of $10.2 \times 10^8\,\mathrm{m}^{-2}$ and a particle with a height of 34 µm corresponds to a maximum E_{RF}^2/Φ_{RF}^2 of $0.96 \times 10^8\,\mathrm{m}^{-2}$. Generally, as the height above the electrodes is increased the total field decreases and the electrode edges become less pronounced in the field curves, causing maxima to occur over the electrode gaps rather than the electrode edges.

Upon simulating the normalized sensing electric field, changes in capacitance due to the presence of a particle could then be found by scaling based on particle size, dielectric contrast, medium permittivity and actual electrode potential using (2.17). Figure 2.5 shows the capacitance signature for unactuated (constant elevation) passing polystyrene spheres of radii, 2.3265 µm, 2.7485 µm, and 4.985 µm, the particle sizes used during experiments, in DI water for a constant elevation of 10 µm. The

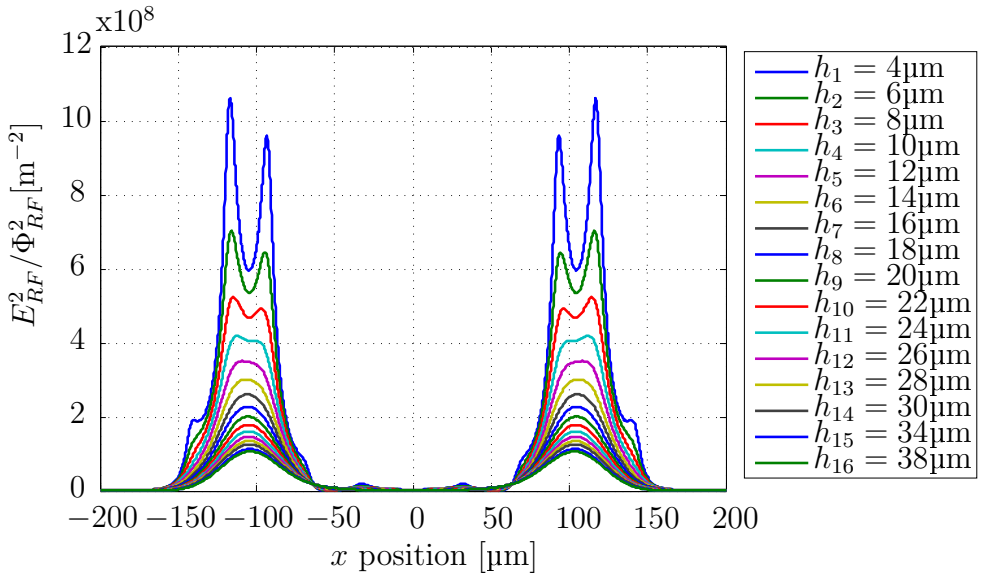

Figure 2.4: COMSOL simulation results showing the square of the RMS electric field magnitude over the square of the RMS electrode potential.

capacitance signatures can now be found for any given particle size and height. These plots should match the capacitance signal voltage measured experimentally when a particle passes over the sensing electrodes after scaling based on capacitance sensitivity and particle velocity. Experimental capacitance signals may differ slightly when compared with the theoretical curves if the particle is close to the electrodes. This is due to the averaging effect of the dielectric particle when field non-uniformities are large compared to the particle size.

Given the solution for E^2_{RF}/Φ^2_{RF}, the next step is to simulate the force exerted on a particle and find particle trajectories for each initial particle height and initial velocity. From these particle trajectories theoretical capacitance signatures can be made for all three particle sizes, and a range of Clausius-Mossotti factors, and initial velocities and heights.

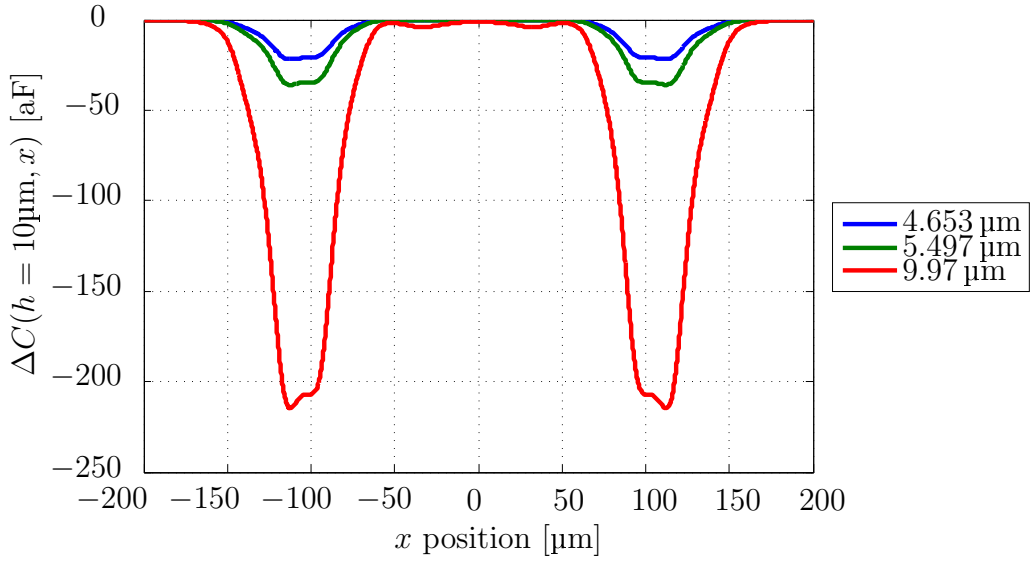

Figure 2.5: Theoretical capacitance change of a 4.653 µm, 5.497 µm, and 9.97 µm diameter PSS in DI water at heights of 10 µm.

2.3 Finite Element Dielectrophoretic Force Simulation

Similar to the method used in solving E_{RF}^2/Φ_{RF}^2, a simulation was performed to solve for the electric field due to Φ_{DEP}. Once the actuation field, $\overline{E}_{DEP}$, is found, the gradient of the squared electric field magnitude, ∇E_{DEP}^2, can then be calculated and used to find the total dielectrophoretic force exerted on a particle in the actuation zone, which is defined as the area over the electrodes where ∇E_{DEP}^2 is non-zero. Figure 2.6 shows the model used for the DEP force simulation. Simulation parameters are the same as shown in Table 2.1, with the exception of the electrode potential which is set to 4 V peak-to-peak, which is the potential used in experiments. Outside boundaries remain the Neumann (insulation) boundary condition, $\hat{a}_n \cdot \bar{J} = 0$, with the assumption that the field is near zero at the simulation edges. The solution to the complex form of Laplace's equation, $\nabla \cdot (\varepsilon \nabla V) = 0$, was found for a frequency of 1 MHz within the actuation zone. The electric field was solved only at 1 MHz since

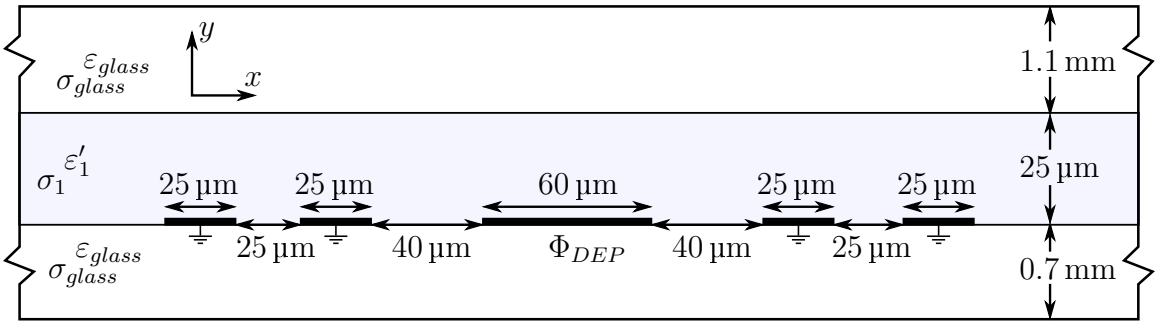

Figure 2.6: Model and parameters for COMSOL simulation of DEP electric field.

it remains relatively constant over the DEP frequency range of interest, 50 kHz to 10 MHz. The electric field does not change with frequency in this range due to the dominant role of conduction current, $\overline{J}_{cond} = \sigma_1 \overline{E}$, as compared with the displacement current, $\overline{J}_{disp} = j\omega\varepsilon'_1 \overline{E}$.

The resulting square of the RMS electric field magnitude, E^2_{DEP}, is shown in Figure 2.7. The general shape of the E^2_{DEP} plot is the same as that of the E^2_{RF}/Φ^2_{RF} plot in Section 2.2. The electric field magnitude becomes lower as the height above the electrode is increased. Local maxima occur over the electrode edges when close to the electrodes and move towards the centers of the electrode gaps as the height is increased.

The average DEP force on the particle, (1.41), depends on the gradient of the square of the the RMS electric field. Taking the gradient of the square of the electric field, the resulting x component is shown in Figure 2.8 and y component in Figure 2.9. The overall effect of the x component of the gradient, $\frac{\partial}{\partial x} E^2_{DEP} \hat{a}_x$, on the total integrated force exerted on the particle as it moves over the electrodes is small since it will act in both directions. The contribution of the x component will be to slow particle, then speed it up as it moves over areas of maximum E^2_{DEP} in the case of nDEP, or vice versa in the case of pDEP. The total net force is dominated by the y component of the gradient, $\frac{\partial}{\partial y} E^2_{DEP} \hat{a}_y$, as it remains the same sign anywhere within the actuation zone

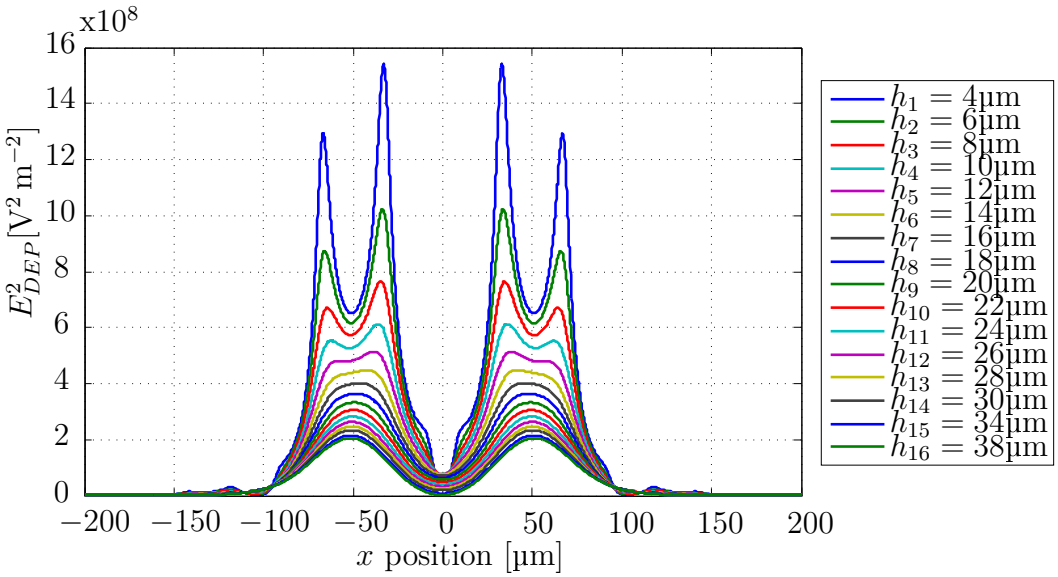

Figure 2.7: Square of the RMS electric field magnitude for the actuation field with $\sigma_1 = 100 \times 10^{-6}\,\frac{\mathrm{S}}{\mathrm{m}}$ and $\varepsilon_1 = 78\varepsilon_0$.

and only varies in magnitude. Generally, the ∇E^2_{DEP}, and therefore the force exerted on a particle with positive Re$\{K\}$, will be directed strongly towards the electrode edges when the particle is at a low elevation, and as the elevation is increased the force will become weaker and will be directed toward the gap between the electrodes.

2.4 Laminar Fluid Flow and Additional Forces

In general, particles flowing in the microfluidic channel will be subject to more forces than just dielectrophoretic forces. These forces will need to be accounted for in order to create a simulation of the expected particle trajectories and accurately interpret experimental data. The particle, will in addition to $\overline{F}_{DEP}$, will be subject

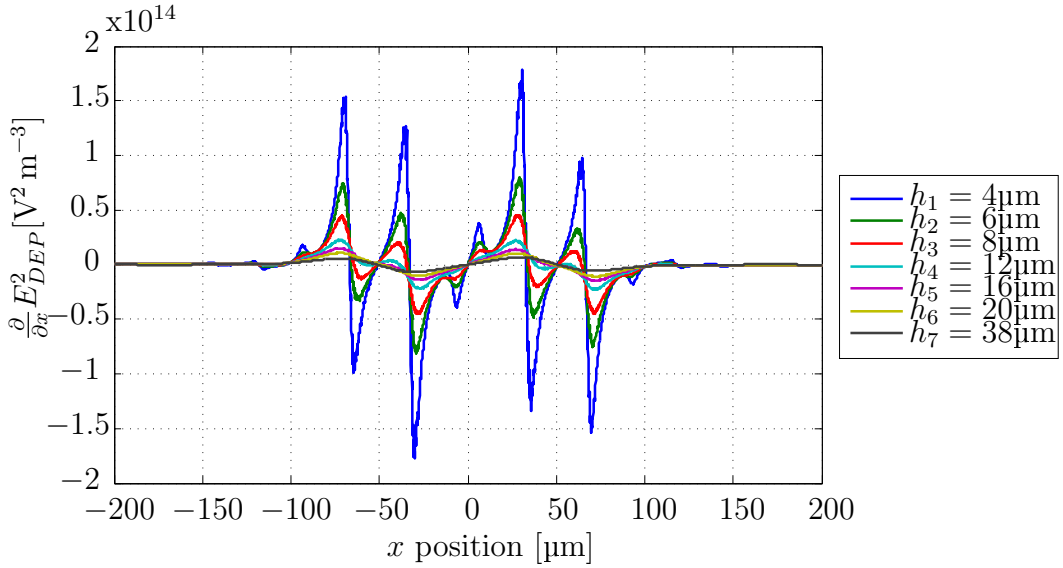

Figure 2.8: x component of ∇E_{DEP}^2 when electrode potential, Φ_{DEP}, is 4 V peak-to-peak.

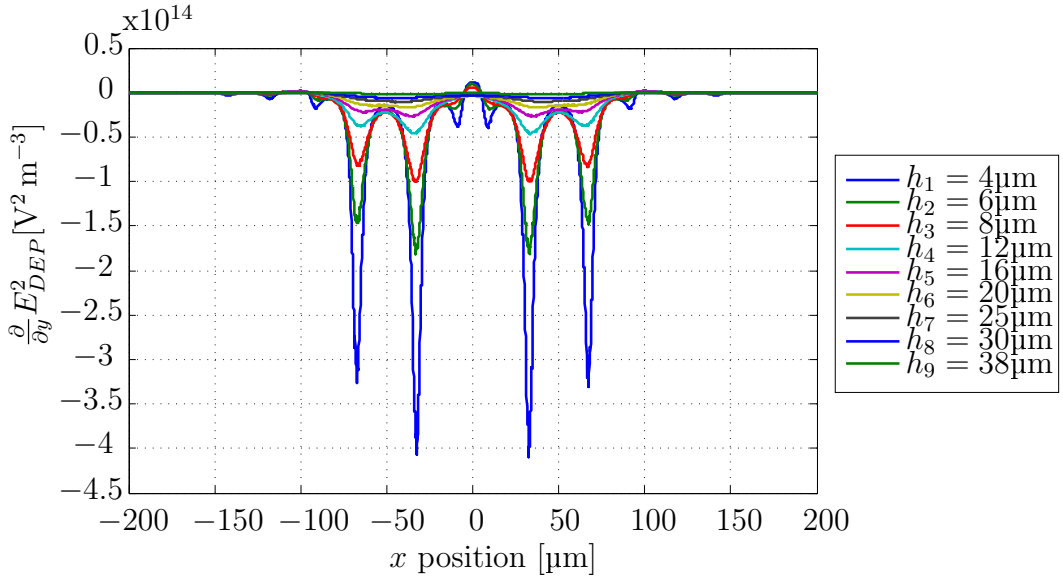

Figure 2.9: y component of ∇E_{DEP}^2 when electrode potential, Φ_{DEP}, is 4 V peak-to-peak.

to drag, gravity and buoyancy, and a hydrodynamic lift force:

$$\overline{F}_{total} = \left\langle \overline{F}_{DEP} \right\rangle + \overline{F}_{grav} + \overline{F}_{buoy} + \overline{F}_{drag} + \overline{F}_{lift} \tag{2.19}$$

A visual representation of the forces acting on a particle flowing in the channel are shown in Figure 2.10. The gravity and buoyancy forces being [12]

$$\overline{F}_{grav} + \overline{F}_{buoy} = \frac{4\pi}{3} a^3 g(\rho_m - \rho_p)\hat{a}_y \tag{2.20}$$

where g is the gravitational acceleration, $g = 9.81\,\mathrm{m\,s^{-1}}$, ρ_m is the density of the medium ($1000\,\mathrm{kg\,m^{-3}}$ for DI water), ρ_p is the particle density, ($1050\,\mathrm{kg\,m^{-3}}$ for polystyrene), and a is the particle radius. The Stokes' drag force is given by [12]

$$\overline{F}_{drag} = 6\pi a\eta(\bar{v}_m - \bar{v}_p) \tag{2.21}$$

where η is the medium viscosity, with $\eta = 1 \times 10^{-3}\,\mathrm{Pa\,s}$ for DI water, and $\bar{v}_m$ and $\bar{v}_p$ are the medium and particle velocity, respectively.

Finally, determining the fluid velocity flow profile within the microfluidic channel is necessary to find the expected lift and drag forces. The Reynolds number in a microfluidic channel is typically low (Re$<<1$), meaning that the flow can be described as laminar, as opposed to turbulent [20, 21]. Laminar flow means that the velocity profile will be parabolic, with the fluid velocity being zero at the walls of the channel and maximum at the center of the channel. The velocity profile will take the form [12]

$$v_m = 6\left\langle v \right\rangle (h/H)(1 - h/H) \tag{2.22}$$

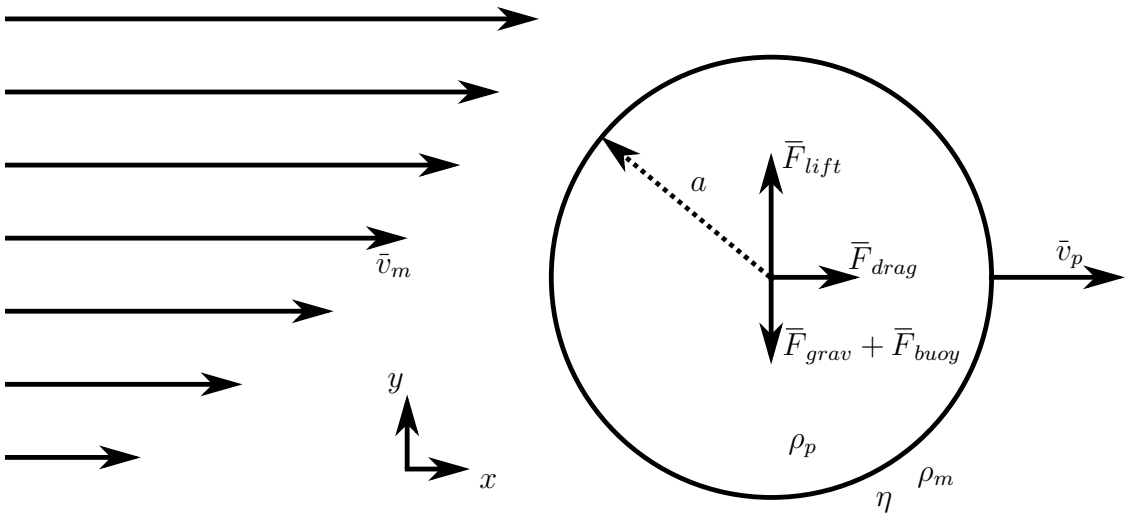

Figure 2.10: Summary of forces acting on a particle in motion in the microfluidic channel.

where v_m is the fluid velocity for a given height above the electrodes, h, $\langle v \rangle$ is the average velocity of the fluid flow and H is the total height of the channel, in this case 40 µm.

Since the fluid velocity varies across the channel, if the particle is anywhere but the center of the channel, either side of the particle will be at a point in the channel with a different velocity. Due to this difference in velocity the particle will experience a shear force that will rotate and push it towards the center for the channel, otherwise known as a hydrodynamic lift force. The hydrodynamic lift force when the particle is in the lower half of the channel is given as:

$$\overline{F}_{lift} = \begin{cases} C\frac{6\eta a^3 \langle v \rangle}{H(h-a)}\hat{a}_y, & a \leq h \leq H/2 \\ -C\frac{6\eta a^3 \langle v \rangle}{H(h-a)}\hat{a}_y, & H/2 \leq h \leq H - a \end{cases} \tag{2.23}$$

where a is the particle radius, η is the fluid viscosity, and C is the lift force constant which varies depending on the particle and system parameters [22]. A method is used in [12] and [1] to empirically determine the lift force constant from experimental data.

In [1], a set of interdigitated electrodes are used to measure capacitance changes due to a population of $a = 2.75\,\mu\text{m}$ PSS. The alternative electrode design allowed for a height estimate of each passing particle. By estimating the height and velocity of passing polystyrene spheres a best fit was done and it was found that $C = 0.106$. Though the above hydrodynamic lift equation typically overestimates the lift force compared to experimental data, it will be used as a best guess in simulation and to estimate the equilibrium height of particles.

Balancing the $\hat{a}_y$ components of the above forces for a given particle size and medium velocity results in the expected equilibrium height of the particle. The expression for the equilibrium particle height, h_{eq}, assuming the particle settles in the lower half of the channel takes the form:

$$h_{eq} = a + \frac{9C\eta \langle v \rangle}{2\pi g H(\rho_p - \rho_m)} \tag{2.24}$$

Calculating the equilibrium particle height for a range of fluid velocities results in a series of equilibrium heights. Next, for each of the fluid velocities and equilibrium heights an associated particle velocity can be found from the fluid velocity at that height in the parabolic flow. Figure 2.11 shows the equilibrium heights for each particle velocity of a $5.5\,\mu\text{m}$ diameter PSS in DI water.

By using the above forces along with the DEP force, the trajectories of particles with a range of sizes, initial heights, and initial velocities can be calculated. The following section will outline the calculation of the particle trajectories and expected capacitance signatures.

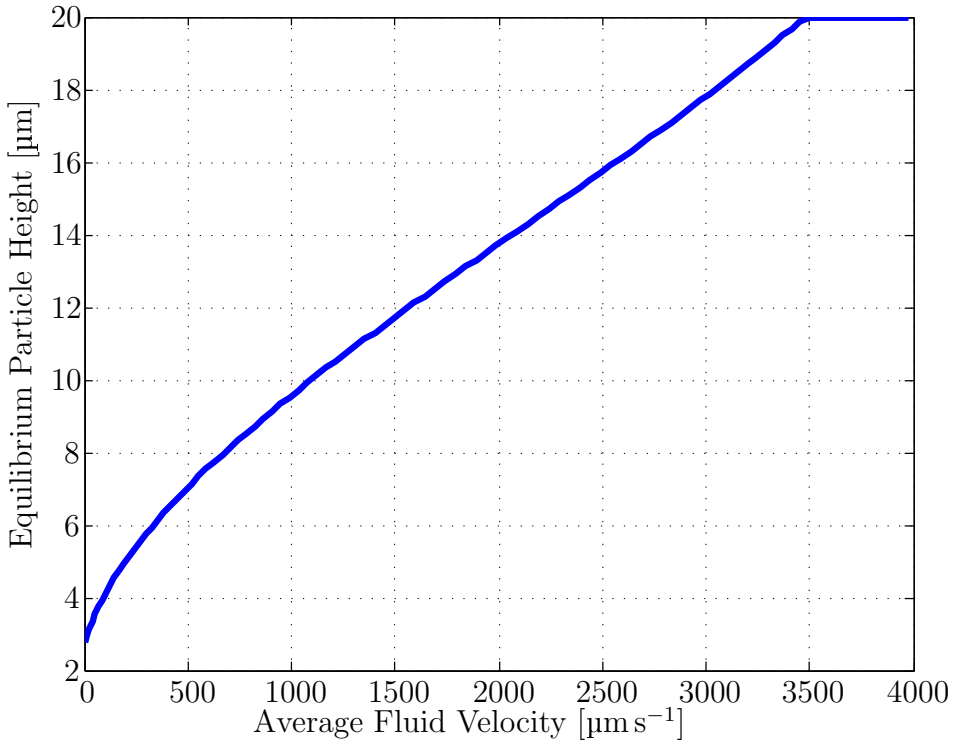

Figure 2.11: Equilibrium height for a 5.5 µm diameter PSS in DI water at a range of velocities.

Table 2.2: Parameters for PSS Trajectory Calculation.

Param	Value	Param	Value
a	$2.75\,\mu\text{m}$	ε_0	$8.854 \times 10^{-12}\,\text{F m}^{-1}$
ε_1	$78\varepsilon_0$ [11]	ε_2	$2.5\varepsilon_0$
Φ_{DEP}	$4\,\text{V}$ peak-to-peak	f_{dep}	$1\,\text{MHz}$
H	$40\,\mu\text{m}$	σ_1	$100 \times 10^{-6}\,\text{S m}^{-1}$
$\sigma_{2,bulk}$	$1 \times 10^{-16}\,\text{S m}^{-1}$	K_s	$2.56 \times 10^{-9}\,\text{S}$ [11]
ε_{glass}	$4.8\varepsilon_0$ [12]	σ_{glass}	~ 0 [12]
η	$1 \times 10^{-3}\,\text{Pa s}$	$\langle v \rangle$	$1500\,\mu\text{m s}^{-1}$
ρ_m	$998\,\text{kg m}^{-3}$	ρ_p	$1050\,\text{kg m}^{-3}$
C	0.106 [1]	g	$9.81\,\text{m s}^{-1}$

2.5 Simulated Particle Trajectories and Capacitance Signatures

Using the solved DEP electric field and the forces defined in Section 2.4, particle trajectories can be calculated for multiple initial elevations and particle sizes in order to find a general trend for the behavior of particles passing over an electrode array. Multiple initial elevations are used due to the uncertainty in the equilibrium height calculation.

Particle trajectories are calculated with COMSOL Multiphysics post-processing mode after the sensing and actuation fields have been calculated. Figure 2.12 shows the trajectories of $5.5\,\mu\text{m}$ diameter PSS subject to a $1\,\text{MHz}$, $4\,\text{V}$ peak-to-peak DEP voltage. The $5.5\,\mu\text{m}$ diameter PSS are released at a range of elevations and the trajectories are traced as they move over the sensing and actuation zones. Parameters are chosen to be the same as in the previous sections and are outlined in Table 2.2. As expected, since $\text{Re}\{K\} = -0.4073 < 0$ at $1\,\text{MHz}$, the particles are pushed away from the electrodes as they pass. Since the electric field gradient as well as the lift force is stronger near the bottom of the channel, the particles closest to the electrodes experience a much stronger force and experience a greater change in elevation.

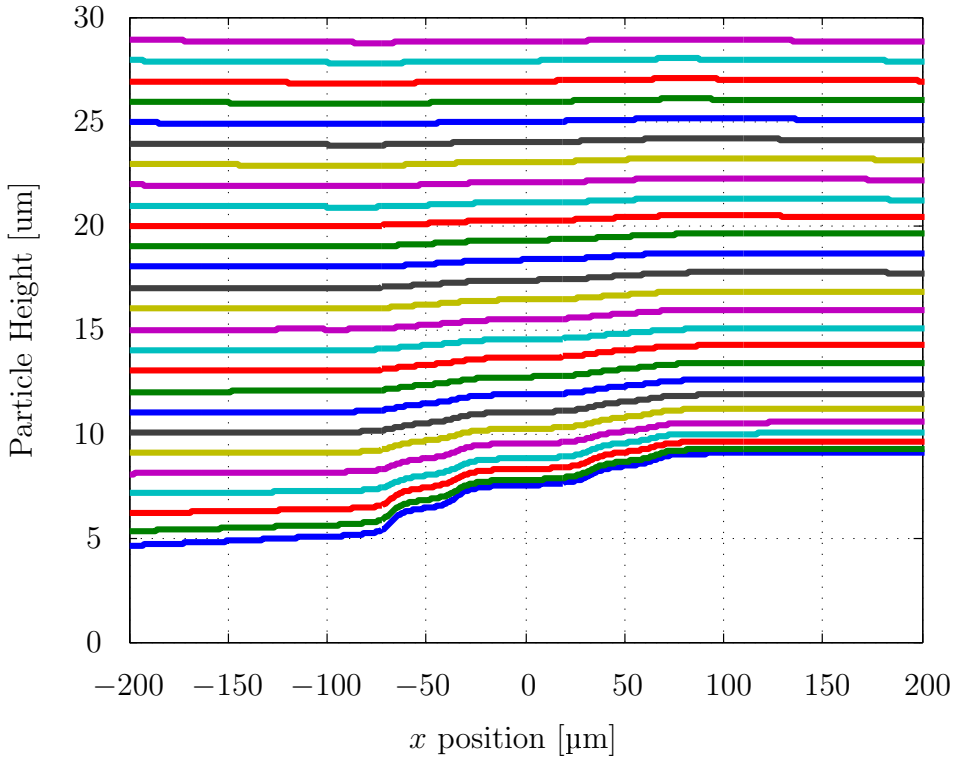

Figure 2.12: Trajectory for a 5.5 µm PSS at a range of initial elevations. The particle elevation, h, is referenced from the bottom of the channel to the center of the particle.

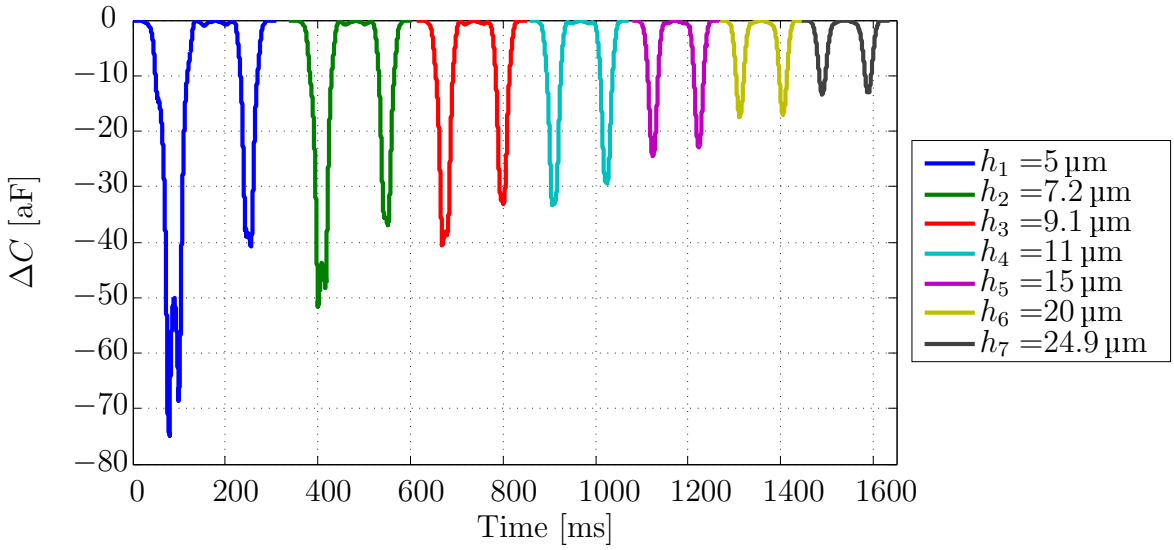

Figure 2.13: Simulated capacitance signatures for a 5.5 µm diameter PSS at a range of initial elevations.

From these particle trajectories the expected capacitance signatures can be found by plotting E_{RF}^2 along the particle path and scaling by $4\pi a^3 \varepsilon_1' K_\infty / \Phi_{RF}^2$. Figure 2.13 shows the capacitance signatures for a range of initial particle heights. As the initial particle elevation is increased the fluid velocity around the particle is increase, making the particle crossing time lower and the width of the capacitance signature shorter. As the initial height is increased E_{RF}^2 and ∇E_{DEP}^2 both decrease meaning the total signal magnitude is smaller due to lower sensing field magnitude and the relative change in magnitude is smaller since the DEP field gradient is lower. This will be explored further in Chapter 5 when experimental data is analyzed and more particle trajectories are used to find the Clausius-Mossotti factor of experimental results.

The following chapter will discuss the experimental apparatus used to collect the capacitance signals. This will include the discussion of the fabrication of the microfluidic chip used for experiments and an analysis of the microwave interferometer and resonator used to measure the electrode capacitance.

Chapter 3

Experimental Setup: Microwave Interferometer and Microfluidic Chip

To measure the dielectrophoretic force on a polystyrene sphere, a system was required to both deliver the particles to the actuation zone and measure the change in electrode capacitance, ΔC, and change in particle elevation cause by the force. To accomplish this a microfluidic chip was designed and fabricated to deliver particles to the actuation zone, and a microwave interferometer in combination with a couple-line resonator was used to measure the sensing electrode capacitance changes. This chapter will outline the steps taken to the final design of the microfluidic chip and microwave interferometer.

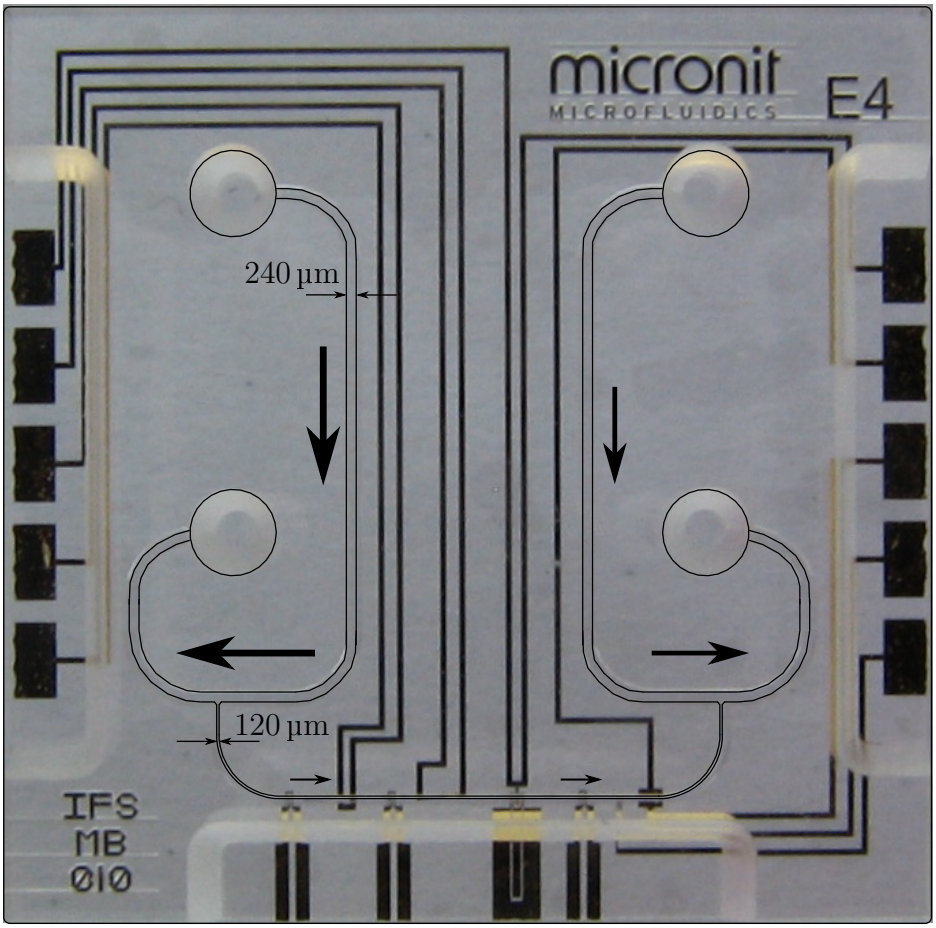

Figure 3.1: IFSMB010 microfluidic chip photograph, with channels, dimensions, and flow pattern overlaid.

3.1 Microfluidic Chip Fabrication

Measuring DEP forces and the Clausius-Mossotti factor of polystyrene spheres, along with other particles, requires the ability to selectively flow particles over the electrode array while accurately controlling the speed of the particles, within a threshold, and controlling the density of particles withing the flow, as to eliminate particle-particle interactions and accurately measure single particles. An H-channel design was used, shown in Figure 3.1, where the fluid velocity in the cross channel is determined by the differential pressure between the two larger side channels.

Microfluidic channels are etched into the bottom of the top, 1.1 mm thick, borosilicate glass layer. The total width of the side and cross channels are 240 µm and 120 µm, respectively, as measured at the bottom of the channel. Having the smaller width cross channel allows for fine control of flow velocity by changing the differential pressure between the side channels. By changing the total flow speed of the side channels, allows for small changes in particle density within the cross channel. Channel heights are 40 µm. The channels have quarter circles on the top corners due to the isotropic etch used in the Sensonit manufacturing process [16], making the width of the channel at the top 160 µm and 40 µm. Microelectrodes, with the same dimensions as simulations in Chapter 2, were countersunk into the of the bottom, 0.7 mm thick, glass layer and deposited as gold with a thickness of 200 nm.

Flow control is provided by a gravity fed mechanism, shown in Figure 3.2, where the pressure differential is provided by the difference in heights between two vials, the higher containing the DI water and polystyrene spheres and the lower just DI water. Solenoids, located on the two output ports, are normally clamping the output ports on each side. Purging of the device, to eliminate settling, is accomplished by having both vials pressurized at 7 psi. To purge, one or both of the solenoids are released and the water is allowed to flow straight through the system.

3.2 Microwave Interferometer and Resonator

This section will discuss the operation of the microwave resonator and interferometer, and provide a detailed circuit equivalent of the resonator and channel. It will also determine the total system sensitivity and total system noise.

Since the capacitance changes that are to be measured are on the order of tens of attofarads, a system was needed to accurately measure capacitances with a sub-

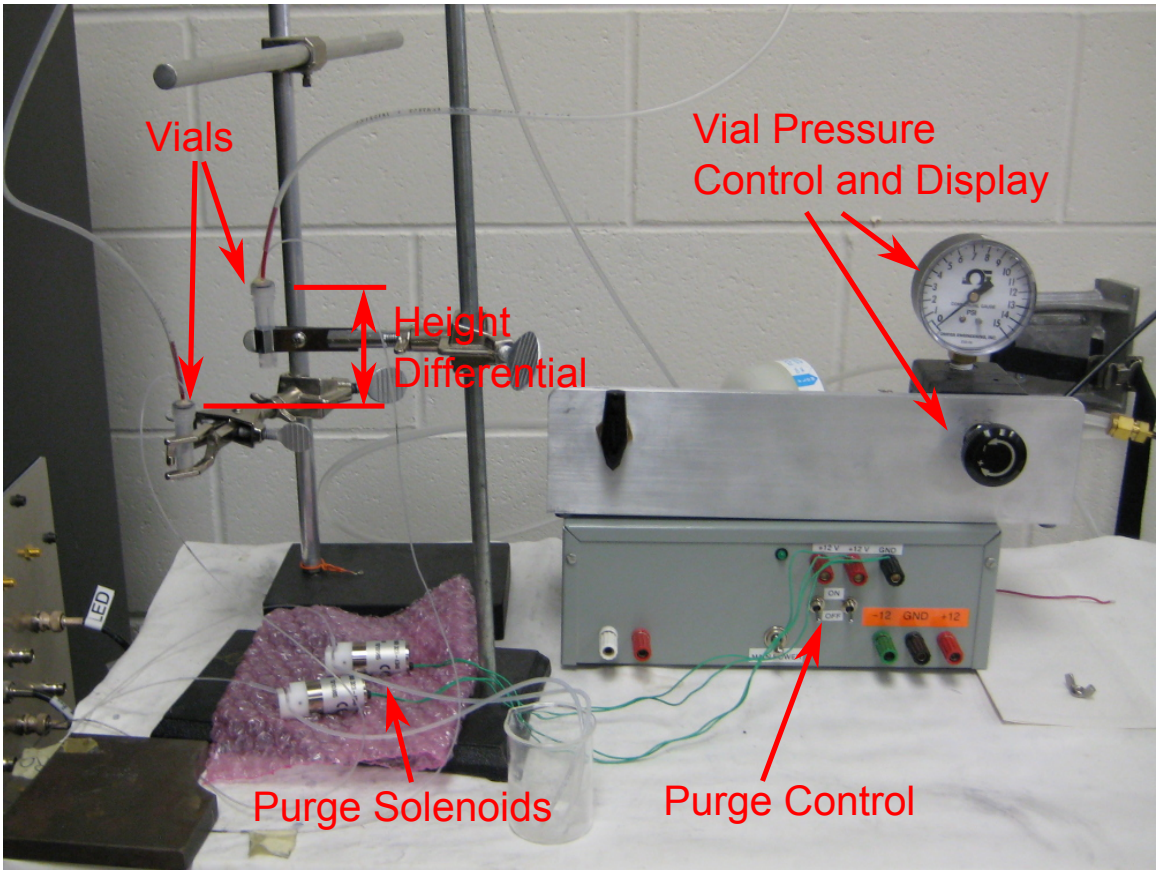

Figure 3.2: Gravity controlled flow is accomplished by placing the vials for each side channel at different heights, with the flow through the cross channel being controlled by the resulting pressure differential.

attofarad resolution. The solution was a microwave interferometer in combination with a quarter-wave-coupled-line resonator, similar to the systems found in [23] and [12, 18, 1, 24, 20]. In the system used for our experiments a slightly different resonator was used. As shown in Figure 3.3, a coupled-line resonator was used with the sensing electrodes connected to one of the traces so that the varying electrode capacitance will change the electrical length of the resonator and therefore change its resonant frequency. The microwave interferometer used to measure the electrode capacitance operates by splitting a 1-2 GHz range signal into two paths, a reference path and a resonator path, and measuring the change in phase difference between them caused

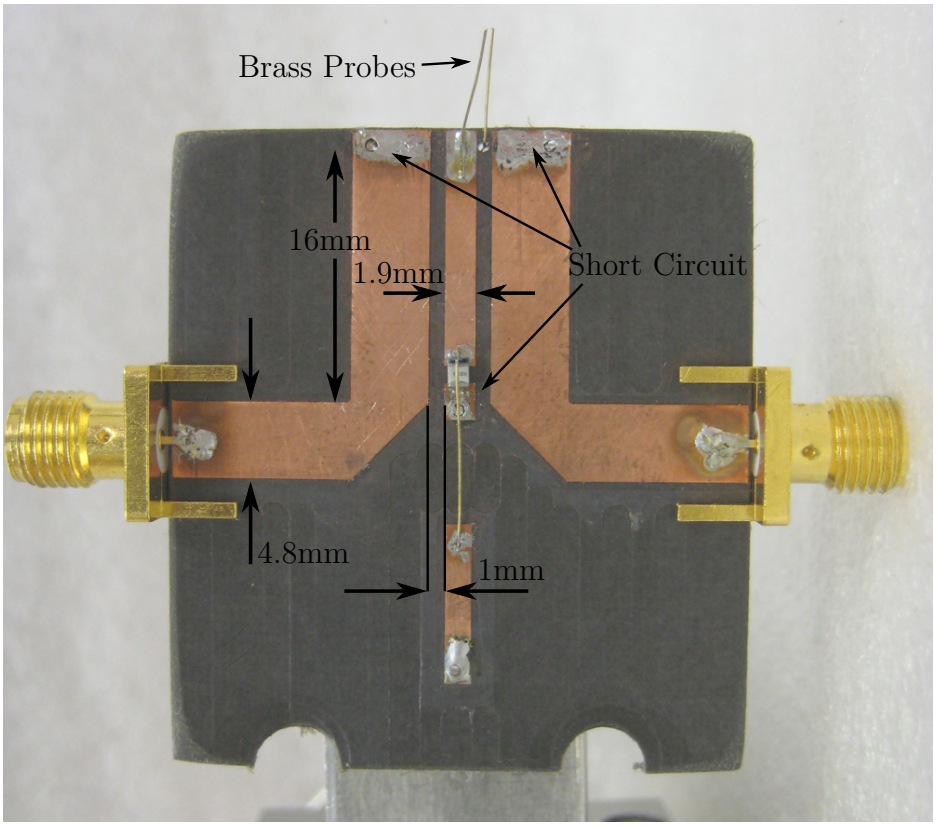

Figure 3.3: Quarter-wave-coupled-line resonator photograph with dimensions.

by the change in the sensing electrode capacitance. This section will describe the operation of the resonator and interferometer and outline the approach used in their design.

3.2.1 Quarter-Wave-Coupled-Line Resonator

To amplify the measured capacitance changes due to a particle passing over the electrodes and improve the signal-to-noise-ratio of the entire system, a quarter-wave coupled-line resonator, shown in Figure 3.3, was fabricated. The resonator was milled into copper on a copper clad low loss dielectric substrate, Rogers Duroid 5880 ($\varepsilon_r = 2.2\varepsilon_0$, $\tan\delta \approx 0.0007$), and is used to create a steep phase response at and around the resonance frequency. Figure 3.4 shows the $|S_{21}|$ thru response of the resonator, found

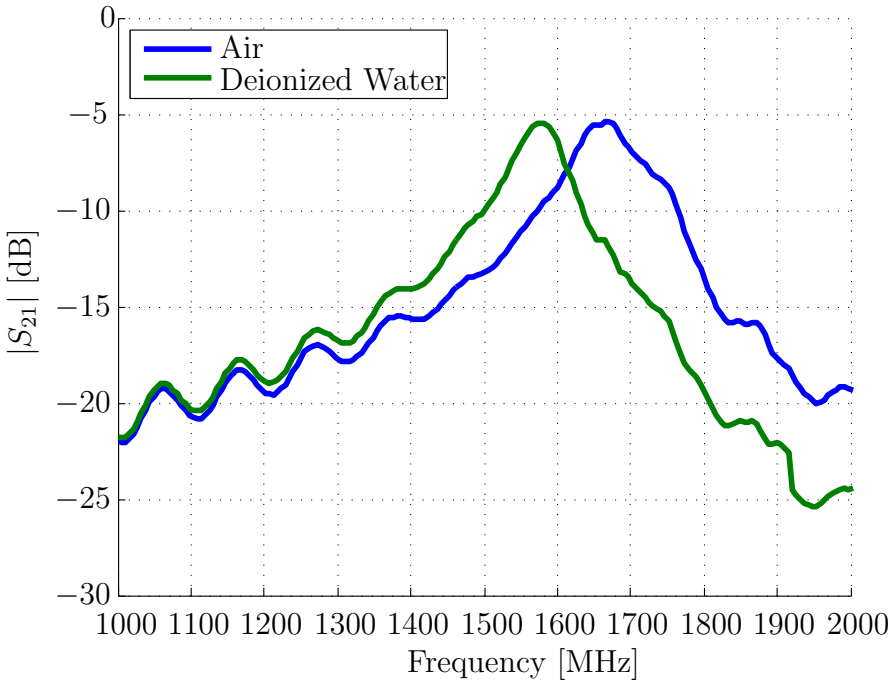

Figure 3.4: Quarter-wave-coupled-line resonator $|S_{21}|$ response with sensing electrodes attached. A 90 MHz shift is observed between the channel being filled with air (blue) and DI water (green).

using an Anritsu MS2036A vector network analyzer (VNA). From the figure it can be seen that the resonant frequency changes from the channel being filled with air at 1.667 GHz to 1.577 GHz when it is filled with DI water. By design, the insertion loss, $|S_{21}|$, is kept fairly constant (~ -5 dB) with the change in medium as to not significantly reduce the sensitivity when higher conductivity mediums are used. The unwrapped phase response of the resonator is shown in Figure 3.5, with a phase sensitivity at resonance of 1.013°/MHz, when the channel is filled with DI water. Keeping the gaps between the coupled-lines small makes the resonator insertion loss reasonably small, and makes quality factor, $Q \sim 15$, fairly low to make the resonator more immune to changes in medium conductivity. Connection of the resonator to the sensing electrodes is done through a set of brass probes attached to the resonator and contact is made by use of a 3-axis positioner.

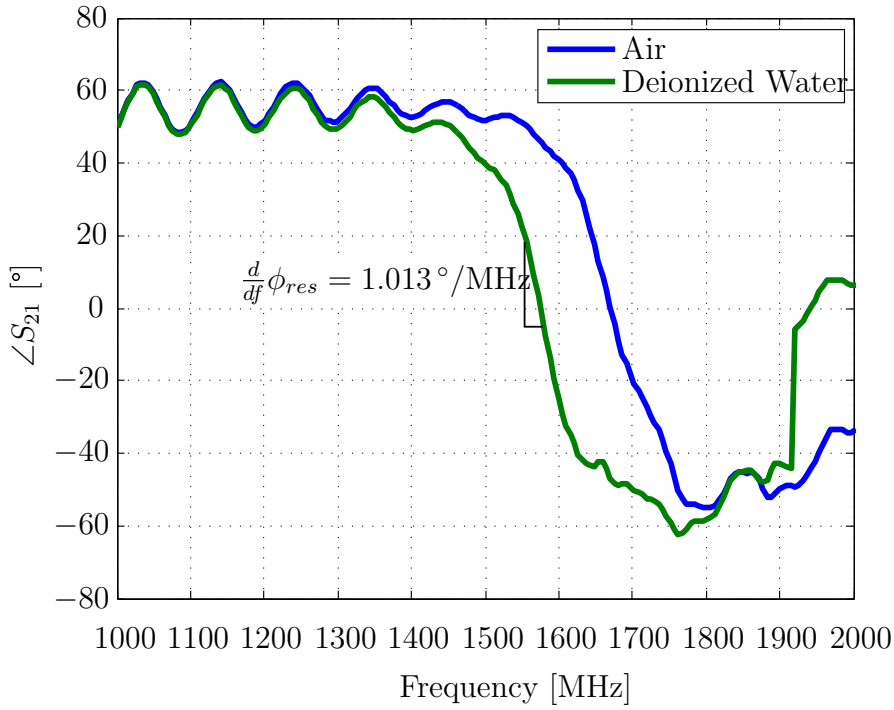

Figure 3.5: Quarter-wave-coupled-line resonator $\angle S_{21}$ response with sensing electrodes attached and channel filled with air (blue) and DI water (green).

An RF simulation was created, using Ansoft Designer, to verify the design and find the approximate voltage on the electrodes. Electrode voltage levels are required to be sufficiently low as to not have an effect on the particle trajectory by inducing a strong DEP force or other electromotive forces such as ac electro-osmisis and the electrothermal effect [12, 11]. The simulation was made to match the measured VNA data for resonator without the microfluidic chip attached, and with the chip attached and the channel filled with air then with DI water. Using these data, and the resonator dimensions and substrate, a circuit representation of the resonator and channel was found, shown in Figure 3.6. The resonator and brass probes are modeled by changing the 0.1 Ω to an open circuit, with everything to the right being the channel model. Removing the 180 fF capacitor and the 30 kΩ resistor on the far right will change the response from the channel filled with DI water to the air filled channel response.

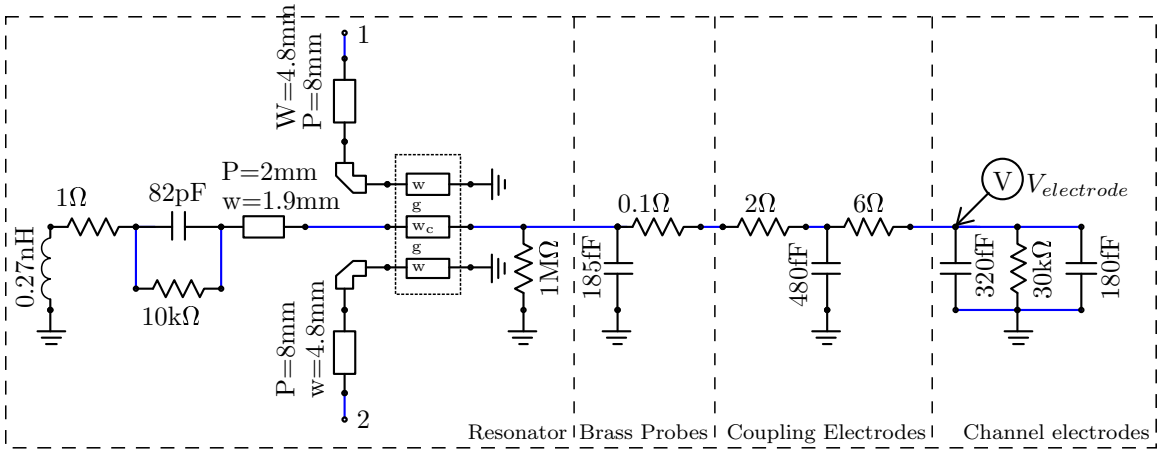

Figure 3.6: Ansoft Designer simulation model of the resonator and channel. Adding and removing the 180 fF capacitor and the 30 kΩ resistor models DI water and air in the channel, respectively.

Since the capacitance changes in experiments due to PSS or cells are on the order of a few hundred attofarads, the shifts in resonance will be no more than 100 kHz, meaning the insertion loss and electrode voltage magnitude will remain constant through the experiments. With 13 dBm on the RF source, -11.8 dBm is expected on port 1 of the resonator after including component and estimated line losses. Inputting -11.8 dBm on port one of the model, the voltage on the electrodes becomes $\sim$310mV peak when the source is operating close to resonance. This low voltage means the DEP force and other electromotive forces will be negligible in the sensing regions.

3.2.2 Microwave Interferometer

As a first-order approximation, the microwave interferometer measures small changes in the insertion phase of the quarter-wave short-circuit resonator described in Section 3.2.1, caused by small changes in electrode capacitance connected to its open-circuit terminal. The microwave interferometer operates by splitting a fixed frequency source into two paths, a reference path and a measurement path. The measurement path, containing the resonator, is mixed back with the reference path, whose low-

frequency output component is proportional to the capacitance change caused by passing particles. To reduce noise one branch of the interferometer is modulated at a lower frequency and a lock-in amplifier is used to extract the modulated signal.

A block diagram for the microwave interferometer is shown in Figure 3.7. For use in experiments the RF source, Agilent E8663B, is set to a power level of 13 dBm with the resonant frequency of the resonator when connected to fluid filled channel electrodes (∼1.58 GHz). From the RF source, the signal is first passed through a power splitter, Minicircuits ZAPDJ-2-S, into two paths, a reference path (ref) and a resonator path (res). From the power splitter the reference path is passed through a variable phase delay, ATM Microwave P1213, which is used to control the phase difference between the two paths at the resonant frequency. The reference path signal is input to the LO-port of the mixer, Minicircuits ZEM-4300MH+, a level 13 mixer.

From the splitter the resonator path is passed through a 6 dB attenuator for matching and power adjustment. Next it is amplitude modulated using an RF switch, ZASWA-2-50DR+. The switch is absorptive, with the second switch output terminated in a 50 Ω load. The modulating signal, at a frequency of 91 kHz, is provided by the lock in amplifier (LIA). A second attenuator is then used to lower the signal further by 10 dB, so the desired -10 dBm input to the resonator is achieved. The resonator path signal is then passed through the resonator, with an insertion loss of 5.45 dB and a phase response which is a function of the electrode capacitance, before being amplified by 30 dB by a low-noise amplifier, Minicircuits ZRL-2400LN. The amplifier output is passed through a 13 dB coupler, Minicircuits ZNDC-13-2G-S+. The coupler coupled port output is used, along with a peak detector, to find the resonant frequency when a VNA is unavailable. The thru-port signal of the coupler is input to the RF port of the mixer.

The reference path and the resonator path signals are then mixed. The lower

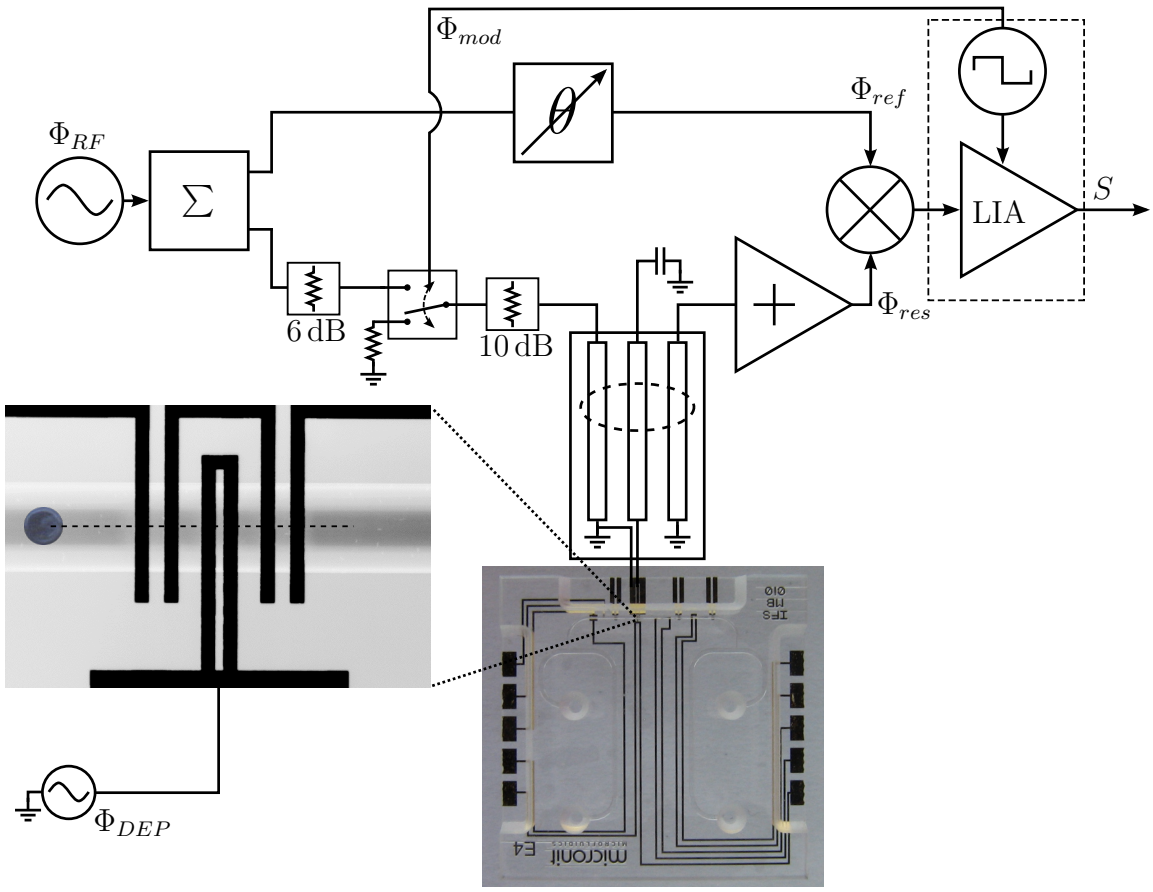

Figure 3.7: Block diagram for microwave interferometer.

frequency down-converted output is a 91 kHz signal with an amplitude proportional to the phase difference between the paths and the capacitance of the sensing electrodes. The higher frequency up-converted components are removed by the LIA input filter. The LIA down-converts the 91 kHz signal to a voltage dependent on the interferometer phase difference. Given as:

$$S = G|\Phi_{ref}|\cos(\omega t + \phi_{ref}) \times |\Phi_{res}|\cos(\omega t + \phi_{res}) \tag{3.1}$$

$$= \frac{G}{2}|\Phi_{ref}||\Phi_{res}|\left[\cos(\phi_{ref} - \phi_{res}) + \cos(2\omega t + \phi_{ref} + \phi_{res})\right]$$

$$\rightarrow \frac{G}{2}|\Phi_{ref}||\Phi_{res}|\cos(\phi_{ref} - \phi_{res}) \tag{3.2}$$

where G is the combined gain of the mixer and LIA, $|\Phi_{ref}|$ and $|\Phi_{res}|$ are the final reference and resonator path signal magnitudes, respectively, and ϕ_{ref} and ϕ_{res} are reference and resonator path signal phases, respectively. At the beginning of a set of experiments the resonant frequency is verified using the 13 dBm coupler and the variable phase delay in the reference path is adjusted so that $\phi_{ref} - \phi_{res}$ is an odd multiple $\pi/2$, so that any change in electrode capacitance will be measured from zero. The signal then becomes:

$$S = \frac{G}{2}|\Phi_{ref}||\Phi_{res}|\cos(\pi/2 - \Delta\phi_{res}) \tag{3.3}$$

$$= \frac{G}{2}|\Phi_{ref}||\Phi_{res}|\sin(\Delta\phi_{res}) \tag{3.4}$$

$$\approx \frac{G}{2}|\Phi_{ref}||\Phi_{res}|\Delta\phi_{res} \tag{3.5}$$

$$\approx \frac{G}{2}|\Phi_{ref}||\Phi_{res}|\frac{d\phi_{res}}{df}\frac{df}{dC}\Delta C \tag{3.6}$$

where $\frac{d\phi_{res}}{df}$ is the small signal change in phase of the resonator path per unit change in frequency, estimated in Section 3.2.1 at 1.013 °/MHz, $\frac{df}{dC}$ is the small signal change in resonant frequency cause by a per unit capacitance change, and ΔC is the change

in the electrode capacitance due to the particle.

A 3D simulation of the channel was made to calculate the electrode capacitance with both air and water filling the channel. An estimated capacitance change of 80 fF was calculated when the air was replaced with water. Since replacing the air filled channel with DI water resulted in a 90 MHz change in resonant frequency, $\frac{df}{dC}$ is estimated to be 1.125 MHz/fF. From the ZEM-4300MH+ datasheet [25] the estimated conversion loss for the mixer for an LO power level of 9 dBm is $\sim$7 dB ($\sim$0.2). The estimated power level for the resonator path at the input of the mixer including cable loss and power loss in the components is 7.9 dBm. The LIA sensitivity during the experiments was set to 500 µV meaning the total LIA gain is 10 V/500 µV=20000 V/V. Finally, unipolar switching AM modulation means that after modulation the fundamental, at $f_{RF} \pm 91$ kHz, is reduced by $2/\pi$. Making the final signal:

$$S \approx G_{tot}|\Phi_{res}|\frac{d\phi_{res}}{df}\frac{df}{dC}\Delta C \tag{3.7}$$

$$\approx \left[(0.2)(20000)\frac{2}{\pi}\right]\left[0.56\right]\left[1.013\frac{\pi}{180}\right]\left[1.125\times10^{-3}\right]\Delta C \tag{3.8}$$

$$\approx \left[0.028\,\mathrm{V\,aF^{-1}}\right]\Delta C \tag{3.9}$$

Making the estimated system sensitivity 36 aF V^{-1} (1/0.028) for a LIA gain of 20,000.

3.3 Experimental Sensitivity Estimate

Due to the various approximations in the above sensitivity estimation method, the overall system sensitivity was also found using experimentally collected capacitance signals. This section will describe the estimation of system sensitivity with use of experimentally collected data.

Experimental determination of the system sensitivity was accomplished by first

simulating the peak electrode capacitance changes versus average crossing speed for a PSS in the detection zone, for a given fluid velocity profile, and then applying the curve as a best-fit to experimentally collected capacitance signals. A block of data was chosen so that many particles crossed the detection zone within a short time, so as to limit effects due to changes in the fluid velocity. A seven minute block of signals were chosen shortly after a purge, when no DEP was applied, so that the particles were more dispersed over the height of the channel. A simulation was done to find the expected capacitance signatures that, when particles are dispersed through the channel, would have the same maximum particle velocity as those observed in the experiment. For this measurement a set of 5.5 µm PSS data were chosen that consisted of 180 PSS crossings. The maximum velocity was found to be roughly $4000\,\mu\mathrm{m\,s^{-1}}$ and a simulation was done to find the capacitance signatures of particles dispersed in a flow profile matching the top speed of the experimental data.

Figure 3.8 shows the curve resulting from the simulated data. In the figure, the peak capacitance change, ΔC, due to the particle moving over the first pair of sensing electrodes is plotted against the average crossing speed as estimated by the physical distance between centers of the sensing electrodes ($\sim$215 µm) divided by the time between the two capacitance peaks. The range of particle heights results in a range of average crossing speeds that match the fluid velocity profile across the channel. A fit, shown in red, was applied to the particles in the lower half of the channel. Next, the segment of experimental data, described above, was plotted and is shown in Figure 3.9. The figure shows, in blue circles, the amplitude of the first peak in the capacitance signals as plotted against the average particle crossing speed, calculated in the same way as in Figure 3.8. The simulated curve fit from Figure 3.8 was then scaled to fit the experimental plot for signal voltage versus average crossing speed, shown in red in Figure 3.9. The simulated peak capacitance change fit was scaled

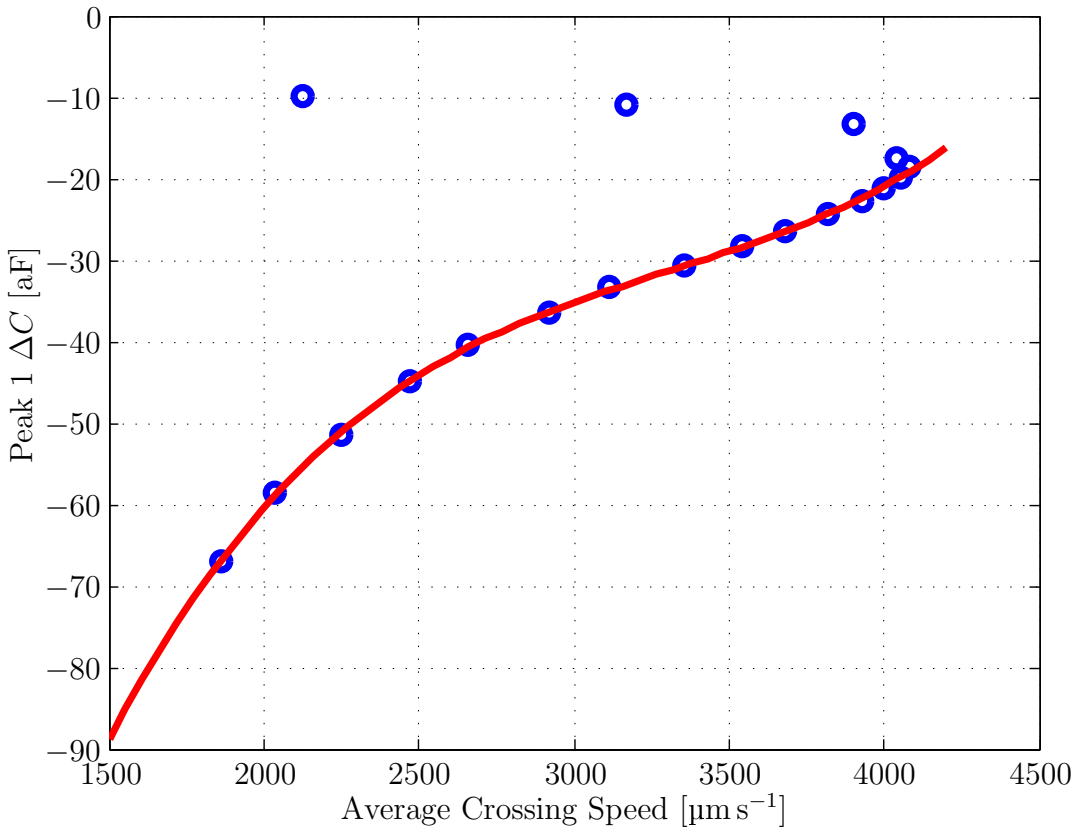

Figure 3.8: Simulated capacitance change of the first peak versus average crossing speed for 5.5 µm PSS in a laminar flow with $\langle v \rangle = 2667\,\mu\mathrm{m\,s^{-1}}$. Average crossing speed is calculated by dividing the physical distance between the centers of the sensing electrode pairs, 215 µm, by the time between the two peaks in the capacitance signature. A third order polynomial fit, shown in red, is done on the data points from the lower half of the channel.

by 1/45 to match the experimental data, making the resulting estimated system sensitivity $45\,\mathrm{aF\,V^{-1}}$ for that given experiment.

This same method was used to find the sensitivity of each of the experiments which will be described later in this thesis. Using the mean particle radii and an estimated average fluid velocity for the set of closely spaced particles, a simulation was done for each of the data sets. The results of the sensitivity estimates are detailed in Chapter 5.

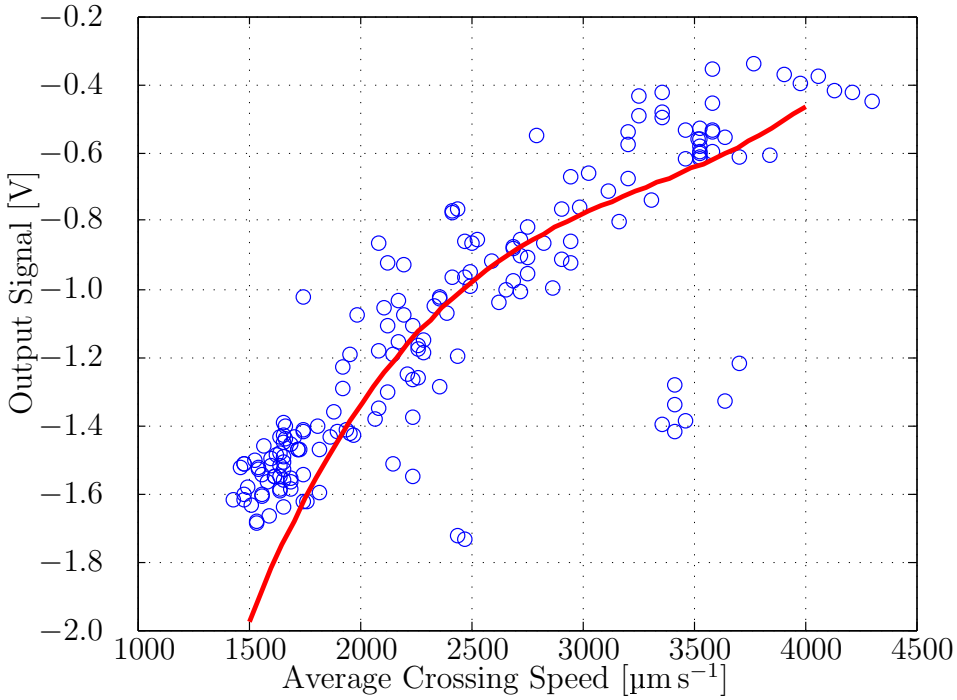

Figure 3.9: Experimental capacitance signal of the first peak versus average particle velocity is plotted for unactuated 5.5 µm. Third order polynomial fit from simulation is scaled by 1/45 V aF^{-1} to match the experimental results and shown in red.

3.4 System Output Noise Measurement

This section will be used to calculate the total output noise of the experimental apparatus. This will also determine the minimum detectable capacitance change.

An example of a 5.5 µm diameter PSS signal at an estimated height of 12 µm, shown in Figure 3.10, was chosen in order to show the signal noise compared to the capacitance signals due to passing particles. To measure the total output noise of the system, the block of capacitance signal, shown in red, was analyzed from the 5.5 µm PSS data set used in the sensitivity analysis above. The DC offset was removed from the original signal, using the same baseline fit technique discussed later in Section 4.2,

leaving a zero offset noise signal. The RMS noise voltage was found using:

$$S_{rms} = \sqrt{\frac{1}{n}\sum_{i=1}^{n} S_i^2} \tag{3.10}$$

where n is the total number of points in the signal section, and S_i are the sample values in the signal. From this, the RMS signal noise was found to be 9.5 mV. With the sensitivity estimate detailed in Section 3.3 (45 aF V^{-1}) applied to the noise voltage, a resulting RMS capacitance floor of 430 zF was found. All measurements in this thesis were taken with LIA settings, τ=1 ms, and a filter roll off of 12 dB/oct, meaning the equivalent noise bandwidth, according to the LIA manual [26], will be $1/8\tau$ =125 Hz. The total sensitivity, assuming only white noise, thus corresponds to 38.5 zF/$\sqrt{\text{Hz}}$.

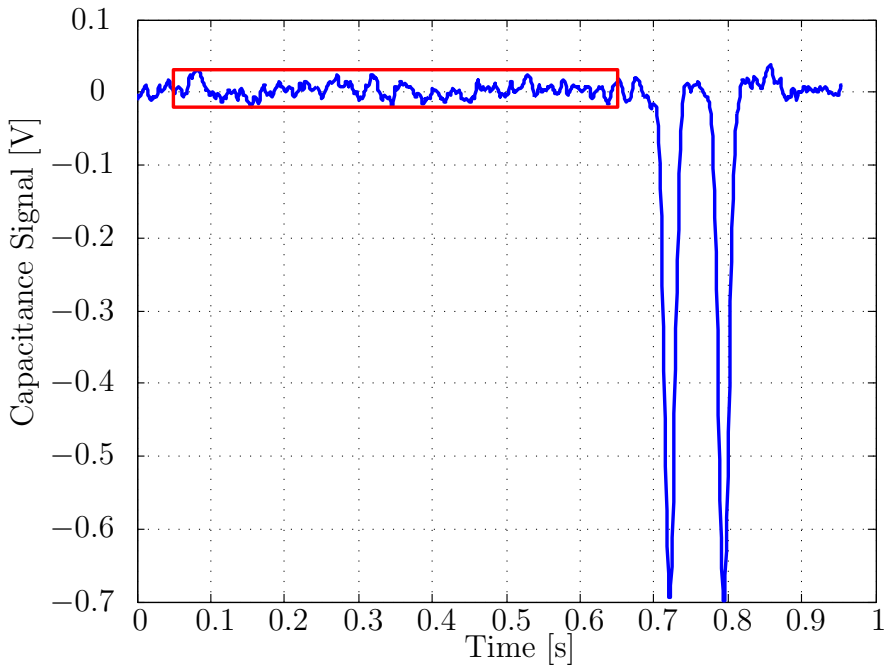

Figure 3.10: Section of capacitance signal from 5.5 µm diameter PSS at an estimate height of 12 µm with DC offset removed, shown in blue. Area shown in red used for noise measurement, with an RMS value of 9.5 mV.

The following chapter will discuss the data acquisition and post processing programs created for the collection and analysis of experimental data.

Chapter 4

Signal Processing

The experimental apparatus described in the previous chapters, a block diagram of which is shown in Figure 4.1, was designed to facilitate the measurement of the dielectric properties of various particles. This is accomplished by collecting the time domain signals that are proportional to the capacitance changes of a set of sensing electrodes, $\Delta C(t)$. These raw signals, an example of which is shown in Figure 4.2, can have shifts in the baseline as the system approaches equilibrium, multiple particles passing over the electrode array simultaneously, and sharp discontinuities cause by external disturbances. Once these undesired signals are removed, quantifiable information needs to be extracted from the signals. This thesis makes use of the time between peaks, and the peak amplitudes and widths for the pre-DEP and post-DEP events. These data are used to filter the data and measure the force on the particle with the final goal of determining the Clausius-Mossotti factor over a range of frequencies for each of the particle sizes.

Two programs were written to facilitate the rapid collection and analysis of capacitance signatures. The first is used to collect and label the capacitance signal output of the microwave interferometer. The second is used to analyze collected capacitance

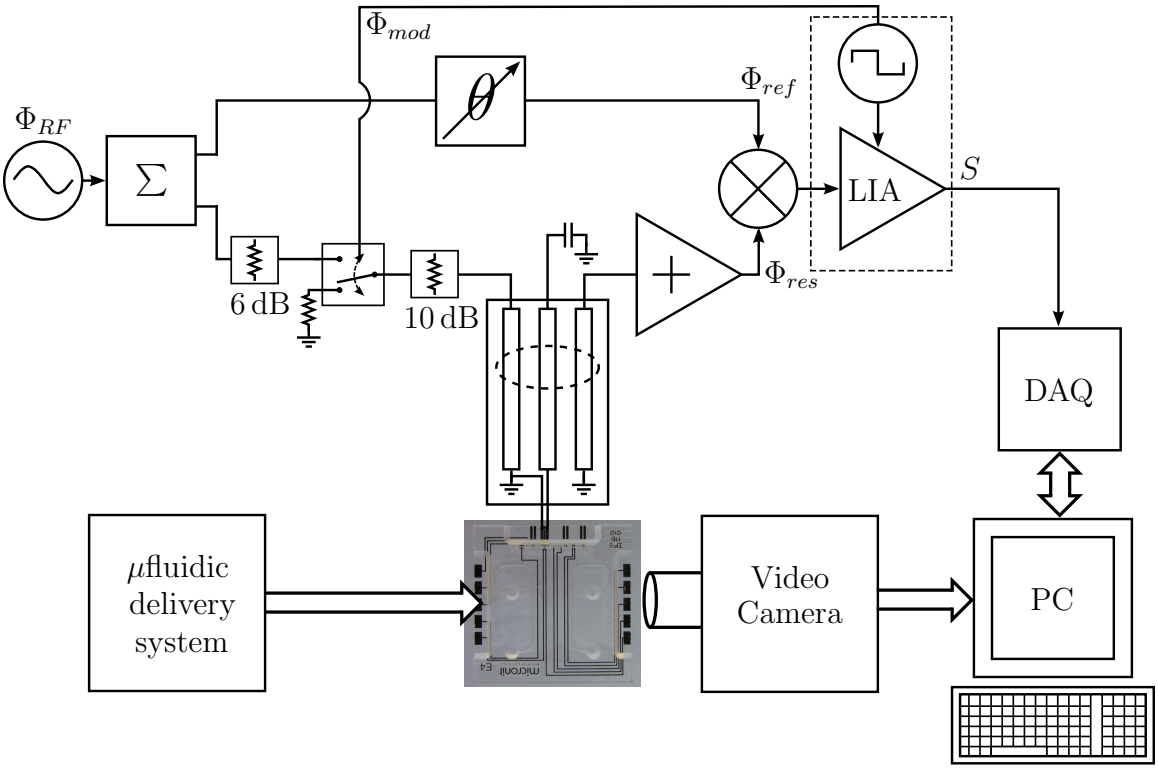

Figure 4.1: Block diagram showing entire experimental apparatus.

signals and to identify usable single cell or particle crossings, allowing for the significant reduction in the non-useful information. This chapter will explore the operation and use of these programs.

4.1 Data Collection and Labeling

Capacitance signals from the lock-in amplifier are collected using a PCI data acquisition (DAQ) board within the desktop computer that accompanies the impedance cytometry system. A program was written to collect sampled data from the DAQ board, mark it with a time stamp, break the data up into chunks for storage, label each of the data files with experimental parameters, and display real-time data during collection.

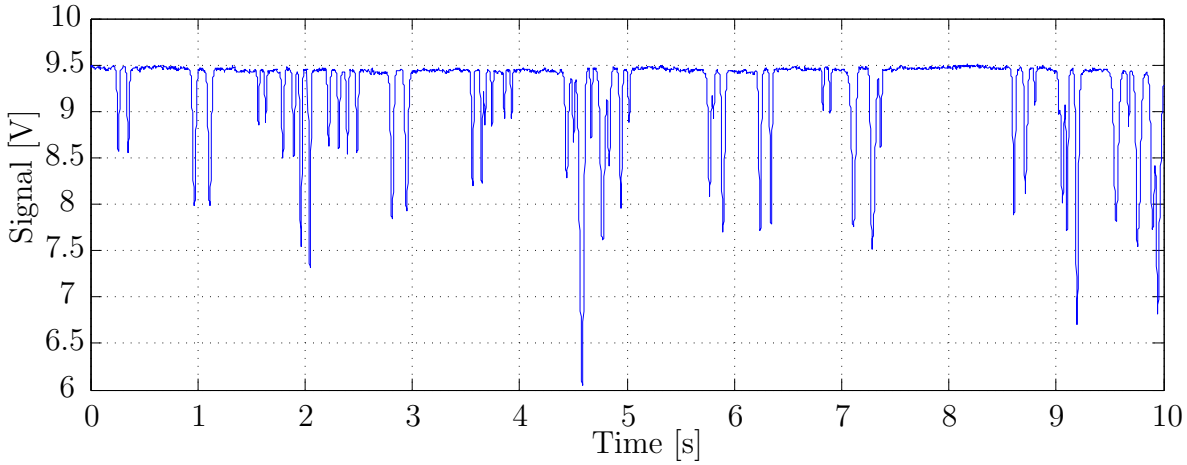

Figure 4.2: Ten second sample of raw 5.5 µm diameter PSS signals.

Figure 4.3 shows a screenshot of the graphical user interface (GUI) of the DAQ program at startup. Before each experiment the information in the middle of the screen is filled in to identify the parameters of the experiment. Next the directory in which the data will be saved is chosen using a folder browser dialog when the "Choose Directory" button is pressed. An option is available to record an auxiliary input on channel 1 of the DAQ, which can be used to record DEP signals or electroporation signals [27], in addition to the capacitance signal from the interferometer on channel 0. There is another option to process data in real time, allowing for real time baseline subtraction of signal offset and identification and saving of signal information such as peak times, peak voltages, and event times. The process by which this is done is the same as that discussed later in Section 4.2, but the baseline fit and peak search algorithms are applied to data after a delay of one to two seconds. This feature is not commonly used as it is CPU intensive and processing during purges and settling times can lead to an overload of data and slow program response.

Once the experiment information is filled in and any additional options are selected, the "Start DAQ" button is pressed, and the program sets up directories and files to store collected data, initializes the DAQ and disables a number of input op-

Figure 4.3: Data acquisition program GUI on launch.

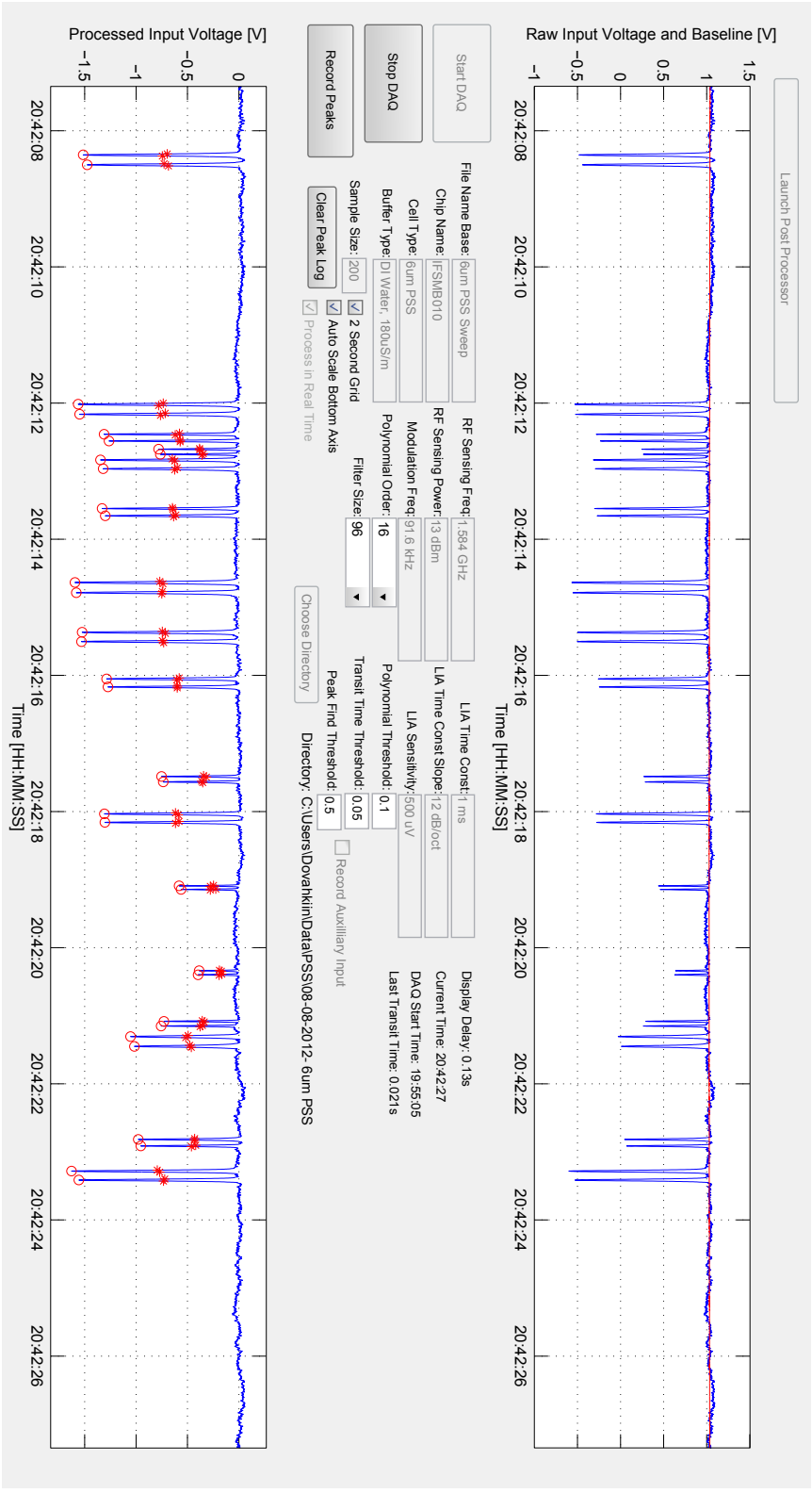

Figure 4.4: Data acquisition program GUI during capacitance signal sampling.

tions to ensure consistency in the data files. The program then starts the DAQ session on the DAQ board and starts collecting, displaying, and saving capacitance signals. A screenshot of the DAQ program GUI while collecting capacitance signals is shown in Figure 4.4. The real-time capacitance signal is displayed on the top axes in volts, with an auto-adjusting voltage extent to allow for viewing of smaller signals and a rolling window width of 20 s to allow for viewing of multiple events. Data is collected from the DAQ buffer in blocks specified in the GUI under "Sample Size" before the experiment begins. Collecting data with a larger sample size means the program will be able to process more data each time through the main loop and will not have any problems keeping up with the real time collection. A drawback of the larger sample size being that the plot updates in larger blocks making feedback delayed when changing experimental parameters such as flow speed and the DEP signal. With smaller sample sizes the plot updates smoothly, but under a heavy CPU load from other programs the DAQ program may need to collect multiple samples in a loop and could lead to loss of data if the heavy CPU load continues. As the program collects multiples of 30000 data points, the blocks of data are saved to comma-separated values (CSV) files, making each file 30 s when sampling rate is 1 kSample/s as is typical, keeping the data files relatively small for fast loading in MATLAB and Microsoft Excel. Table 4.1 shows an example of the top of a saved data file, showing the header format and format of the collected data.

When the experiment is over the "Stop DAQ" button is pressed, the program stops the DAQ session, saves the remaining data in the buffer to a new file, and re-enables the original buttons and text fields for another experiment. All the experimental parameters are also saved in a preferences file to be reloaded on the next program launch since most of the parameters remain the same over multiple experiments.

Table 4.1: Data file header and data points example.

Chip Name: IFSMB010		Cell Type: 6um PSS	Buffer Type: DI Water, 180uS/m
RF Sensing Freq: 1.584 GHz		RF Sensing Power: 13 dBm	Modulation Freq: 91.6 kHz
LIA Time Const: 1 ms		LIA T.C. Slope: 12 dB/oct	LIA Sensitivty: 500 uV
Start Time: 08-Aug-2012 19:55:05			Sample Rate: 1 kSamples/s
Time:	Raw Data:	Processed Data:	Peaks:
7:55:05.608 PM	-2.350957504		
7:55:05.609 PM	-2.353704128		
7:55:05.610 PM	-2.353704128		
7:55:05.611 PM	-2.350957504		
7:55:05.612 PM	-2.347600519		
7:55:05.613 PM	-2.350347143		
7:55:05.614 PM	-2.356145571		
7:55:05.615 PM	-2.355230030		

4.2 Post Processing and Analysis

Since irregularities are commonly observed in the capacitance signals, including purges of the channel, discontinuities due to changes in sensing frequency or changes in DEP voltage, or mechanical disturbances, a program was written to convert the high volume of time domain data accompanying each experiment into a more compact form. The time domain signals are broken down into peak amplitudes, times, and widths. The program adds an interface, shown in Figure 4.5, to allow for seamless viewing of full experiments and the ability to identify single crossings of particles.

To start, the location of the experimental data to be processed is identified by clicking the "Choose Directory" button and navigating the directory dialog to the proper data location. The folder is then scanned to find the files with the correct format for loading and the drop down menu labeled "Available Files" is populated with the data files in the experiment. The first file in the data set, along with the adjacent file, is then loaded into memory and displayed. The bottom axis is used to display the processed data. The DC offset is removed and the signal peaks are identified. The raw signal voltage is displayed on the top axis to give a comparison

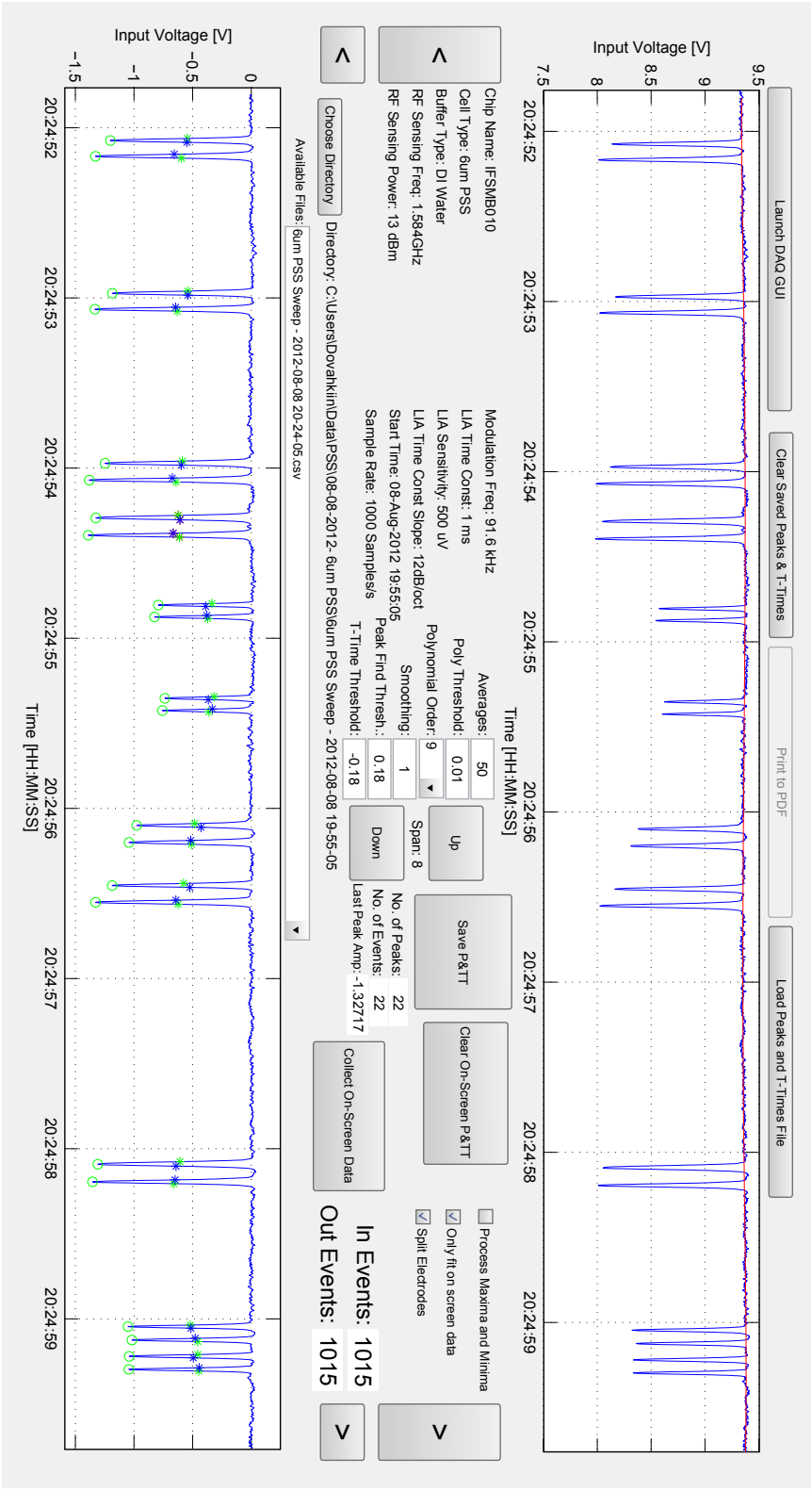

Figure 4.5: Post processing program.

in case processing causes an distortion in the signals.

Processing of the data first includes a base-line fit to subtract out an offset or a slow drift in the capacitance signal. This base-line fit is found by subtracting a moving average filtered signal from the raw data and removing the points that exceed a threshold, typically cause by a passing particle, then applying a polynomial fit to the remaining raw data points. Subtracting the filter signal from the raw is similar to finding the time derivative of the signal and removing points with too high of a slope. The data points to which the fit is applied then satisfy:

$$\left| S[n] - \frac{1}{N} \sum_{i=0}^{N} S[n-i] \right| < d_{max} \tag{4.1}$$

where $S[n]$ is the nth signal sample in the data to be fit, N is the filter size, specified in the GUI in the "Averages" text field, and d_{max} is the threshold for the maximum change from average, specified in the "Poly Threshold" text field in the GUI. A polynomial fit of an order specified in the "Polynomial Order" drop-down menu, is then applied to the data points that are under the threshold. The values of the polynomial are then calculated for the times of each data point and the raw data is plotted along with the calculated polynomial on the top axis. The polynomial fitted base-line is subtracted from the raw data, moving the base-line to zero. An optional moving average filter, with a filter size specified by the "Smoothing" text field, is then applied to the base-line subtracted data to reduce noise in the signal and the filtered signal is plotted on the bottom axes of the GUI.

After any offset is removed from the capacitance signal and the optional smoothing filter is applied, local minima are found, identifying a particle passing over the electrodes, using the peak detection function, peakdet [28], configured to find local minima. The peak threshold level for the function is set using the "Peak Find Thresh"

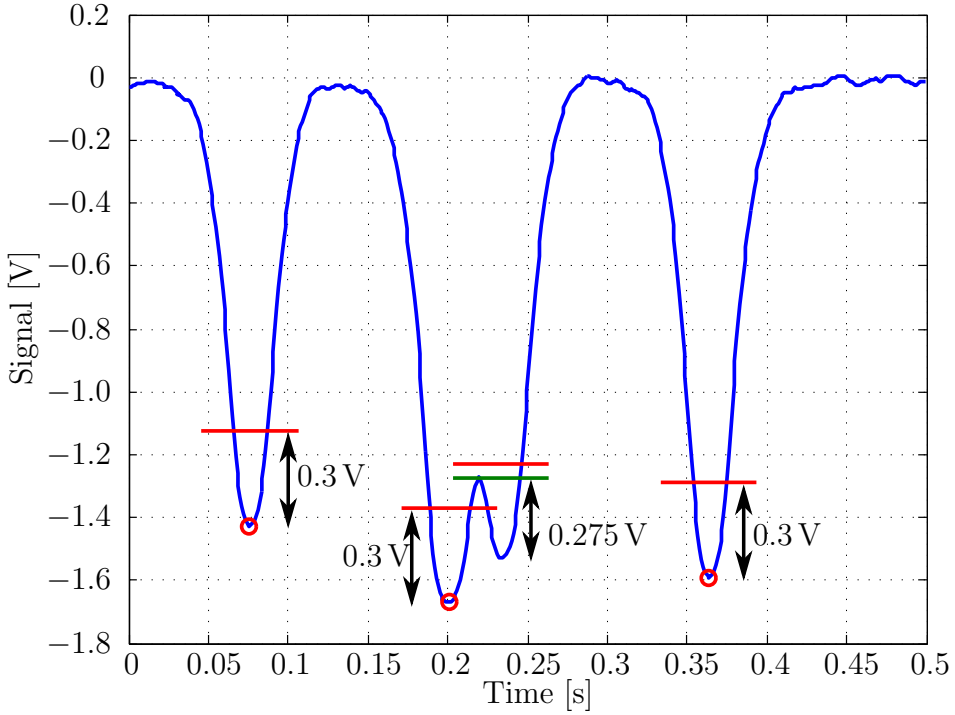

Figure 4.6: Example of the peakdet algorithm run using a threshold of 0.3 V.

text field. The zero derivative with thresholding algorithm in the peakdet function will only accept local minima with points above the threshold on either side of the minima, an example of the results when the threshold is set to 0.3 V is shown in Figure 4.6. Depending on the electrodes used in the experiment, selected in the GUI using the "Split Electrodes" check box, the signals will have a different form and need to be labeled in different ways to simplify plotting of processed data.

Two gap electrode sets, such as those shown in Figure 4.7 with an inset capacitance signal example, have multiple peaks and only deviate from the base-line once per crossing, unlike the signals from the split electrode configuration discussed in earlier chapters. For the two gap electrodes, crossing events are bookended by in and out flags which are found by setting a threshold level, "T-Time Threshold" text field in the GUI, and finding the points at which the signal deviates from the base-line by more than the threshold. These in an out flags group the minima, and maxima if the

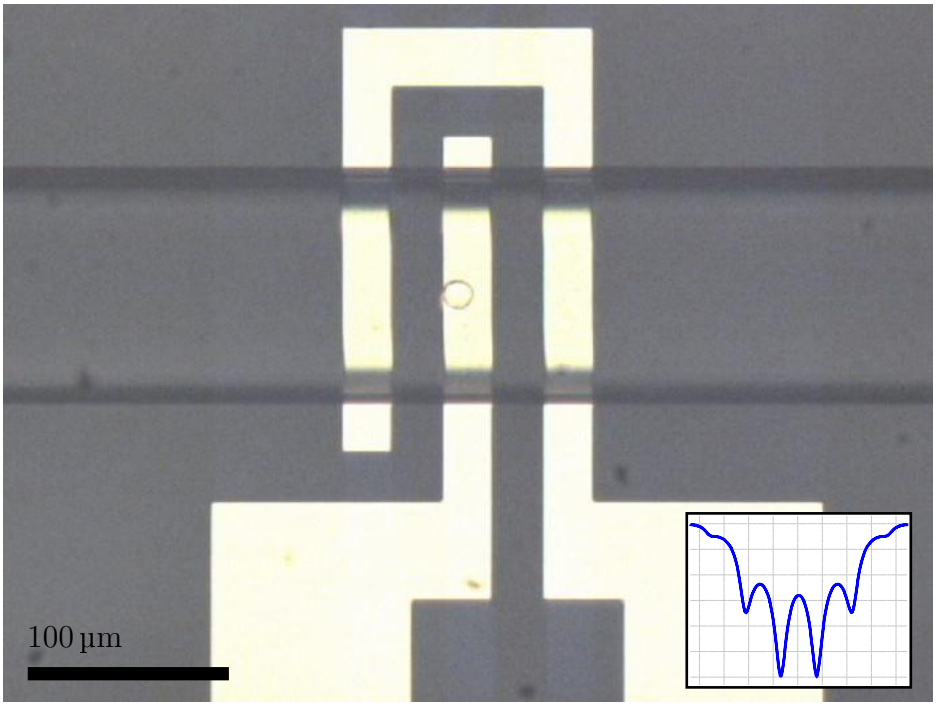

Figure 4.7: Two gap electrode micrograph with inset capacitance signal example.

"Process Maxima and Minima" check box is active, into events.

When data collected using the split electrode configuration is analyzed, peaks due to particle crossing before and after the actuation are fully separated and the signal returns to the baseline in between peaks. This means that signals need to be identified as pre-actuation and post-actuation to identify them as the same particle when the processed file is saved. Once the peakdet function finds the minima, the program will go through each of the peaks and estimate the width of the peak by finding the full width at half maximum associated with each peak.

After events are identified using the method above, user input is needed to identify useful signals and remove signals from multiple particles passing over the detection zone at once, channel purges, and signal discontinuities. Signals are identified by clicking on acceptable peaks and half-maximum points or by clicking the "Collect On-Screen Data" button when everything in the current span is acceptable. When

clicking on individual signals, pre-actuation and post-actuation events are identified by clicking on the left-most or right-most half-maximum point of each peak, respectively.

Once acceptable signals have been identified they can be saved to a CSV file using the "Save P&TT" button. In the case of two gap electrode data, each event is saved in a single row with the in and out flag times being on the outsides and the times and amplitudes of the six possible peaks being in the middle. An example of the formatting of the two gap processed data CSV is shown in Table 4.2 with four of the six peak columns filled. Times are saved in the Excel datenum format, which is scalable to the Matlab datenum by an offset of -693960. In the case of split electrodes, file rows are formatted with the separate in and out flag times surrounding the peak amplitudes and times of the pre-actuation and post-actuation signals. An example of the CSV formatting is shown in Table 4.3, with the data after the baseline subtraction is applied shown in Figure 4.8.

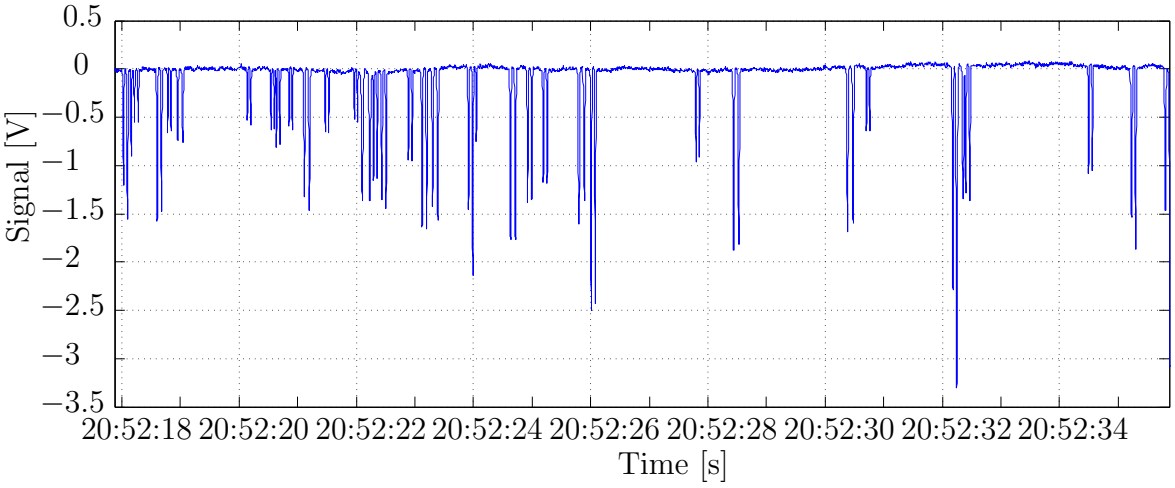

Figure 4.8: Capacitance signal from which data in Table 4.3 was collected.

The following chapter will discuss the results of the two sets of PSS experiments for the three particle sizes. One experiment will be analyzed in detail, using simulation results, in order to extract the Clausius-Mossotti function of the particle. The

remaining experiments are normalized to find the spectral dielectrophoretic response.

Table 4.2: Sample of processed data CSV from two gap electrodes.

Chip Name: IFSMB009			Cell Type: Yeast		Buffer Type: Meth-Blue 89.9uS/cm				
RF Sensing Freq: 1.491GHz			RF Sensing Power: 13 dBm		Modulation Freq: 91.58 kHz				
LIA Time Const: 3 ms			LIA T.C. Slope: 12 dB/oct		LIA Sensitivty: 200 uV				
Start Time: 15-Sep-2010 15:35:48				Sample Rate: 1 kSamples/s					
In Time	Peak 1	Time 1	Peak 2	Time 2	Peak 3	Time 3	Peak 4	Time 4	Out Time	T-Time(s)
16:05:27.217	-2.3895	16:05:27.250	-3.3226	16:05:27.268	-3.2198	16:05:27.286	-2.5328	16:05:27.308	16:05:27.356	0.139
16:05:29.901	-0.6501	16:05:29.940	-0.9416	16:05:29.968	-0.8985	16:05:30.000	-0.7354	16:05:30.035	16:05:30.093	0.192
16:05:30.654	-0.8798	16:05:30.676	-1.1629	16:05:30.723	-0.9494	16:05:30.765	-0.8031	16:05:30.813	16:05:30.832	0.178
16:05:31.923	-1.9546	16:05:31.972	-2.7047	16:05:32.006	-2.2983	16:05:32.039	-1.7820	16:05:32.070	16:05:32.113	0.190
16:05:33.175	-2.6154	16:05:33.241	-3.1970	16:05:33.286	-2.8175	16:05:33.327	-1.9154	16:05:33.366	16:05:33.413	0.238
16:05:34.179	-1.8590	16:05:34.221	-2.6703	16:05:34.250	-2.3163	16:05:34.279	-1.6468	16:05:34.305	16:05:34.342	0.163
16:05:37.204	-1.2217	16:05:37.246	-1.7033	16:05:37.278	-1.5278	16:05:37.308	-1.0876	16:05:37.334	16:05:37.373	0.169
16:05:37.578	-3.0939	16:05:37.625	-4.2045	16:05:37.656	-3.9366	16:05:37.688	-2.7918	16:05:37.716	16:05:37.759	0.181
16:05:38.351	-1.0600	16:05:38.397	-1.4145	16:05:38.429	-1.2361	16:05:38.461	-0.8802	16:05:38.490	16:05:38.534	0.183
16:05:40.567	-2.1443	16:05:40.622	-3.1911	16:05:40.663	-2.7925	16:05:40.705	-2.0991	16:05:40.737	16:05:40.794	0.227
16:05:43.244	-1.3048	16:05:43.292	-1.7221	16:05:43.331	-1.5858	16:05:43.369	-1.0835	16:05:43.405	16:05:43.449	0.205
16:05:45.473	-1.3892	16:05:45.509	-2.3246	16:05:45.537	-1.8734	16:05:45.565	-1.5070	16:05:45.591	16:05:45.624	0.151
16:05:45.749	-2.0361	16:05:45.795	-2.7729	16:05:45.828	-2.6392	16:05:45.861	-1.8042	16:05:45.890	16:05:45.933	0.184
16:05:48.519	-1.5555	16:05:48.565	-2.3562	16:05:48.606	-2.6400	16:05:48.655	-1.8999	16:05:48.710	16:05:48.764	0.245
16:05:49.656	-1.2509	16:05:49.690	-1.6209	16:05:49.714	-1.5584	16:05:49.741	-1.2367	16:05:49.770	16:05:49.815	0.159

Table 4.3: Sample of processed data from split electrodes.

Chip Name: IFSMB010			Cell Type: 6um PSS		Buffer Type: DI Water, 180uS/m			
RF Sensing Freq: 1.584 GHz			RF Sensing Power: 13 dBm			Modulation Freq: 91.6 kHz		
LIA Time Const: 1 ms			LIA T.C. Slope: 12 dB/oct			LIA Sensitivty: 500 uV		
Start Time: 08-Aug-2012 19:55:05			Sample Rate: 1 kSamples/s					
In Time 1	Peak 1	Time 1	Out Time 1	T-Time 1 (s)	In Time 2	Peak 2	Time 2	Out Time 2	T-Time 2 (s)
20:52:18.592	-1.5623	20:52:18.602	20:52:18.611	0.019	20:52:18.667	-1.4658	20:52:18.676	20:52:18.684	0.017
20:52:18.775	-0.6534	20:52:18.782	20:52:18.789	0.014	20:52:18.831	-0.6309	20:52:18.837	20:52:18.845	0.014
20:52:18.943	-0.7364	20:52:18.952	20:52:18.962	0.019	20:52:19.029	-0.7561	20:52:19.038	20:52:19.048	0.019
20:52:20.133	-0.5234	20:52:20.140	20:52:20.148	0.015	20:52:20.191	-0.5678	20:52:20.198	20:52:20.205	0.014
20:52:20.846	-0.5874	20:52:20.853	20:52:20.860	0.014	20:52:20.901	-0.6240	20:52:20.909	20:52:20.916	0.015
20:52:21.464	-0.6446	20:52:21.472	20:52:21.479	0.015	20:52:21.522	-0.6512	20:52:21.530	20:52:21.537	0.015
20:52:22.882	-0.9350	20:52:22.890	20:52:22.897	0.015	20:52:22.944	-0.9500	20:52:22.952	20:52:22.960	0.016
20:52:23.112	-1.6252	20:52:23.121	20:52:23.132	0.020	20:52:23.191	-1.6513	20:52:23.202	20:52:23.210	0.019
20:52:23.291	-1.4241	20:52:23.302	20:52:23.312	0.021	20:52:23.380	-1.5652	20:52:23.392	20:52:23.402	0.022
20:52:24.622	-1.7627	20:52:24.633	20:52:24.642	0.020	20:52:24.705	-1.7617	20:52:24.716	20:52:24.725	0.020
20:52:24.915	-1.3783	20:52:24.924	20:52:24.932	0.017	20:52:24.986	-1.3463	20:52:24.995	20:52:25.003	0.017
20:52:25.182	-1.1664	20:52:25.191	20:52:25.199	0.017	20:52:25.250	-1.1849	20:52:25.258	20:52:25.266	0.016
20:52:27.790	-0.9626	20:52:27.798	20:52:27.805	0.015	20:52:27.847	-0.9114	20:52:27.854	20:52:27.861	0.014
20:52:28.429	-1.8798	20:52:28.440	20:52:28.450	0.021	20:52:28.518	-1.8172	20:52:28.529	20:52:28.539	0.021
20:52:30.372	-1.6904	20:52:30.383	20:52:30.394	0.022	20:52:30.468	-1.6033	20:52:30.479	20:52:30.489	0.021
20:52:30.699	-0.6479	20:52:30.706	20:52:30.713	0.014	20:52:30.756	-0.6488	20:52:30.763	20:52:30.770	0.014
20:52:34.490	-1.0958	20:52:34.498	20:52:34.506	0.016	20:52:34.553	-1.0649	20:52:34.561	20:52:34.568	0.015
20:52:37.210	-1.3239	20:52:37.219	20:52:37.228	0.018	20:52:37.281	-1.3905	20:52:37.291	20:52:37.299	0.018
20:52:37.852	-0.7972	20:52:37.859	20:52:37.866	0.014	20:52:37.909	-0.7904	20:52:37.916	20:52:37.923	0.014
...									

Chapter 5

Results

The final goal of this thesis is to determine the Clausius-Mossotti factor for a population of polystyrene spheres at a range of frequencies. Two sets of experiments were done with polystyrene spheres of nominal diameters 4.65 µm, 5.5 µm, and 9.97 µm in DI water at DEP frequencies ranging from 50 kHz to 10 MHz. This chapter will analyze one population in detail, that being from one of the two 5.5 µm diameter PSS experiments, and extract the Clausius-Mossotti factor spectrum. This will be accomplished by filtering the data and comparing each of the remaining particles with finite element simulations, to determine the Clausius-Mossotti factor as an average over the full population.

The first step in finding the Clausius-Mossotti factor of the experimental data was to run all of the data through the post processing program described in Section 4.2 and extract the peak voltages and times in the capacitance signals for the range of DEP frequencies. The extracted peak voltages will be scaled in order to find the induced capacitance changes. Next, the initial and final particle heights are found using simulation data. The particle heights are then used in combination with particle trajectory simulations to find the Clausius-Mossotti function of one of the 5.5 µm PSS

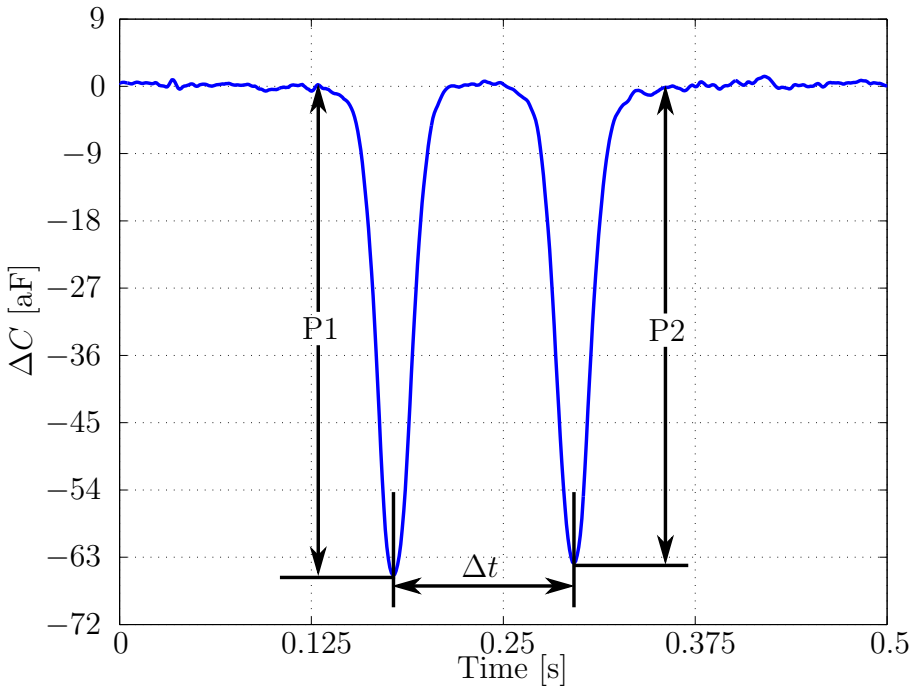

Figure 5.1: Example of the capacitance change, ΔC, of a 5.5 µm diameter PSS in DI water. Here, P1 and P2 show the peak capacitance change of the first and second peak, respectively. Δt is used to calculate the average crossing speed using 215 µm/Δt.

data sets, hereafter for simplicity called the 5.5 µm PSS data set. The sensitivities, and initial and final particle heights are then found for the remaining data sets and a factor called the normalized height difference is plotted to show an approximation of the DEP force on each of the particles.

5.1 Experimental Capacitance Signatures and Particle Heights

In Section 3.3 the sensitivity for the 5.5 µm PSS data set was found. This was accomplished by first simulating the peak capacitance change of 5.5 µm PSS in a laminar flow of DI water with $\langle v \rangle = 2667\,\mu\mathrm{m\,s^{-1}}$ at a range of heights. A curve, shown with the simulated points in Figure 3.8, was then found to approximate the peak ΔC

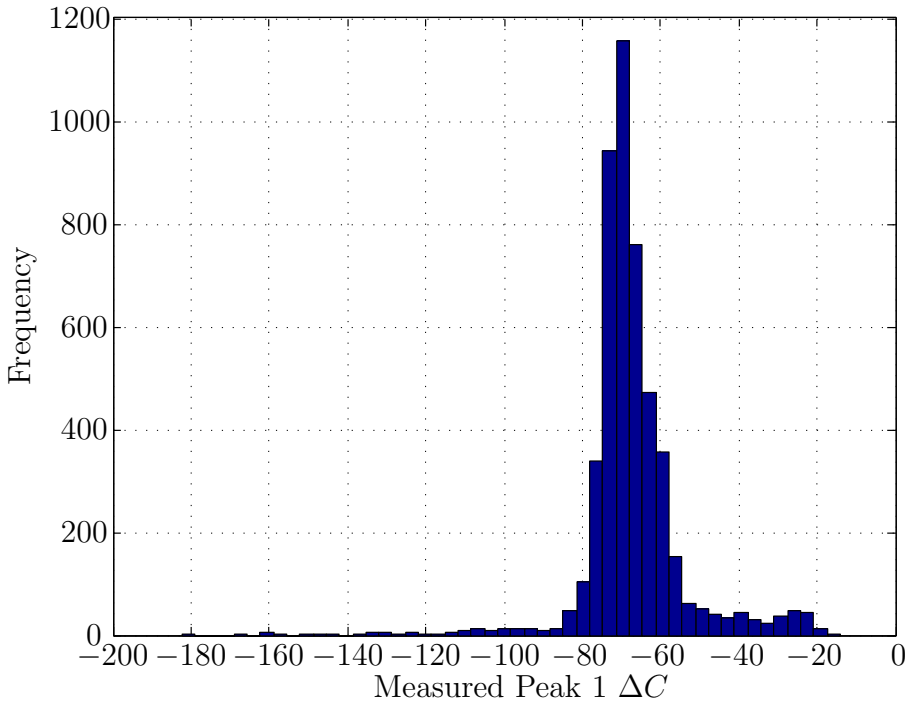

Figure 5.2: Peak capacitance histogram of the 5.5 µm PSS data set, found with a 45 aF V^{-1} scaling factor.

versus average crossing speed for the particles in the lower half of the channel. Next a series of 180 closely spaced PSS signals were selected, having no DEP applied, and the peak signal voltage was plotted against their average crossing speed. Shown in Figure 3.9, the simulation curve was then scaled to fit the experimental data, thus giving the scaling factor to convert the experimental voltage to a capacitance in attofarads (45 aF V^{-1}) for that experiment.

Using the calculated capacitance sensitivity scaling factor (45 aF V^{-1}), every signal voltage peak in the 5.5 µm PSS data set can be converted to an estimated peak capacitance change. A visualization of the peak capacitance changes, ΔC, of the first and second peaks can be found in Figure 5.1. Figure 5.2 shows a histogram of the first peak of each particle crossing from the 5.5 µm PSS data set, scaled by 45 aF V^{-1}. The next step in analyzing the data is to find the initial and final heights of each of the

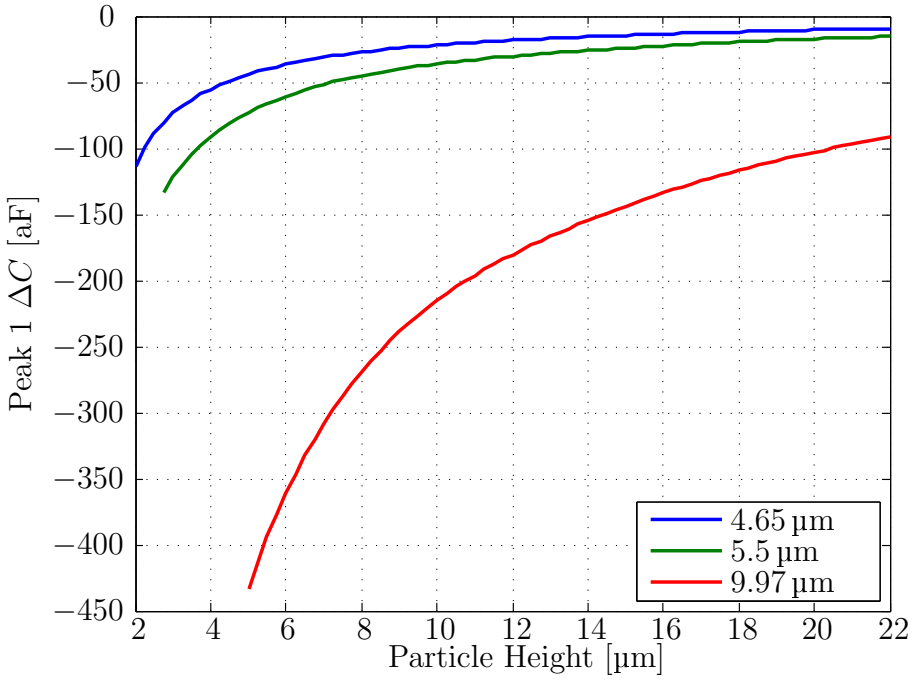

Figure 5.3: Simulated capacitance change, ΔC, of the first peak due to crossing particles of diameters 4.65 µm, 5.5 µm, and 9.97 µm, at a range of heights above the electrodes.

particle crossings using simulations and the calculated experimental peak capacitance changes. Simulated peak capacitances for a range particle heights, shown for all three particle sizes in Figure 5.3, are used to find the heights of each of the particles from their calculated peak capacitances. Simulated peak capacitances are found by finding the minima of the simulated capacitance signatures, found using the method described in Section 2.5, for particles with heights ranging from touching the channel floor to just over halfway up the channel. Using the simulated peak capacitances and the experimental peak capacitances from the 5.5 µm PSS data set, particle elevations were found for each of the passing particles. The first and second peaks of each crossing were mapped using Figure 5.3 to find the initial and final particle elevations, respectively. A histogram of the initial particle elevations is shown in Figure 5.4.

Finding the Clausius-Mossotti function from the experimental data requires ex-

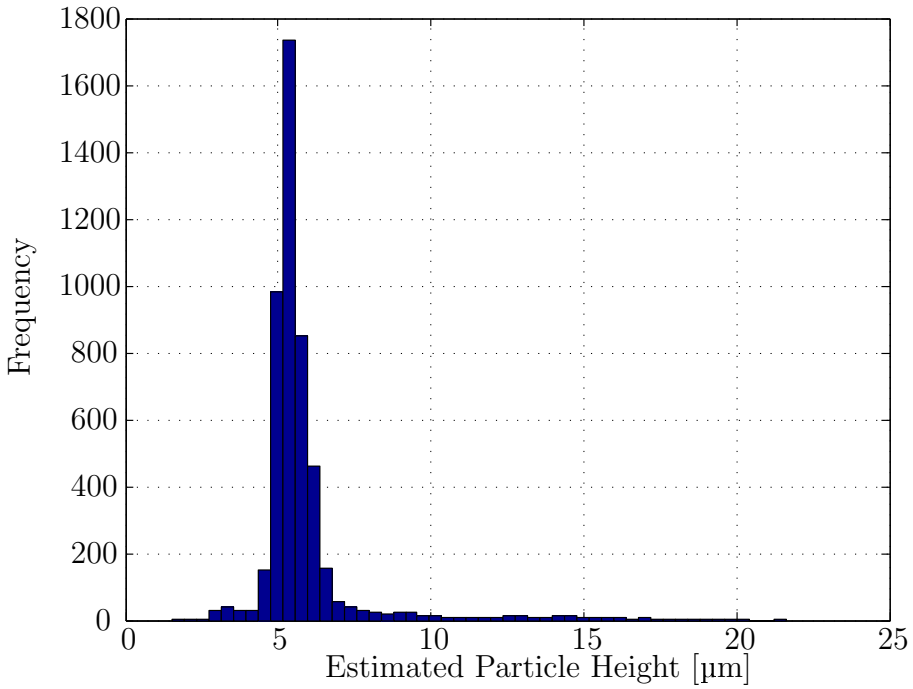

Figure 5.4: Estimated initial particle heights by peak height for the 5.5 µm PSS data set.

tracting forces from a range particle speeds and elevations, fluid velocity profiles, and force magnitudes. In order to use simulations to estimate $\mathrm{Re}\{K\}$, the fluid velocity profile must be known since different fluid velocities will determine how long each of the particles is exposed to the DEP force and therefore, the total change in particle height. Estimating the fluid flow profile can be difficult as it is changing throughout the experiment, with fluid purges occurring roughly every 10 minutes, and fluid pressures varying in between purges. Since particle trajectories are only calculated at fixed fluid velocity profiles, an estimation of the fluid profile over time was needed in order to limit calculation time. It is first assumed that at all times during the experiment a parabolic fluid profile exists over the height of the channel. Using this fact and knowing that the fluid flow is zero at the top and bottom of the channel, the fluid velocity profile can be determined if the particle height and velocity is known for each particle crossing. The following section will discuss finding the fluid velocity

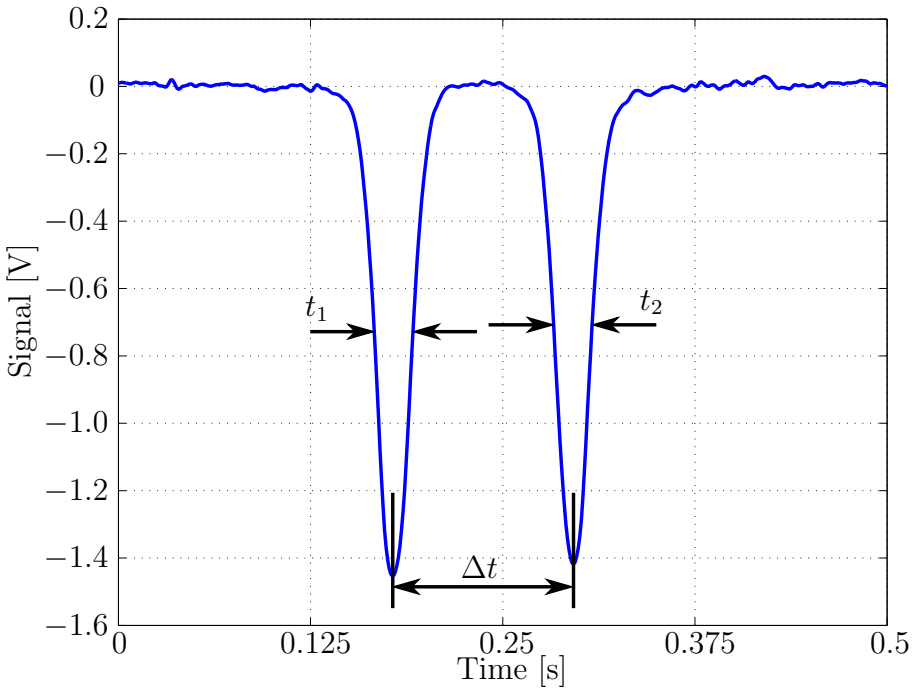

Figure 5.5: Initial and final particle speeds are found by finding a best fit between the inverse peak width at half maximum of the first peak, $1/t_1$, and the average crossing speed, $[215/\Delta t]\mu\mathrm{m\,s^{-1}}$.

profile and using this to filter the data to better match simulated parameters.

5.2 Fluid Velocity Profile Estimation

Typically the particle speed is found using the average crossing speed approximation, the physical distance between the centers of the sensing electrodes divided by the time between the peaks in the capacitance signal. While this is accurate for particles that have minimal or no DEP force acting upon them, if the particle is actuated by more than a few micrometers it can experience a large shift in velocity as it enters an elevation where the fluid flow is significantly faster or slower than its initial elevation. This change in elevation can lead to an averaging effect of the particle velocity and can skew the estimate of the fluid velocity profile. A different method will

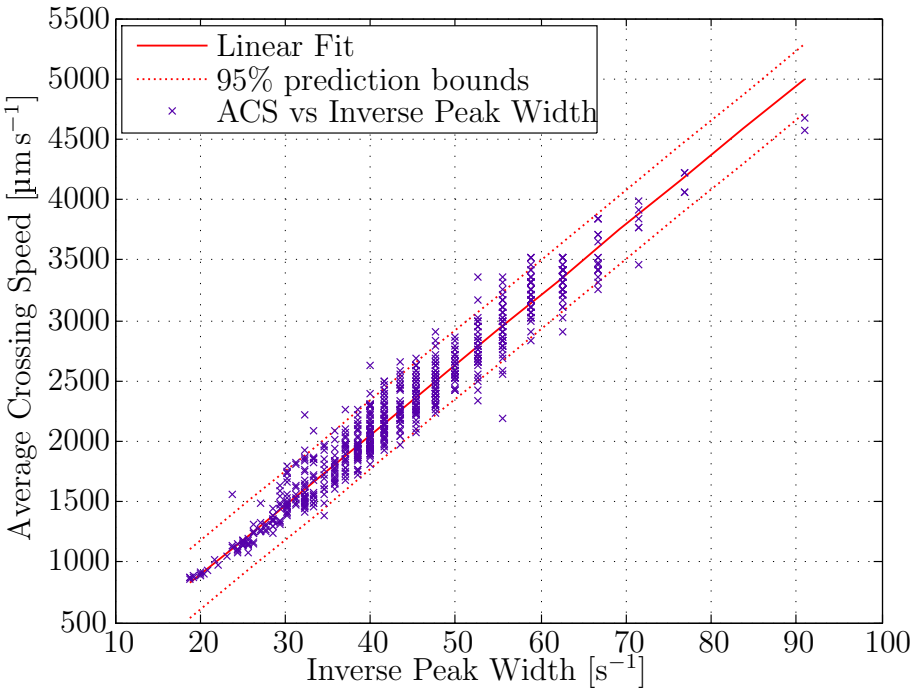

Figure 5.6: Experimental fit for estimating initial particle velocity based on inverse peak width, $v_{init} = 57.92/t_1 - 265.6$.

be described in this section to find an approximation for the instantaneous particle velocity as it enters and exits the detection zone. The particles with no DEP applied are used to find a best fit between the inverse of the full width at half maximum of the first peak when plotted against the average crossing speed as described above. An explanation of the widths and times is shown in Figure 5.5. Unactuated particles are used based on the assumption that their speed is constant over the detection zone so the average crossing speed is an accurate measure of their velocity.

The resulting least-squares linear fit, shown in Figure 5.6, was found to be $v_{init} = 57.92/t_1 - 265.6$ for the 5.5 µm PSS data set. This method of estimating the initial and final velocity using the first and second peaks, respectively, was applied individually to each experiment using the first peak in the set of unactuated particle for a fit.

Using this fit to find the initial velocities of every particle crossing along with the initial heights found earlier, the fluid velocity profile can be calculated through the

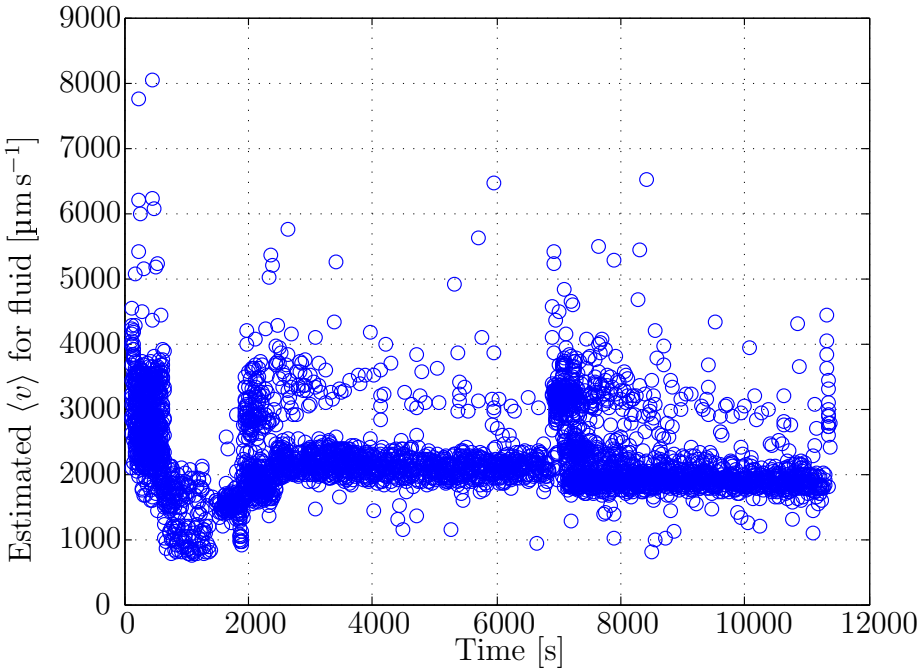

Figure 5.7: Estimated average fluid velocity, $\langle v \rangle$, over time for unactuated 5.5 µm PSS. Calculated from estimated particle height, average crossing speed and assumed parabolic flow profile: $v = 6 \langle v \rangle (h/H)(1 - h/H)$. Note the purges at roughly 2000 s, 7000 s, and at the start of the experiment.

experiment. The average fluid velocity at the time of each crossing is found by:

$$\langle v \rangle = v_{init} \left[6 \frac{h_{init}}{H} \left(1 - \frac{h_{init}}{H} \right) \right]^{-1} \tag{5.1}$$

Figure 5.7 shows the resulting estimated average fluid velocity over time for the 5.5 µm PSS data set. As shown in the figure, the average fluid velocity changes significantly over the course of the experiment. Most notable are the purges at roughly 2000 s, 7000 s, and at the start of the experiment, as well as the slow dropping of the average speed between the purges. The best option to fit the experimental data to simulations is to choose a small range of average fluid velocities which will cover a majority of the experiment and simulate particle trajectories for the average velocity at the center of that range.

5.3 Experimentally Determining the Clausius-Mossotti Function for 5.5 µm Polystyrene Spheres

Determining the Clausius-Mossotti function for each of the experiments will require many simulations for each particle size with a range of Clausius-Mossotti function values, initial particle heights, and the individual mean $\langle v \rangle$ values for each experiment. For this reason, only the 5.5 µm PSS data set will be normalized. This section will describe the simulation, filtering, and normalization to find the average Clausius-Mossotti function for the 5.5 µm PSS data set.

Simulations were then done in COMSOL Multiphysics to find the change in particle elevations for a Clausius-Mossotti factor ranging over all possible values, from -0.5 to 1, and a DEP electrode potential of 4 V peak-to-peak. The simulations used a range of initial particle heights, from 4.7 µm to 7.2 µm, and a constant average fluid velocity of $2000\,\mu\mathrm{m\,s^{-1}}$, which was found to be the best approximation for the average fluid velocity over the course of the experiment. The resulting particle trajectories were calculated and a mapping was produced to find the estimated Clausius-Mossotti factor for each of the particles in the 5.5 µm PSS data set that occurred when the average fluid velocity was in the range $1800\,\mu\mathrm{m\,s^{-1}}$ to $2200\,\mu\mathrm{m\,s^{-1}}$. This was done by interpolating the surface between the simulated points to find the Clausius-Mossotti factor that caused a specific change in height, Δh, for a given initial height, h_{init}. The mapped Clausius-Mossotti factor values for the filtered data were then sorted by DEP frequency and a mean was found for each frequency. Figure 5.8 shows the resulting Clausius-Mossotti spectra for each of the DEP frequencies of the 5.5 µm PSS data set, when compared against the theoretical $\mathrm{Re}\{K\}$ spectra, calculated using $\varepsilon_1 = 78\varepsilon_0$, $\sigma_1 = 180\,\mu\mathrm{S\,m^{-1}}$, $\varepsilon_2 = 2.5\varepsilon_0$, $K_s = 2.56\,\mathrm{nS}$ [11], $\sigma_{2,bulk} = 100\,\mathrm{aS\,m^{-1}}$ [12], $a = 2.75\,\mu\mathrm{m}$,

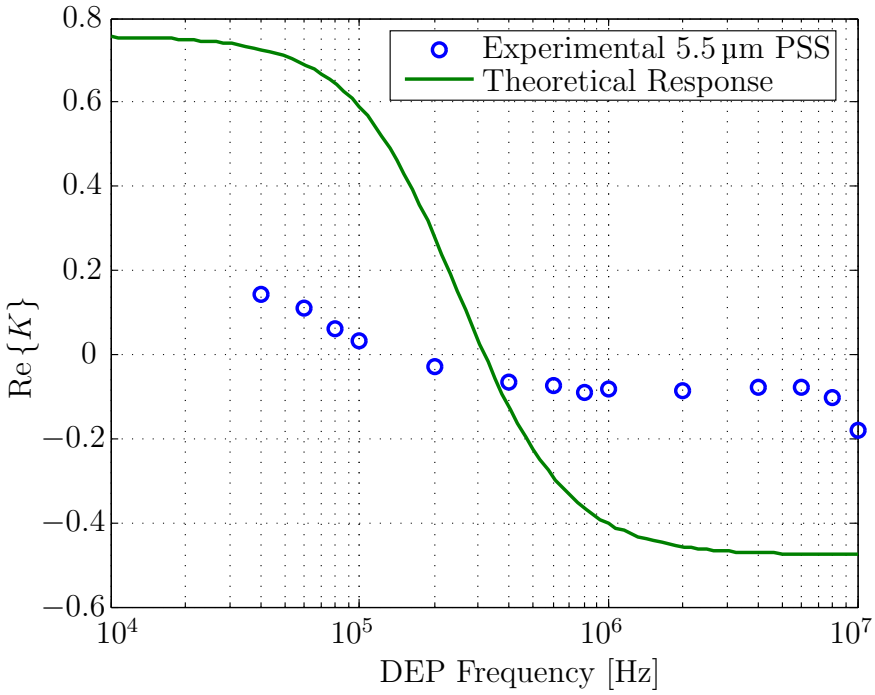

Figure 5.8: Experimental and theoretical Re$\{K\}$ spectra for 5.5 µm PSS data set. Experimental Re$\{K\}$ mapped using simulations with $\Phi_{DEP} = 4\,\mathrm{V}$ peak-to-peak

.

making

$$\mathrm{Re}\left\{K\left(\omega\right)\right\} = \frac{3.74 \times 10^{-6} - 1.20 \times 10^{4}\varepsilon_0^2\omega^2}{4.94 \times 10^{-6} + 2.51 \times 10^{4}\varepsilon_0^2\omega^2} \tag{5.2}$$

for this case.

As is clearly shown in Figure 5.8, the simulated mapping produced a significantly different Re$\{K\}$ spectra from that of the theoretical plot. The crossover frequency is similar, though slightly lower than the theoretical spectrum, meaning that most of the frequency dependent simulation parameters are likely close. However, the magnitude of the Re$\{K\}$ values have been dramatically underestimated. This is likely due to an overestimation in the experimental DEP electrode potential, causing an overestimation of Δh for a given Re$\{K\}$ value. This error is likely due to an unexpectedly low impedance of the DEP application apparatus, including the cables

and electrodes, making the high impedance approximation no longer valid.

Two additional simulation sets were done in order to approximate the DEP electrode potential. The first set, with an electrode potential of 2 V peak-to-peak, led to a mapping that produced Clausius-Mossotti factor values outside the possible range (-0.5 to 1). The filtered results are shown in Figure 5.9, all points outside the valid Clausius-Mossotti factor range have been removed. Next simulations were done with an electrode potential of 2.7 V peak-to-peak which produced more accurate results. This final set of simulations was used to create a surface mapping, shown in Figure 5.10, which was used to map the experimental data to the simulated Clausius-Mossotti factors, as described above. Values were separated into DEP frequencies and the average $\mathrm{Re}\{K\}$ value was found for each frequency. The calculated $\mathrm{Re}\{K\}$ spectra, found using the experimental data normalized with the 2.7 V peak-to-peak simulations, along with the theoretical spectrum is shown in Figure 5.11.

Variations in the crossover frequency from the theoretical DEP spectrum were seen and can be partially attributed to the overestimation of the lift force in the simulation data, which will shift the crossover point to a higher Clausius-Mossotti factor value, or in this case to a lower frequency. Two simulations were done with $\mathrm{Re}\{K\} = -0.5$ to compare the effect of the estimated lift force from Section 2.4, with a lift force constant of $C = 0.106$, with trajectories having no lift force. The absence of the lift force, comparison shown in Figure 5.12, results in a significant reduction in Δh, meaning the experimental curve will be shifted to lower frequencies.

A shift in the crossover frequency could also be due to inaccurate measurement of the medium conductivity or, more significantly, overestimation of the particle conductivity as shown in Figure 5.13 where the particle conductivity was changed from $1.862\,\mathrm{mS\,m^{-1}}$ to $1.0\,\mathrm{mS\,m^{-1}}$. Errors can also be attributed to the over or underestimation of the DEP voltage on the electrodes in experiments, and can lead to mapped

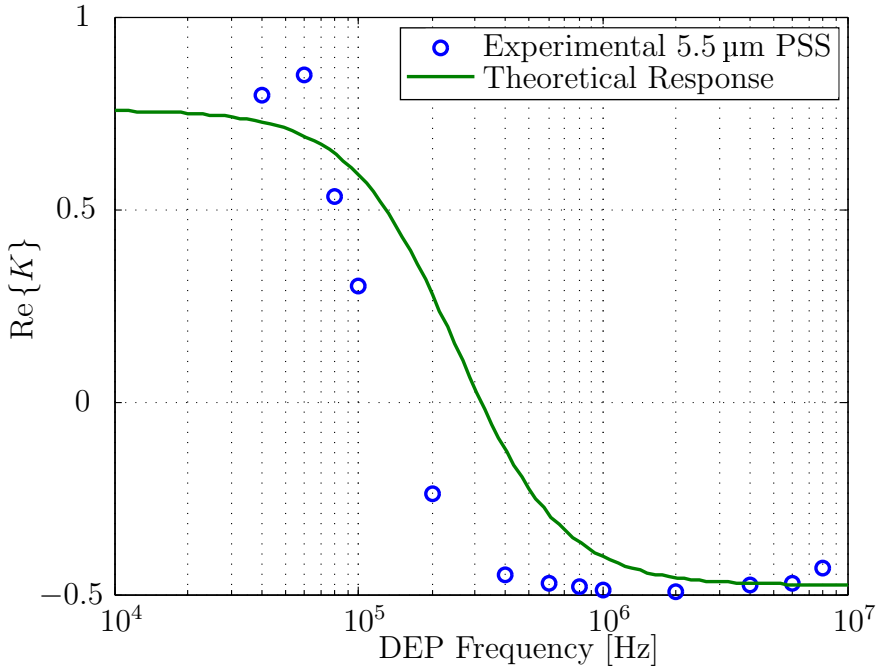

Figure 5.9: Experimental and theoretical Re$\{K\}$ spectra for the 5.5 µm PSS data set. Experimental Re$\{K\}$ found using mapping created from simulations with $\Phi_{DEP} = 2\,\mathrm{V}$peak-to-peak. Re$\{K\}$ values have been filtered average only valid points, that is Re$\{K\} \in [-0.5, 1]$.

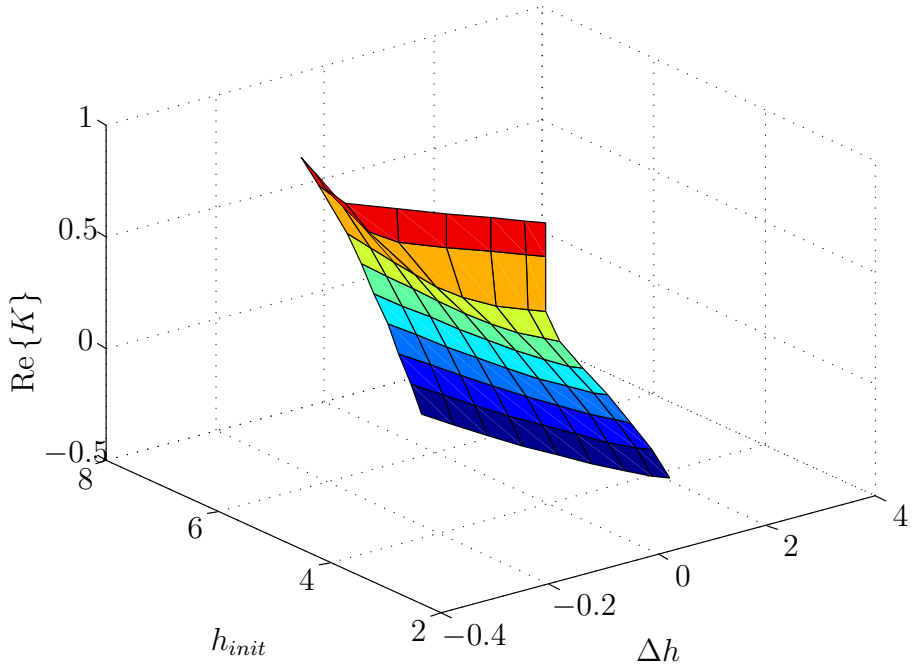

Figure 5.10: Simulated Re$\{K\}$ mapping for values of Δh and h_{init}. Simulation done for $a = 2.75\,\mu\mathrm{m}$, $\langle v \rangle = 2000\,\mu\mathrm{m\,s^{-1}}$, and $\Phi_{DEP} = 2.7\,\mathrm{V_{pp}}$.

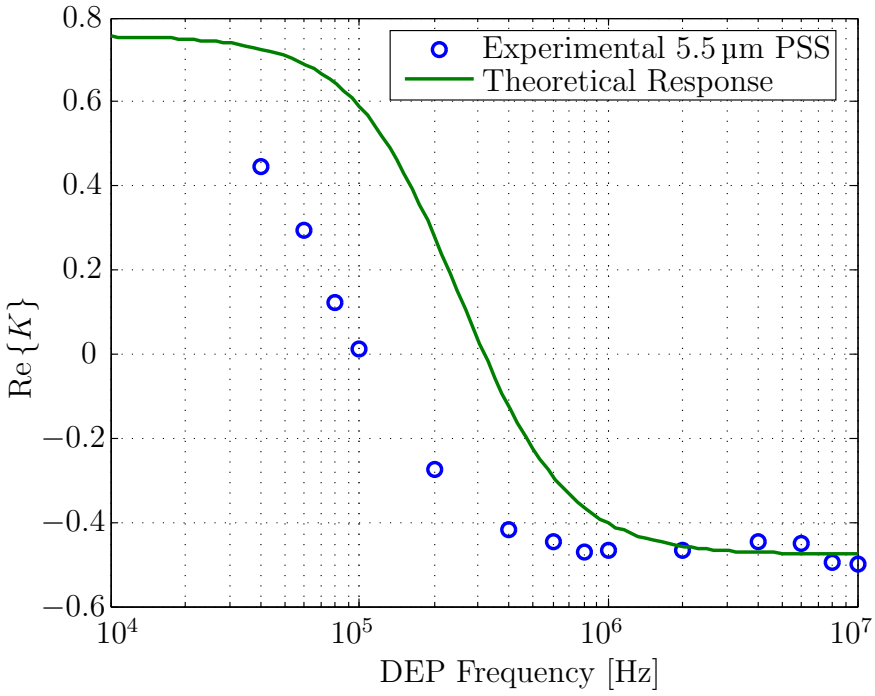

Figure 5.11: Experimental and theoretical Re$\{K\}$ spectra for the 5.5 µm PSS data set. Experimental Re$\{K\}$ found using mapping shown in Figure 5.10 with $\Phi_{DEP} = 2.7\,\text{V}_{\text{peak-to-peak}}$.

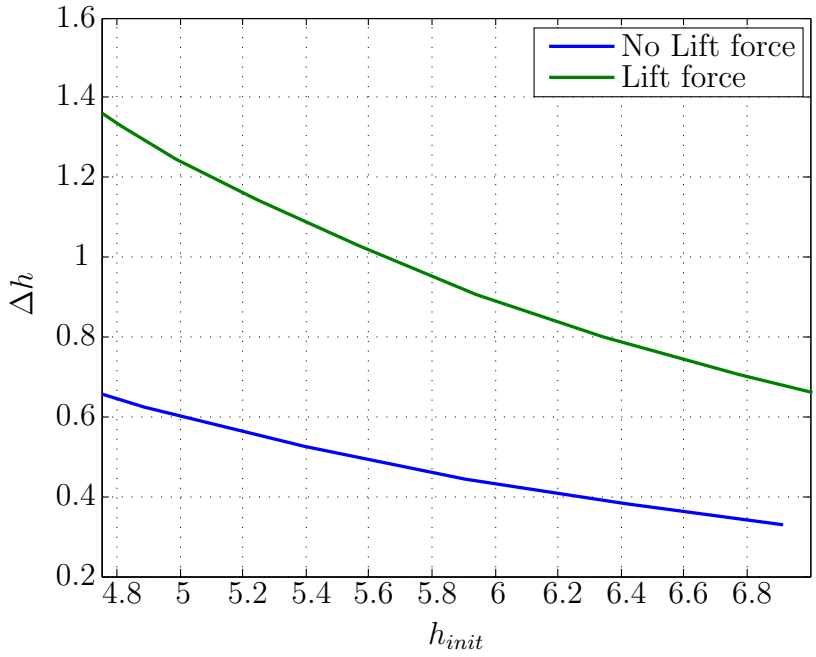

Figure 5.12: Simulation to show differences in Δh for particle trajectories with the full lift force, $F_{lift} = C\frac{6\eta a^3\langle v\rangle}{H(h-a)}\hat{a}_y, a \leq h \leq H/2$ with $C = 0.106$ [1], and those with no lift force included.

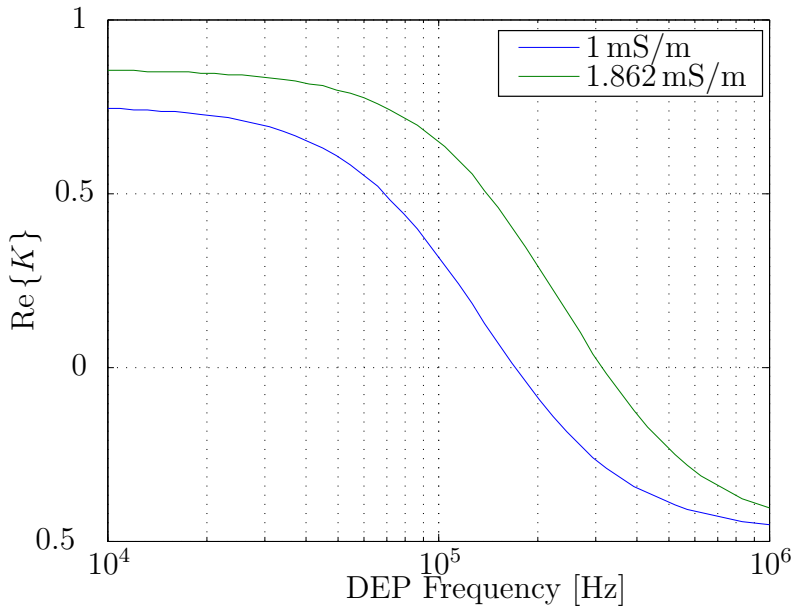

Figure 5.13: Demonstration of the variation in crossover due to changes in particle conductivity.

$\mathrm{Re}\{K\}$ values which have a range that is smaller or larger than the experimental results, respectively. Direct measurements of the DEP voltage at the time of the experiments were not made and would be dependent on frequency due to the highly capacitive impedance of the connecting cables for the DEP signal.

Other factors in the variations in the Clausius-Mossotti factor spectra include the uncertainty in the sensitivity measurement ($45\,\mathrm{aF\,V^{-1}}$) found in Section 3.3 and the particle and fluid velocity estimate. The sensitivity estimate can change the estimated heights which will change the total force on the particle. Uncertainty in the initial particle speed can lead to plotting of particles flowing in an average fluid velocity, $\langle v \rangle$, which deviates significantly from the simulated value of $2000\,\mu\mathrm{m\,s^{-1}}$. Filtering will also play a role in the uncertainty of the plotted Clausius-Mossotti factor, as a higher range of allowed $\langle v \rangle$ can lead to more dispersed results since values can deviate from the simulated $\langle v \rangle$ value. An estimated average fluid of $1800\,\mu\mathrm{m\,s^{-1}}$ to $2200\,\mu\mathrm{m\,s^{-1}}$ is used in the above data, in order to keep the number of crossings for each frequency

above 50.

5.4 Normalization and Plotting of PSS Data

Due to the time intensive act of simulating the full range of Clausius-Mossotti factors, with a range of initial particle heights for each particle size and average fluid velocities, simulations were only done to normalize the 5.5 µm PSS data set at an average fluid velocity of 2000 µm s^{-1}. This section will describe the filtering, normalization, and plotting of the six sets of PSS data in order to compare them with the theoretical Clausius-Mossotti spectra.

The sensitivities of the remaining experiments were individually found using the method shown in Section 3.3, which found the sensitivity of the 5.5 µm PSS data set. The resulting sensitivities, shown in Table 5.1 under **Sens.**, where then applied to find the two peak capacitances of each of the passing particles and the same height estimation was done using the curves shown in Figure 5.3. The particle speeds were estimated using a least squares fit, as shown in Figure 5.6 for the 5.5 µm PSS data set, to find the relationship between the inverse full width at half maximum and the average crossing speed for the unactuated particles in each experiment. These fits, the coefficients of which are shown in Table 5.1 under a and b for $v_{init,fin} = a/t_{1,2} + b$, were then applied to each of the crossing particles to find the initial and final particle speeds. The particle velocities were then used to find the average fluid velocity at the time of each crossing and to filter out particles in an average flow velocity that are not within 200 µm s^{-1} of the mean $\langle v \rangle$ shown in Table 5.1.

In place of fitting the experimental data to the simulated Re$\{K\}$, h_{init}, Δh surface, as in Section 5.3, an approximate measure of the relative force exerted on the particle is used in order to reduce simulation time. Using the changes in height, as well as the

Table 5.1: Sensitivity estimates, least squares particle velocity linear fit, and estimated mean $\langle v \rangle$ for each experiment. Sensitivity and least squares fit found using same method as the 5.5 µm PSS data set. Fit takes the form: $v_{init,fin} = a/w_{1,2} + b$, where $v_{init,fin}$ is the estimated particle velocity for a peak width of $w_{1,2}$.

Particle size	**Exp. #**	**Sens.** [aF V^{-1}]	a	b	**mean** $\langle v \rangle$ [µm s^{-1}]
4.65 µm	1	24	62.01	−318.4	850
4.65 µm	2	45	54.98	−190.4	1500
5.50 µm	1	24	62.01	−618.4	1500
5.50 µm	2	45	57.92	−265.6	2000
9.97 µm	1	25	56.54	−148.7	1400
9.97 µm	2	35	59.42	−426.4	2200

initial height of the filtered data, the normalized height difference is found for each of the particle crossings:

$$\mathbb{H} = \frac{h_{fin} - h_{init}}{h_{init}} = \frac{\Delta h}{h_{init}} \tag{5.3}$$

This normalized height difference will is simalar to the force index, defined in [1] as $2\frac{R-L}{R+L}$, where R and L are the right and left signal peaks, respectively. The force index is more immune to the initial particle height than simply using the absolute change in particle height. However the force index, is dependent on the signal voltage, which is directly proportional to the change in capacitance, ΔC, and is therefore a non-linear mapping based on height and force. The normalized height difference acts to eliminate the non-linearity in the capacitance measurement that is present in the force index. The normalized height difference, however, is not immune to changes in particle size, making it a measure of the total force exerted on the particle rather than a direct measure of $\mathrm{Re}\{K\}$. It is also a function of the particle velocity as particles moving faster in the channel will experience the DEP force for a shorter time and will therefore be deflected less. Figure 5.14 to 5.19 show the results of the $\mathbb{H}$ spectra, plotted as $-\mathbb{H}$ to match the $\mathrm{Re}\{K\}$ spectra.

Figure 5.14 and 5.15 show the response of the first and second 5.5 µm PSS experiments, respectively. Ideally, the responses of the two experiments would be the same. However, due to the significant change in the mean $\langle v \rangle$ between the two, 1500 µm s^{-1} to 2000 µm s^{-1}, there is a significant shift towards zero for the second experiment since the particles are, on average, moving faster and experience the DEP force for a shorter time. The two responses do however have similar crossover frequencies Figure 5.16 and 5.17 show the normalized height difference for the first and second set of 9.97 µm PSS experiments, respectively. As expected, the height difference generally has a larger magnitude than the 5.5 µm PSS experiments. This is due to the a^3 term in the time averaged DEP force equation, making larger particles have larger forces exerted on them in the same field. The same trend is true as in the 5.5 µm PSS, the second experiment sees a response closer to zero since the particles are, on average, moving at a faster speed than the first experiment. Figure 5.18 and 5.19 show the normalized height difference of the first and second 4.65 µm PSS experiments, respectively. The first 4.65 µm PSS experiment shows average fluid velocities much lower than that of any of the other experiments. As a consequence of this the normalized height difference is quite large, but generally matches the expected trend. The second 4.65 µm PSS experiment shows speeds closer to that of the other experiments, but has a far less consistent distribution in height changes. This could be caused by a poor connection on the DEP electrodes, the accidental collection of multiple simultaneous passes of multiple particles, or by an unknown source of noise during the experiment.

In conclusion, the normalized height difference provides a measurement of the relative change in height of a particle subject to a DEP force. While not as immune to changes in fluid velocity profiles as the $\mathrm{Re}\{K\}$ method used in Section 5.3, it help to eliminate the of effects of changes in system sensitivity and removes the nonlinearity in height by converting values from capacitances to physical heights.

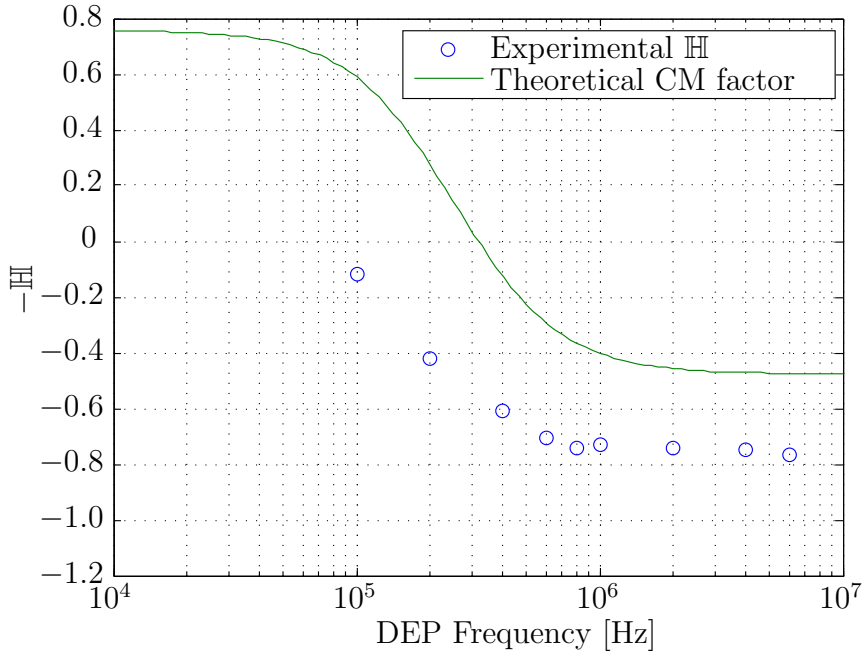

Figure 5.14: Normalized height difference spectra for the first 5.5 µm PSS experiment (parameters shown in Table 5.1) with overlaid theoretical Re$\{K\}$ spectra. Sensitivity was found to be 24 aF V^{-1}. Average fluid velocity was estimated to be 1500 µm s^{-1}.

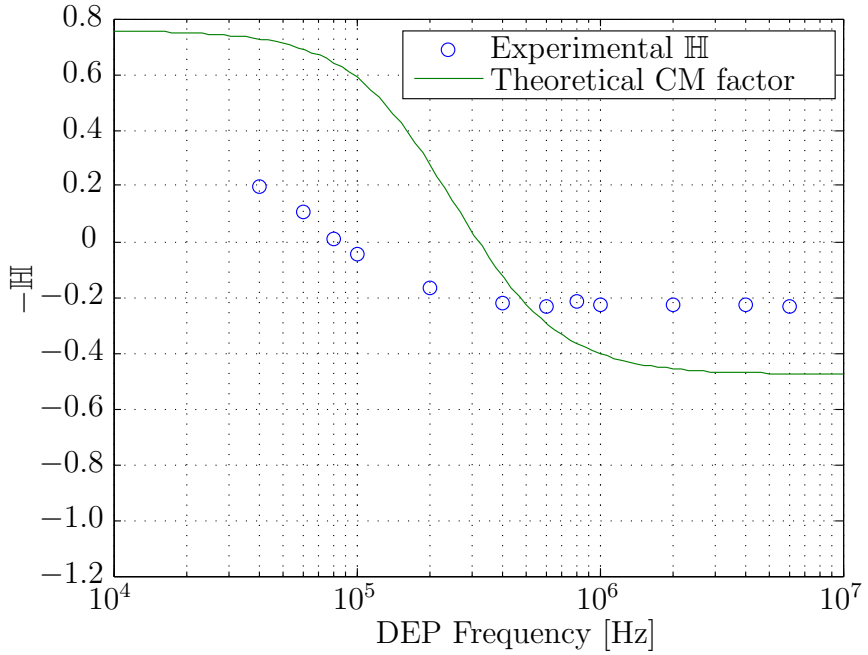

Figure 5.15: Normalized height difference spectra for the second 5.5 µm PSS experiment (parameters shown in Table 5.1) with overlaid theoretical Re$\{K\}$ spectra. Sensitivity was found to be 45 aF V^{-1}. Average fluid velocity was estimated to be 2000 µm s^{-1}.

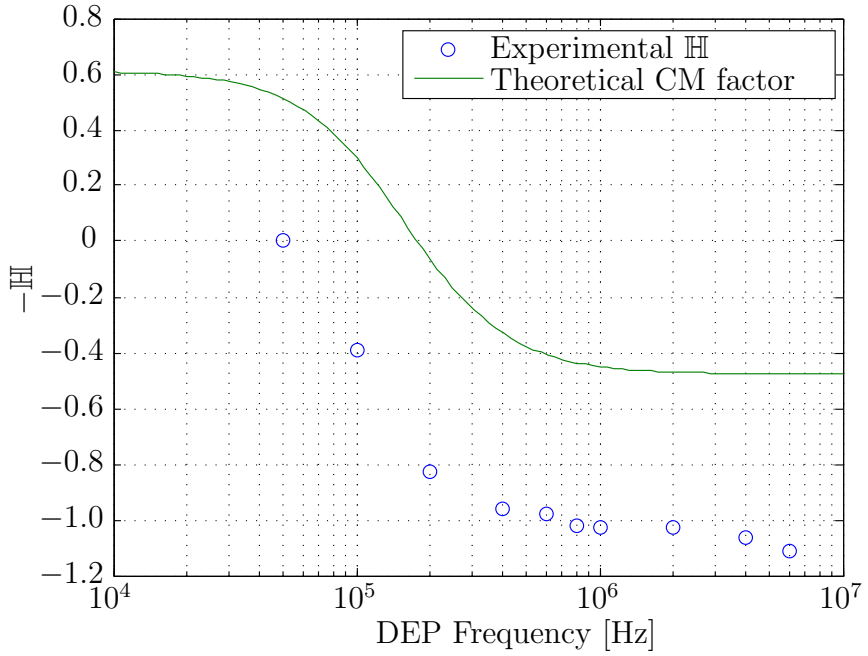

Figure 5.16: Normalized height difference spectra for the first 9.97 µm PSS experiment (parameters shown in Table 5.1) with overlaid theoretical Re$\{K\}$ spectra. Sensitivity was found to be 25 aF V^{-1}. Average fluid velocity was estimated to be 1400 µm s^{-1}.

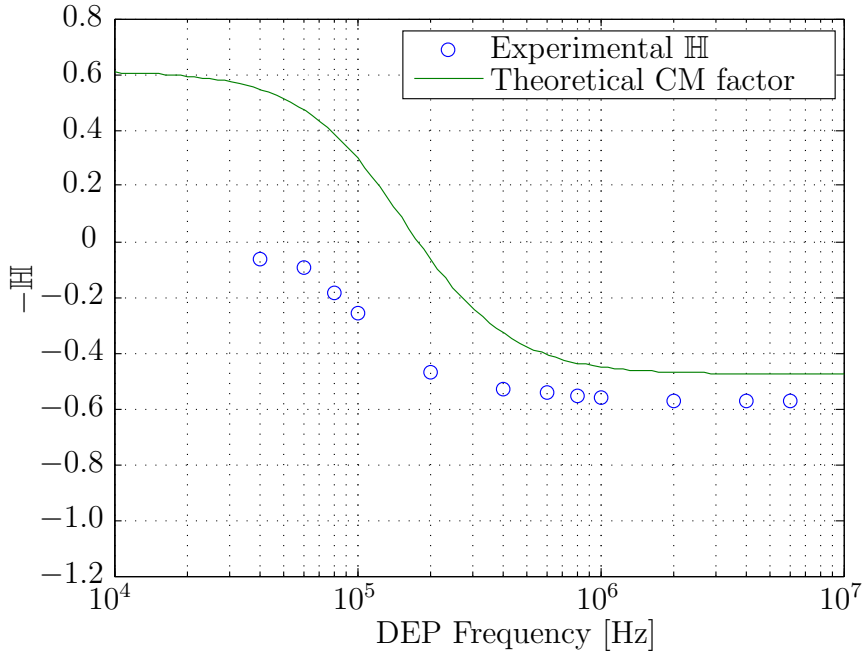

Figure 5.17: Normalized height difference spectra for the second 9.97 µm PSS experiment (parameters shown in Table 5.1) with overlaid theoretical Re$\{K\}$ spectra. Sensitivity was found to be 35 aF V^{-1}. Average fluid velocity was estimated to be 2200 µm s^{-1}.

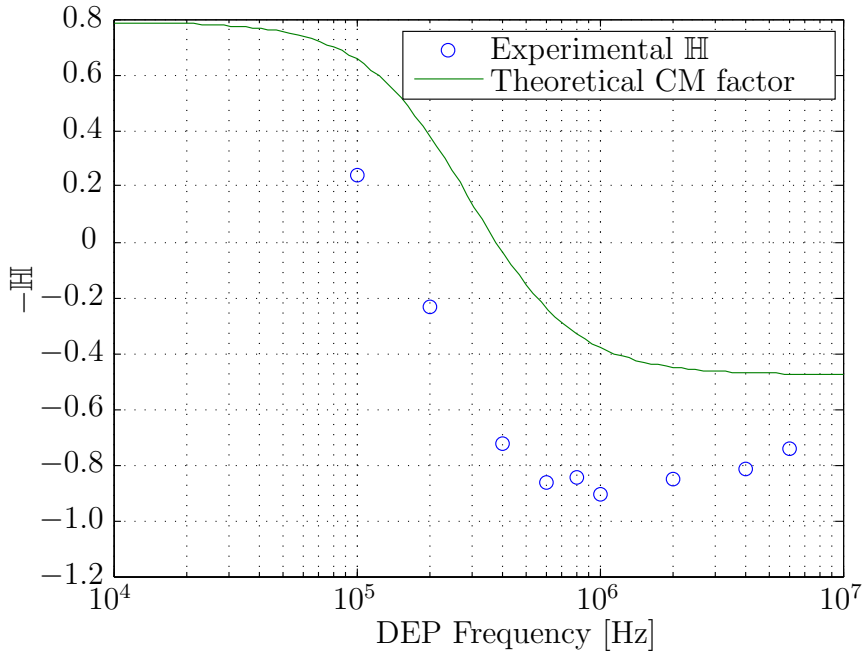

Figure 5.18: Normalized height difference spectra for the first 4.65 µm PSS experiment (parameters shown in Table 5.1) with overlaid theoretical Re$\{K\}$ spectra. Sensitivity was found to be 24 aF V^{-1}. Average fluid velocity was estimated to be 850 µm s^{-1}.

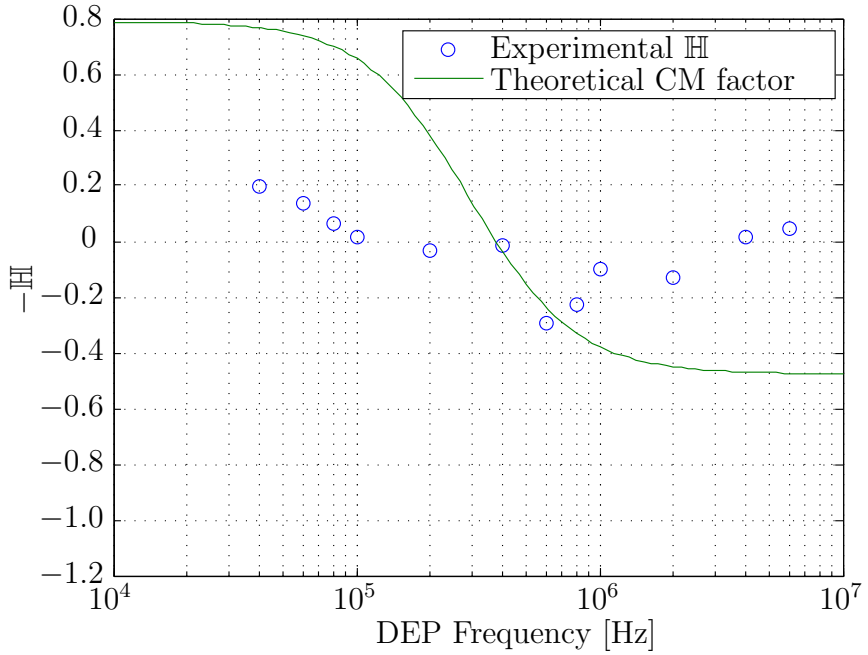

Figure 5.19: Normalized height difference spectra for the second 4.65 µm PSS experiment (parameters shown in Table 5.1) with overlaid theoretical Re$\{K\}$ spectra. Sensitivity 45 aF V^{-1} was used in the plot, with and average fluid velocity of 1500 µm s^{-1}.

Chapter 6

Conclusion and Recommended Future Work

The development of the signal processing and data acquisition systems described in this thesis has allowed for the rapid collection and processing of raw capacitance signals into a few parameters to describe each particle. The programs created allow for analysis of large data sets consisting of 5000+ particle crossing events with a collection and processing time of a day or two. Once the peak amplitudes, widths, and times are extracted from the data using the data processing software, they are used to reconstruct to the initial and final particle speeds and heights, giving the full picture of the net effect of the DEP force on the passing particles.

The analysis technique used in this thesis, while time consuming, provides a mapping of the change in signal due to a dielectrophoretic force to the Clausius-Mossotti factor for that particle. The technique of finding the sensitivity for a given experiment by mapping signal voltages to capacitance changes allows for a direct comparison with simulated data, and the ability to find initial and final heights of particles. This is directly applicable to particles with a small variance in size and well defined high fre-

quency properties. A new technique of finding the initial particle velocity even when the particle is subject to large dielectrophoretic forces was used to find the average fluid velocity at the time of the particle crossing. This was possible by solving the parabolic fluid flow equation for the average fluid velocity using the estimated heights and velocities of each particle. It was then possible to filter the data to limit the range of fluid velocity profiles and use simulations with a fluid velocity only in that range, rather than simulating using multiple fluid velocity profiles. By simulating the particle trajectories at a range of initial heights and Clausius-Mossotti factors, a mapping was produced to find the Clausius-Mossotti factor for each particle based on their initial and final heights.

Due to the simulation time required for finding the Clausius-Mossotti factor for one set of data, the full analysis was not performed on the five remaining data sets. Instead the capacitance sensitivities as well as the initial and final particle heights were found for each of the remaining data sets. The data could then be filtered to limit the range of fluid velocity profiles within each experiment. The remaining data points were averaged and the normalized height change was plotted for each, to be an indication of the DEP force on the particle.

For additional work on the aspects of signal normalization discussed in this work I would recommend that additional simulation be done to find trajectories for particles with a range of DEP forces and fluid velocities. The simulation results could then be interpolated in order to develop a mapping that could be used to find the total forces and Clausius-Mossotti factors of experimental particles in a range of fluid flows. The technique could also benefit from having two sets of two-gap electrodes, one each before and after the actuation, to allow for fast estimation of particle height and

total sensitivity rather than curve fitting a relatively small block of data. Another recommendation I would make would be to use a channel of the data acquisition module to periodically sample the DEP voltage as close to the chip as possible. This would allow for the correction of the cable loss as a function of frequency and in general give a more accurate measure of the DEP voltage being applied.

The bulk of the suggestions I would make regarding the operation of the microfluidic apparatus and interferometric system are in the process of being carried out. First I would recommend a program to automate the processing of data collected with the system and eventually allow for real-time processing. Another recommendation I would make, which is commonly pointed out as a benefit of the all electronic approach to cell detection, would be miniaturization. This would eliminate the need for a large electrical isolation chamber that houses the optics and interferometer electronics.

References

[1] M. Nikolic−Jaric, S. F. Romanuik, G. A. Ferrier, *et al.*, "Electronic detection of dielectrophoretic forces exerted on particles flowing over interdigitated electrodes," *Biomicrofluidics*, vol. 6, no. 2, p. 024117, 2012. [Online]. Available: http://link.aip.org/link/?BMF/6/024117/1

[2] S. Romanuik, "A microflow cytometer with simultaneous dielectrophoretic actuation for the optical assay and capacitive cytometry of individual fluid suspended bioparticles," Master's thesis, University of Manitoba, September 2009. [Online]. Available: http://hdl.handle.net/1993/3205

[3] N. G. Green, A. Ramos, A. González, *et al.*, "Fluid flow induced by nonuniform ac electric fields in electrolytes on microelectrodes. i. experimental measurements," *Phys. Rev. E*, vol. 61, pp. 4011–4018, Apr 2000. [Online]. Available: http://link.aps.org/doi/10.1103/PhysRevE.61.4011

[4] M. Nikolic-Jaric, T. Cabel, E. Salimi, *et al.*, "Differential electronic detector to monitor apoptosis using dielectrophoresis-induced translation of flowing cells (dielectrophoresis cytometry)," *Biomicrofluidics*, vol. 7, no. 2, p. 024101, 2013. [Online]. Available: http://link.aip.org/link/?BMF/7/024101/1

[5] H. A. Pohl, "The motion and precipitation of suspensoids in divergent electric fields," *Journal of Applied Physics*, vol. 22, no. 7, pp. 869 –871, jul 1951.

[6] H. A. Pohi and I. Hawk, "Separation of living and dead cells by dielectrophoresis," *Science*, vol. 152, no. 3722, pp. pp. 647–649, 1966. [Online]. Available: http://www.jstor.org/stable/1719000

[7] J. S. Crane and H. A. Pohl, "A study of living and dead yeast cells using dielectrophoresis," *Journal of The Electrochemical Society*, vol. 115, no. 6, pp. 584–586, 1968. [Online]. Available: http://jes.ecsdl.org/content/115/6/584.abstract

[8] ——, "Theoretical models of cellular dielectrophoresis," *Journal of Theoretical Biology*, vol. 37, no. 1, pp. 15 – 41, 1972. [Online]. Available: http://www.sciencedirect.com/science/article/pii/0022519372901130

[9] H. Pohl, K. Kaler, and K. Pollock, "The continuous positive and negative dielectrophoresis of microorganisms," *Journal of Biological Physics*, vol. 9, no. 2, pp. 67–86, 1981. [Online]. Available: http://dx.doi.org/10.1007/BF01987284

[10] T. Jones, *Electromechanics of Particles*, 1st ed. New York: Cambridge University Press, 1995.

[11] T. Honegger, K. Berton, E. Picard, *et al.*, "Determination of clausius-mossotti factors and surface capacitances for colloidal particles," *Applied Physics Letters*, vol. 98, no. 18, p. 181906, 2011. [Online]. Available: http://link.aip.org/link/?APL/98/181906/1

[12] G. Ferrier, "Electrical detection and actuation of single biological cells with application to deformability cytometry for markerless diagnostics," Ph.D. dissertation, University of Manitoba, Winnipeg, MB, 2003. [Online]. Available: http://hdl.handle.net/1993/5039

[13] K. Asami, "Characterization of heterogeneous systems by dielectric spectroscopy," *Progress in Polymer Science*, vol. 27, no. 8, pp. 1617 – 1659, 2002. [Online]. Available: http://www.sciencedirect.com/science/article/pii/S0079670002000151

[14] L. Benguigui and I. J. Lin, "More about the dielectrophoretic force," *Journal of Applied Physics*, vol. 53, no. 2, pp. 1141–1143, 1982. [Online]. Available: http://link.aip.org/link/?JAP/53/1141/1

[15] R. Hölzel, "Electrorotation of single yeast cells at frequencies between 100 hz and 1.6 ghz," *Biophysical Journal*, vol. 73, no. 2, pp. 1103 – 1109, 1997. [Online]. Available: http://www.sciencedirect.com/science/article/pii/S0006349597781426

[16] (2009, September) Sensonit glass-based microfluidic technology with metallization: Design rules and process steps. CMC Microsystems. Kingston, ON. [Online]. Available: http://products.cmc.ca/Members/Download.ashx?id=18592

[17] "Polybead® Microspheres data sheet," Polysciences Inc., Warrington, PA, USA. [Online]. Available: http://www.polysciences.com/SiteData/docs/TDS%20788/db0c191bb5cd2307/TDS%20788.pdf

[18] M. Nikolic-Jaric, S. F. Romanuik, G. A. Ferrier, *et al.*, "Microwave frequency sensor for detection of biological cells in microfluidic channels," *Biomicrofluidics*, vol. 3, no. 3, p. 034103, 2009. [Online]. Available: http://link.aip.org/link/?BMF/3/034103/1

[19] R. Buchner, J. Barthel, and J. Stauber, "The dielectric relaxation of water between 0c and 35c," *Chemical Physics Letters*, vol. 306, no. 12, pp. 57 – 63,

1999. [Online]. Available:
http://www.sciencedirect.com/science/article/pii/S0009261499004558

[20] M. Nikolic-Jaric, G. A. Ferrier, D. J. Thomson, *et al.*, "Dielectric response of particles in flowing media: The effect of shear-induced rotation on the variation in particle polarizability," *Phys. Rev. E*, vol. 84, p. 011922, Jul 2011. [Online]. Available: http://link.aps.org/doi/10.1103/PhysRevE.84.011922

[21] J. Brody, P. Yager, R. Goldstein, *et al.*, "Biotechnology at low reynolds numbers," *Biophysical Journal*, vol. 71, no. 6, pp. 3430 – 3441, 1996. [Online]. Available:
http://www.sciencedirect.com/science/article/pii/S0006349596795383

[22] Y. Huang, X. Wang, F. Becker, *et al.*, "Introducing dielectrophoresis as a new force field for field-flow fractionation," *Biophysical Journal*, vol. 73, no. 2, pp. 1118 – 1129, 1997. [Online]. Available:
http://www.sciencedirect.com/science/article/pii/S000634959778144X

[23] T. D. Tran, "Development of a zeptofarad (10^{-21} f) resolution capacitance sensor for scanning capacitance microscopy," Master's thesis, University of Manitoba, May 2001. [Online]. Available: http://hdl.handle.net/1993/2539

[24] G. A. Ferrier, S. F. Romanuik, D. J. Thomson, *et al.*, "A microwave interferometric system for simultaneous actuation and detection of single biological cells," *Lab Chip*, vol. 9, pp. 3406–3412, 2009. [Online]. Available: http://dx.doi.org/10.1039/B908974H

[25] "ZEM-4300MH+ data sheet," Mini-Circuits®, Brooklyn, NY, USA. [Online]. Available: http://www.minicircuits.com/pdfs/ZEM-4300MH+.pdf

[26] (2011, October) Model sr830 dsp lock-in amplifier. Stanford Research Systems. Sunnyvale, CA. [Online]. Available: http://www.thinksrs.com/downloads/PDFs/Manuals/SR830m.pdf

[27] E. Salimi, "Nanosecond pulse electroporation of biological cells: The effect of membrane dielectric relaxation," Master's thesis, University of Manitoba, May 2011. [Online]. Available: http://hdl.handle.net/1993/4460

[28] E. Billauer. (2012, July) peakdet: Peak detection using matlab. [Online]. Available: http://billauer.co.il/peakdet.html